

Drug sensitivity and resistance test on a Droplet Microarray chip for solid types of tumors

Zur Erlangung des akademischen Grades eines

DOKTORS DER NATURWISSENSCHAFTEN
(Dr. rer. nat)

von der KIT-Fakultät für Chemie und Biowissenschaften
des Karlsruher Instituts für Technologie (KIT)

genehmigte

Dissertation

von

M.Sc. Maryam Salarian

Referent: Prof. Dr. Pavel Levkin

Korreferent: Prof. Dr. Sylvia Erhardt

Tag der mündlichen Prüfung: 10.02.2025

**Drug sensitivity and resistance test on a
Droplet Microarray chip for solid types of
tumors**

Abstract

Precision oncology is an approach that tailors therapies to the genetic and molecular characteristics of each patient's tumor. Functional precision oncology expands on this idea by identifying optimal treatment strategies based on the specific responses of individual tumors to experimental drug testing. Drug Sensitivity and Resistance Testing (DSRT) involves exposing cancer cells from patient biopsies to various anticancer drugs in vitro to determine the most effective therapy for each patient. However, this strategy often faces a number of challenges, including limited tumor cell availability, in particular from solid tumors, high costs, and long timelines for generating actionable data. These challenges are particularly significant for patients with advanced, inoperable cancers, where core needle biopsies yield small cell samples that must be shared across multiple diagnostic tests, leaving little material for DSRT. Furthermore, traditional DSRT methods, which typically rely on microtiter plates to test multiple drugs, require large amounts of cellular material and costly reagents, making them inaccessible to many patients.

In response to these challenges, miniaturization has emerged as a promising solution, enabling the development of advanced high-throughput screening platforms such as the Droplet Microarray (DMA). The DMA platform uses patterned hydrophilic and superhydrophobic surfaces to confine nanoliter-scale liquid droplets without the need for physical barriers. By reducing assay volumes by several orders of magnitude compared to traditional microtiter plates, the DMA platform significantly lowers cell and reagent consumption, offering a cost-effective approach to DSRT. This study presents the integration of the DMA platform into multiple functional precision oncology studies, demonstrating its application and efficacy in this field. The first project focuses on developing a miniaturized DSRT platform on primary cancer cells derived from patients' Lung cancer tumors. The second project investigates the use of decitabine to sensitize glioblastoma cells and identifies drugs that, when paired with decitabine, demonstrate enhanced efficacy against glioblastoma. The third project introduces a hydrogel-based culture system on DMA platform, capable of incorporating cells or cell spheroids while maintaining stability during washing and medium immersion.

Lung cancer remains a leading cause of cancer mortality worldwide. Current treatment strategies rely on standardized approaches such as surgery, radiotherapy and systemic therapy. In the first project, a miniaturized DSRT platform is developed using DMA technology to advance therapeutic options for this type of cancer toward functional precision oncology. Tumor samples from patients with stage I to III Non-small cell lung carcinoma (NSCLC) were dissociated into single-cell suspensions using manual and semi-automated methods and dispensed onto DMA slides pre-printed with a panel of 12 chemotherapy drugs at five different concentrations. The DMA platform demonstrated reproducible drug sensitivity results with as few as 300 cells per spot, revealing patient-specific responses. Sensitivity to vinorelbine and carboplatin varied across patients and tumor regions, emphasizing the platform's ability to capture both inter- and intra-patient variability. Furthermore, the DMA system successfully conducted DSRT on artificial needle biopsy samples, highlighting its potential for application in patients with limited tumor material.

The second project is focused on glioblastoma (GBM), which is highly resistant to standard therapies due to epigenetic dysregulation. This study investigates a therapeutic strategy that uses decitabine (DAC), a DNA methyltransferase inhibitor, to sensitize glioblastoma cells and enhance their response to treatment, followed by high-throughput screening (HTS) of CNS-penetrating drugs. Using the DMA platform, GBM cells pre-treated with DAC were screened under miniaturized conditions (200 nL per spot) against 722 CNS-penetrating drugs. This high-throughput approach identified several promising drugs including Obatoclax Mesylate, GNE-317, Vorinostat, Trametinib, and Flavopiridol which showed significantly enhanced efficacy in DAC-pretreated cells compared to DAC-untreated cells. These findings highlight the potential of combining epigenetic sensitization, such as with decitabine, and high-throughput drug testing to overcome therapeutic resistance in GBM.

In the third project, to further enhance the physiological relevance of in vitro models, the integration of hydrogel-based 3D cell cultures into the DMA platform was investigated. Dextran-PEG hydrogels were used to create stable nanoliter-volume arrays, supporting individual cells or spheroids. Two methods were developed to generate hydrogel pads on DMA platform. In the first method cells were pre-mixed with hydrogel precursors and dispensed on the spots and the second method includes on-chip gelation of cell-laden droplets. The hydrogel arrays demonstrated high structural integrity and cell viability, maintaining spheroid stability during washing and medium

immersion. The selective gelation of individual spheroids inside of nanoliter droplets enables sorting of different spheroids and their patterning in a simple way, while gelation-degelation cycles provided advanced cell manipulation capabilities. This platform offers a robust tool for high-throughput screening in 3D microenvironments with application in cancer drug screening and precision medicine.

The integration of miniaturized DSRT and 3D culture systems on the DMA platform represents a significant advancement in precision oncology. By reducing the amount of cellular material and reagents required, these technologies make comprehensive drug sensitivity testing accessible to a broader range of patients, including those with minimal biopsy samples. Moreover, the platform enables rapid and cost-effective drug screening, facilitating more personalized and effective cancer therapies. This study highlights the potential of miniaturized HTS platforms in overcoming key limitations in current workflows therefore, advancing research in different fields such as drug screening and functional precision oncology.

Kurzfassung

Die Präzisionsonkologie ist ein Ansatz, der Therapien an die genetischen und molekularen Eigenschaften des Tumors jedes einzelnen Patienten anpasst. Die funktionelle Präzisionsonkologie erweitert dieses Konzept, indem sie optimale Behandlungsstrategien basierend auf den spezifischen Reaktionen individueller Tumore auf experimentelle Medikamententests identifiziert. Drug Sensitivity and Resistance Testing (DSRT) untersucht in vitro die Empfindlichkeit von Krebszellen aus Patientenbiopsien gegenüber verschiedenen Krebsmedikamenten, um die effektivste Therapie zu bestimmen. Diese Methode stößt jedoch häufig auf Herausforderungen wie begrenzte Verfügbarkeit von Tumorzellen, insbesondere bei soliden Tumoren, hohe Kosten und lange Zeiträume für die Generierung verwertbarer Daten. Diese Hindernisse sind besonders relevant bei Patienten mit fortgeschrittenen, inoperablen Krebsarten, bei denen Nadelbiopsien nur geringe Zellmengen liefern, die für mehrere diagnostische Tests aufgeteilt werden müssen, was wenig Material für DSRT übrig lässt.

Um diese Herausforderungen zu bewältigen, hat sich die Miniaturisierung als vielversprechende Lösung etabliert. Plattformen wie die Droplet Microarray (DMA) ermöglichen durch die Nutzung hydrophiler und superhydrophober Oberflächen die Konfination von Nanoliter-Tropfen ohne physische Barrieren. Mit einer drastischen Reduktion der Testvolumina im Vergleich zu herkömmlichen Mikrotiterplatten senkt die DMA-Technologie den Zell- und Reagenzverbrauch erheblich und bietet eine kosteneffiziente Alternative für DSRT. Diese Studie zeigt die Integration der DMA-Plattform in verschiedene funktionelle Präzisionsonkologieprojekte und demonstriert deren Anwendung und Wirksamkeit.

Das erste Projekt widmet sich der Entwicklung einer miniaturisierten DSRT-Plattform für primäre Krebszellen aus Lungenkrebstumoren von Patienten. Tumorproben von Patienten mit NSCLC (Stadium I bis III) wurden durch manuelle und semi-automatisierte Methoden in Einzelzellsuspensionen überführt und auf DMA-Slides mit 12 Chemotherapie-Medikamenten in

fünf Konzentrationen verteilt. Die Plattform zeigte reproduzierbare Ergebnisse bereits bei Zellzahlen von nur 300 Zellen pro Spot und offenbarte patientenspezifische Antworten. Unterschiede in der Empfindlichkeit gegenüber Vinorelbin und Carboplatin zwischen Patienten und Tumorregionen unterstreichen die Fähigkeit der Plattform, sowohl inter- als auch intraindividuelle Variabilität zu erfassen. Darüber hinaus konnte das System erfolgreich DSRT an künstlichen Nadelbiopsieproben durchführen und zeigt so das Potenzial für Anwendungen bei Patienten mit begrenztem Tumormaterial.

Das zweite Projekt fokussiert auf Glioblastome (GBM), die aufgrund epigenetischer Dysregulation hochresistent gegenüber Standardtherapien sind. Hierbei wurde Decitabin (DAC), ein DNA-Methyltransferase-Inhibitor, eingesetzt, um GBM-Zellen zu sensibilisieren und ihre Therapieresistenz zu überwinden. Unter miniaturisierten Bedingungen (200 nL pro Spot) wurden DAC-vorbehandelte GBM-Zellen gegen 722 CNS-penetrierende Medikamente getestet. Die Hochdurchsatzanalyse identifizierte vielversprechende Wirkstoffe wie Obatoclax Mesylate, GNE-317, Vorinostat, Trametinib und Flavopiridol, die in DAC-vorbehandelten Zellen eine signifikant höhere Wirksamkeit zeigten. Diese Ergebnisse verdeutlichen das Potenzial, epigenetische Sensibilisierung und Hochdurchsatztests zu kombinieren, um die Therapie von GBM zu verbessern.

Das dritte Projekt erforschte die Integration von Hydrogel-basierten 3D-Zellkulturen in die DMA-Plattform zur Erhöhung der physiologischen Relevanz von in vitro-Modellen. Dextran-PEG-Hydrogele wurden genutzt, um stabile Nanoliter-Arrays zu erzeugen, die einzelne Zellen oder Spheroide unterstützen. Zwei Methoden zur Zellinkorporation wurden entwickelt: das Vormischen von Zellen mit Hydrogel-Präkursoren und die direkte Gelierung von zellhaltigen Tropfen auf der Plattform. Die Hydrogel-Arrays zeigten eine hohe strukturelle Integrität und Zellviabilität, während die Stabilität von Spheroide während Waschschritten und Mediumwechsel erhalten blieb. Die selektive Gelierung von Spheroide in Nanolitertropfen ermöglicht eine einfache Sortierung, während Gelierungs-De-Gelierungs-Zyklen fortschrittliche Zellmanipulationen unterstützen.

Die Kombination von miniaturisierten DSRT- und 3D-Kultursystemen auf der DMA-Plattform stellt einen bedeutenden Fortschritt in der Präzisionsonkologie dar. Durch die Reduktion des Zell- und Reagenzverbrauchs werden umfassende Tests auch für Patienten mit minimalen Biopsieproben zugänglich. Die Plattform ermöglicht zudem eine schnelle und kosteneffiziente Medikamentenscreening, wodurch personalisierte und effektivere Krebstherapien gefördert werden. Diese Studie unterstreicht das Potenzial miniaturisierter Hochdurchsatzplattformen, zentrale Einschränkungen aktueller Workflows zu überwinden und die Forschung in Bereichen wie Medikamentenscreening und funktionelle Präzisionsonkologie voranzutreiben.

Preface

This thesis is based on results of my research in the group of Prof. Dr. Pavel Levkin between June 2021 and November 2024 at the Institute of Biological and Chemical Systems- Functional Material Systems (IBCS-FMS) at Karlsruhe Institute of Technology (KIT).

The results in Chapter 2.1 were obtained in collaboration with Dr. Marc Schneider, Dr. Michael Meister and Prof. Dr. Thomas Muley, Thoraxklinik, University Hospital of Heidelberg who provided the lung tumor samples, artificial needle biopsies and H&E figures.

Parts of the results were presented at the following conferences as poster:

1. EHA-SfPM Precision Medicine Meeting 2024, Denmark.
2. SLAS 2024 Europe, Spain
3. SLAS 2023 Europe, Belgium
4. NEXUS Personalized Health Technologies, Switzerland

The results in Chapter 2.2 were obtained in collaboration with Prof. Dr. Sevin Turcan, Neurology Clinic and National Center for Tumor Diseases, University Hospital of Heidelberg who provided the cell lines and all the consumable of the project.

The MCF-7 cell line was provided by Dr. Oliver Kassel's research group, Institute of Biological and Chemical Systems - Biological Information Processing (IBCS-BIP).

Parts of the chapter 2.3 results were presented at the following conferences as poster:

1. EHA-SfPM Precision Medicine Meeting 2024, Denmark.
2. SLAS 2024 Europe, Spain

Affidavit

Hiermit versichere ich, diese Arbeit selbstständig verfasst zu haben, dass ich keine anderen als die angegebenen Quellen und Hilfsmittel benutzt habe, dass ich die wörtlich oder inhaltlich übernommenen Stellen als solche kenntlich gemacht habe und die Satzung des KIT zur Sicherung guter wissenschaftlicher Praxis in der jeweils gültigen Fassung beachtet habe.

Karlsruhe, den 07.01.2025

Table of contents

Abstract	I
Kurzfassung.....	IV
Preface.....	VII
Affidavit.....	VIII
Table of contents	IX
List of Figures	XI
List of tables	XIII
List of Abbreviations	XIV
1. General Introduction.....	- 1 -
1.1 The Evolving Landscape of Cancer Treatment.....	- 1 -
1.2. Precision oncology	- 2 -
1.3. Functional precision oncology and Drug sensitivity and resistance test	- 4 -
1.4. The Droplet Microarray as Miniaturized Screening Platform.....	- 14 -
1.5. Objectives	- 21 -
2. Results and discussion.....	- 24 -
2.1. Miniaturized drug sensitivity and resistance test on cells derived from lung cancer patients on Droplet Microarray platform	- 24 -
2.1.1. Project idea and background.....	- 24 -
2.1.2. Tissue dissociation	- 26 -
2.1.3. Drug sensitivity test on patient-derived cells.....	- 35 -
2.1.4. Summary	- 50 -
2.2. High-Throughput Screening to Uncover Therapeutic Vulnerabilities in Decitabine-Treated Glioma cells using Droplet Microarray	- 51 -
2.2.1. Project idea and background.....	- 51 -
2.2.2. Culturing glioma spheroids	- 53 -
2.2.3. High-throughput drug screening	- 62 -

Table of contents

2.2.4. Summary	- 74 -
2.3. Nanoliter Hydrogel Array for High Throughput 3D Cell Screening, Spheroid Sorting and Patterning.....	- 75 -
2.3.1. Project idea and background.....	- 75 -
2.3.2. Protocol optimization	- 77 -
2.3.3. Selective sorting of spheroids	- 85 -
2.3.4. Summary	- 91 -
3. Experimental part	- 93 -
4. Conclusion	- 101 -
5. References	- 105 -
Appendix	- 115 -
Curriculum Vitae	- 133 -
Acknowledgement	- 134 -

List of Figures

Figure 1. Cancer Therapy.....	- 3 -
Figure 2. Comparison of biological models for precision oncology various features.....	- 12 -
Figure 3. Photo of a part of Droplet Microarray (DMA).....	- 16 -
Figure 4. Overview of applications of the Droplet Microarray..	- 20 -
Figure 5. Concept and experimental workflow of miniaturized DSRT for patient-derived lung cancer cells on the DMA slide.....	- 27 -
Figure 6. Detection of EpCAM-positive cancer cells in cell suspensions post-isolation and after 24-hour incubation.....	- 33 -
Figure 7. Cell viability of isolated tumor cells cultured on the DMA slide.	- 34 -
Figure 8. Drug sensitivity test on patient-derived cells.....	- 38 -
Figure 9. Comparison of dose-dependent effects of compounds on primary patient-derived cells cultured on a DMA slide.....	- 41 -
Figure 10. Workflow for evaluating the reproducibility of drug sensitivity tests on patient-derived cells ...	- 42 -
Figure 11. Reproducibility of drug sensitivity testing across different cell densities..	- 43 -
Figure 12. Workflow of evaluating intratumor heterogeneity in drug sensitivity across distinct tumor regions.....	- 44 -
Figure 13. Drug sensitivity across different regions of a single tumor specimen.....	- 46 -
Figure 14. Workflow for drug sensitivity testing using needle biopsy samples..	- 48 -
Figure 15. Drug sensitivity testing using needle biopsy samples	- 49 -
Figure 16. Formation of a single cell spheroid on a spot of the DMA slide.....	- 54 -
Figure 17. Single-cell spheroids of L0125 and L0512 on DMA slides.....	- 55 -
Figure 18. Optimization of cell density for single spheroid formation on DMA slide using L0125 cells. ...	- 57 -
Figure 19. Optimization of cell density for single spheroid formation on DMA slide using L0512 cells. ...	- 58 -
Figure 20. Culture and growth analysis of single spheroids on DMA slide over 7 days.	- 60 -
Figure 21. Spheroid formation in L0125 and L0512 cells following decitabine pretreatment.....	- 62 -
Figure 22. Drug hits for L0125 cell line using dual read-out..	- 67 -
Figure 23. Drug hits for L0512 cell line using dual read-out..	- 72 -
Figure 24. Nanoliter hydrogel array on the DMA platform..	- 78 -
Figure 25. Homogeneity of hydrogels.....	- 79 -
Figure 26. Cell culture in nanoliter hydrogel array.....	- 80 -
Figure 27. Comparison of cell culture in nanoliter hydrogel array and in array of liquid droplets..	- 81 -
Figure 28. Validation of the stability of hydrogel pads on the DMA slide during washing procedure..	- 82 -
Figure 29. Stable nanoliter hydrogel array.	- 84 -
Figure 30. Stability of hydrogels on coated DMA spots.	- 86 -

List of Figures

Figure 31. Gelation of single spheroid array on the DMA slide.....	- 87 -
Figure 32. Gelation and stability of spheroids in hydrogels on DMA slide.	- 88 -
Figure 33. Sorting of cell spheroids.	- 89 -
Figure 34. Digestion of hydrogel.	- 90 -

List of tables

Table 1. Summary of patient-derived tumor samples used in the study.....	-30-
Table 2. Anticancer cytotoxic drugs used in this study	-36-
Table 3. Hits identified in high-throughput screening of L0125 cells.....	-64-
Table 4. Hits identified in high-throughput screening of L0512 cells.....	-69-
Table 5. List of 722 CNS-penetrant compound library	-115-

List of Abbreviations

2D	Two-dimension
2-HG	2-hydroxyglutarate
3D	Three-dimension
α -KG	α -ketoglutarate
°C	Degree Celsius
CDK	Cyclin-dependent kinase
CNB	Core needle biopsy
CNS	Central nervous system
DAC	Decitabine
DMA	Droplet Microarray
DMEM	Dulbecco's Modified Eagle Medium
DMSO	Dimethylsulfoxide
DNMT	DNA methyltransferase enzyme
DSRT	Drug sensitivity and resistance test

List of Abbreviations

ECM	Extracellular Matrix
EGFR	Epidermal growth factor receptor
EpCAM	Epithelial Cell adhesion molecule
GBM	Glioblastoma
GDSC	Genomics of Drug Sensitivity in Cancer
HEMA-EDMA	2-hydroxyethyl methacrylate-co-ethylene dimethacrylate
hiPSCs	Human induced pluripotent stem cells
HTS	High-throughput screening
IDH	Isocitrate dehydrogenase
μM	10^{-6} Mol/L
MGMT	O-6-methylguanine-DNA methyltransferase
nM	10^{-9} Mol/L
NSCLC	Non-small cell lung cancer
PBS	Phosphate buffered saline
PCR	Polymerase Chain Reaction
PDT	Patient-derived tumorspheres
PDAC	Pancreatic ductal adenocarcinoma

List of Abbreviations

PDX	Patient-derived xenograft
PEG	Polyethylene glycol
PI	Propidium Iodide
PI3K	Phosphatidylinositol 3-kinase
P/S	Penicillin-Streptomycin Mixture
SCLC	Small-cell lung cancer
θ	Contact angle

1. General Introduction

1.1. The Evolving Landscape of Cancer Treatment

Cancer, a leading cause of mortality worldwide, is a group of diseases characterized by uncontrolled proliferation of abnormal cells and the ability to invade adjoining parts of the body or spread to the other organs. ^(1,2) In 2022, an estimated 20 million new cancer cases were diagnosed worldwide, with 9.7 million deaths. Approximately 53.5 million people were living within five years of their cancer diagnosis. On average, around 1 in 5 people will develop cancer during their lifetime, while roughly 1 in 9 men and 1 in 12 women will die from the disease, reflecting the growing burden of the disease worldwide ⁽³⁾. This alarming trend highlights the critical need for continued research and advancements in cancer prevention, diagnosis, and treatment strategies.

A tumor is an abnormal mass of tissue that arises from uncontrolled cell growth. Tumors can be classified as benign (non-cancerous) or malignant (cancerous), with malignant tumors having the ability to invade and spread to other parts of the body via the circulatory or lymphatic systems forming the metastasis. Solid tumors are a category of malignant tumors that develop in solid organs such as the lungs or brain. Unlike hematologic malignancies, which affect blood-forming tissues, solid tumors develop in various organs and tissues and are further classified based on their tissue of origin and biological characteristics. There are three major types of solid tumors: Carcinomas, the most common type, arise from epithelial cells that line organs and body surfaces, Sarcomas develop from connective tissues such as bone, muscle, or fat, ⁽⁴⁾ and central nervous system (CNS) tumors, including gliomas, originate in the brain or spinal cord. ⁽⁵⁾

The treatment of solid tumors typically involves a combination of conventional methods such as surgical resection followed by radiotherapy and systemic therapies (Figure 1), including chemotherapy, targeted therapy, and immunotherapy, which affect the entire body in contrast to localized treatments such as surgery or radiation that target specific areas. While these approaches can be effective in certain context, they are developed based on large clinical trials designed to provide broad therapeutic benefits to a wide range of patients. ⁽⁶⁾ However, these conventional methods often fail to address the unique characteristics of individual cancers. Some tumors may be

resistant to commonly used therapies, making them ineffective, while others may respond better to less conventional treatments. Furthermore, cancers often contain specific mutations, markers, or molecular features that can guide the selection of the most suitable therapy, but these are not considered in traditional approaches.⁽⁷⁾

These limitations highlight the need for more targeted and personalized approaches in cancer treatment. Therefore, in recent years, there has been a shift in oncology toward more personalized and precise treatment strategies.

1.2. Precision oncology

Precision oncology is an innovative approach to cancer treatment that tailors therapies based on the genetic, molecular, and environmental characteristics of an individual's tumor.⁽⁸⁾ The primary aim of precision oncology is to move away from the 'one-size-fits-all' model of cancer treatment by identifying and targeting the specific characteristics of a tumor therefore, improve the treatment outcomes, reduce unnecessary side effects, and offer more effective therapeutic options.⁽⁹⁾ One common approach in precision oncology include genomic sequencing, which identifies mutations and alterations within tumors. Many tumor-specific molecular alterations, such as protein overexpression, mutations in driver genes, and gene rearrangements, serve as well-established predictive biomarkers for response to targeted therapies. As a result, clinical molecular pathology analysis has become a laboratory tool for characterizing tumor biology and guiding therapeutic decisions.⁽¹⁰⁾ Targeted therapies are designed to affect only the abnormal molecule involved in cancer growth and progression, in contrast to chemotherapy, which is nonselective and affects all rapidly dividing cells. Drugs used in molecular targeted therapy can inhibit signals that promote cancer cell growth, disrupt cell cycle regulation, or trigger cell death to eliminate cancer cells.⁽¹¹⁾ These methods have led to significant advancements in cancer treatment (Figure 1).

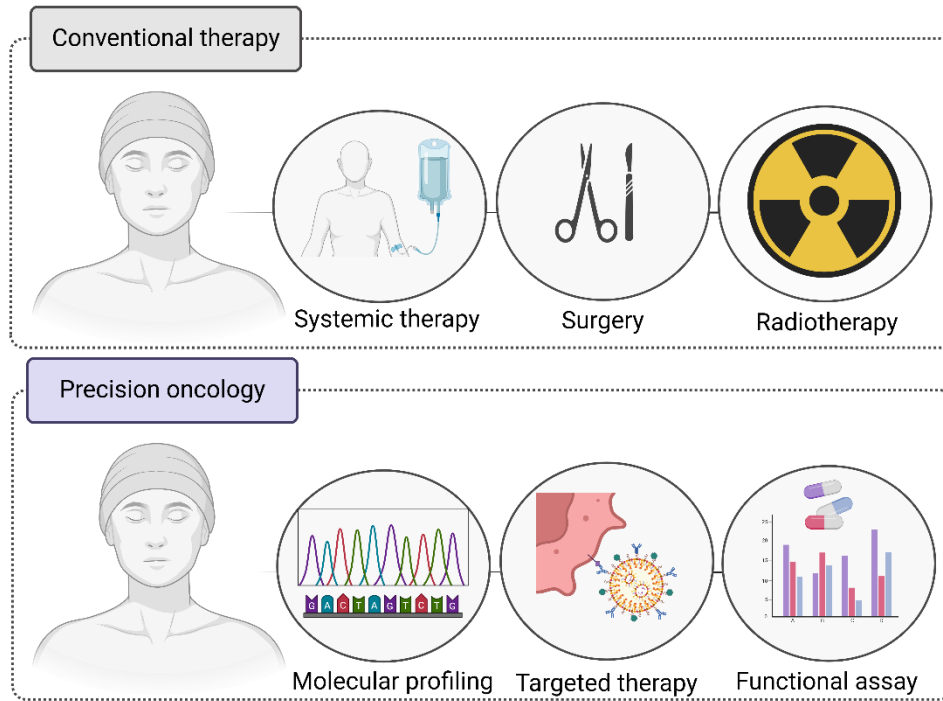


Figure 1. Cancer Therapy. The treatment of solid tumors traditionally involves a combination of conventional approaches, including surgical resection followed by radiotherapy and systemic therapy (upper panel). Precision oncology (lower panel) represents an innovative approach that tailors treatments based on molecular profiling, incorporating targeted therapies and functional drug testing assays for personalized cancer care.

However, precision oncology faces several challenges. While the number of druggable genetic alterations and predictive biomarkers is increasing, molecular profiling does not always result in the identification of reliable and clinically actionable biomarkers, and some tumors may completely lack biomarkers that can be targeted.⁽¹²⁾ Another major obstacle is tumor heterogeneity, where different cells within the same tumor can have distinct genetic profiles, making it difficult to identify a single target for a therapy.⁽¹³⁾ Furthermore, targeted therapies are effective only if the cancer possesses the specific alteration that can be targeted with such therapies, and many cancers eventually develop resistance to these therapies over time.⁽¹¹⁾

To address some of these challenges, the field is turning to functional precision oncology. This approach goes beyond genetic and molecular profiling by experimentally testing how cells derived from a patient's tumor respond to different anticancer drugs. It involves testing live tumor cells derived from patient biopsies against a panel of potential therapies to identify the most effective treatment based on the actual drug sensitivity results. Therefore, it does not rely solely on predicted sensitivity from genetic data.⁽¹⁴⁾ The advantage of functional precision oncology is that it can identify effective therapies even in cases where other approaches in precision oncology might not be efficient, for example when tumors lack predictive genetic biomarkers.⁽¹⁵⁾

1.3. Functional precision oncology and Drug sensitivity and resistance test

An important method in functional precision oncology is drug sensitivity and resistance testing, which involves exposing live tumor cells to a range of potential anticancer drugs to evaluate their effectiveness.⁽¹⁶⁾ This method helps identify which drugs are most likely to be effective based on the actual response of the tumor cells, rather than predictions based only on genetic information. Additionally, it can uncover potential resistant cell populations that may not be detected through genetic profiling. These tests can be conducted before treatment to guide initial therapy selection and during treatment to monitor emerging resistance. By continuously evaluating the tumor's response at different stages, clinicians can adapt the treatment strategy in real time.^(14, 17)

By identifying both effective treatments and potential resistant cell populations, functional precision oncology enables a more dynamic and responsive treatment strategy. This method not only enhances the ability to select the most appropriate therapy for each patient but also helps overcome the challenge of drug resistance by identifying alternative treatments that remain effective as the tumor changes overtime. As a result, functional precision oncology has the potential to improve treatment outcomes and offer more personalized and adaptive treatment strategies.⁽¹⁸⁾

Drug repurposing, also known as drug repositioning, is an emerging approach within precision oncology that has gained importance in the context of DSRT. It involves testing approved or investigational drugs originally developed for other diseases and identifying new therapeutic applications beyond their initial medical indications.⁽¹⁹⁾ This approach offers advantages over

developing new drugs for a given condition. The risk of failure is lower, as repurposed drugs have already undergone preclinical safety testing and, in some cases, human trials, making them less likely to fail due to safety concerns in efficacy trials. Additionally, repurposing reduces the time needed for drug development since the preclinical testing, safety assessment, and sometimes even formulation development has already been completed.⁽²⁰⁾ This can significantly lower the cost of bringing a repurposed drug to market, which is estimated at around €280 million on average, compared to the €1.9–2.8 billion and 13 to 15 years typically needed to develop new drugs.⁽²¹⁾ Furthermore, because of the financial risks involved, not all diseases are prioritized in drug discovery, leaving patients with rare conditions facing limited therapeutic options.⁽²²⁾

Drug repurposing has the potential to uncover new biological targets and pathways, providing further insights into disease mechanisms. Well-known examples of successful drug repurposing include sildenafil (Viagra), originally developed to treat hypertension but later found to be an effective treatment for erectile dysfunction,⁽²³⁾ and thalidomide, a sedative that was initially withdrawn due to causing severe birth defects but was later repurposed to treat multiple myeloma.⁽²⁴⁾ These cases highlight the significant therapeutic success that repurposed drugs can achieve.

By adding the drugs that were not originally designed for a specific cancer type to the panel of DSRT tests, the range of potential treatments will expand and precision oncology can identify previously unexpected therapeutic options that may prove effective against a patient's tumor, particularly when standard treatments fail or the tumor demonstrates resistance to commonly used drugs. Repurposed drugs, having already been through clinical trials for safety and dosage in other conditions, offer an accelerated pathway to cancer therapy, helping to reduce time, costs, and risks associated with the development of new treatments. This approach not only increases the chance of finding the best treatment option for the patients but also aligns with the goals of precision oncology by providing more personalized and adaptive treatment options.⁽²⁵⁾

This is where high-throughput screening (HTS) plays an important role. HTS is the process of testing large numbers of compounds or drugs in an automated manner. The primary goal is to identify 'hits' which are compounds that affect the target in the desired manner. The greater the

number and diversity of compounds that are run through a screen, the more successful it is likely to be.⁽²⁶⁾

The growing number of compounds for these tests can only be managed by significantly reducing the size and scale of HTS assays. During the advent of HTS in the 1990s, 96-well microplates were the standard format for handling and screening compounds. However, in recent years, there has been a shift toward using plates with higher well densities. To conduct a successful HTS assay, a balance between three key factors, often referred to as the "magic triangle": time, cost, and quality, must be achieved.⁽²⁷⁾ While speeding up assays helps shorten the time needed to identify new treatment options, this must be done without compromising data quality or increasing costs. HTS automation and the ability to process thousands of wells in parallel effectively reduce assay times, but costs can rise with increasing complexity, particularly when advanced reagents or technologies are involved.⁽²⁸⁾

As these advancements have refined the technical aspects of HTS, a range of innovative models and approaches are emerging in this field to provide more accurate and reliable data for personalized cancer treatment (Figure 2). Two-dimensional (2D) monolayer cultures have long been used in cancer research, where tumor cells are grown in a flat, two-dimensional layer, allowing for rapid cell expansion and large-scale drug screening. The main advantages of 2D cultures are their fast expansion, low cost, and high throughput, making them ideal for rapid testing of multiple drugs or experimental conditions.⁽²⁹⁾ An example of using this model is the study of *Kim, S. et al.*, where patient-derived cells from lung cancer patients were cultured in 384-well plates (1000 cells per well) and exposed to 64 chemotherapeutic agents.⁽³⁰⁾

However, the 2D structure of the cultures does not accurately represent the three-dimensional architecture of tumors in the human body, which means that many key components of the tumor microenvironment, such as the interaction of cells with their extracellular matrix (ECM), are missing. These interactions play an important role in regulating cell differentiation, proliferation, drug metabolism, and other cellular functions.^(31,32) Once cells are isolated from their original tissue and transferred to 2D culture conditions, their morphology undergo significant changes. The changed morphology of the cells can affect their properties and therefore drug response.^(33, 34) Another limitation of 2D cultures is that cells in a monolayer have unrestricted access to the

ingredients of the medium such as oxygen, nutrients, metabolites and signal molecules. In contrast, for cancer cells *in vivo* the availability of these elements is more variable because of the natural architecture of the tumor mass.⁽³¹⁾ Additionally, 2D adherent cultures are typically monocultures, allowing for the study of only a single cell type, which leads to the absence of a tumor microenvironment or niches, an essential element for supporting cancer-initiating cells *in vivo*. As a result, drug responses observed in 2D monolayers may not fully represent how tumors respond to the therapy.^(29, 35)

In the last decades, three-dimensional (3D) cell culture models have emerged to represent *in vivo* condition more closely. Unlike traditional 2D cultures, 3D models allow cells to grow and interact with the surrounding extracellular matrix, better reflecting the natural environment within living tissues. These models promote cell-to-cell and cell-to-extracellular matrix interactions, supporting more accurate cell proliferation and differentiation.⁽³⁶⁾ Additionally, cell morphology, behavior, and organization in 3D cultures more closely resemble those seen *in vivo*.⁽³⁷⁾ A key distinction between 2D and 3D cultures is nutrient access. In 2D cultures, cells have uniform access to nutrients, whereas in 3D models, nutrient gradients naturally form, with cells deeper within the structure having reduced access.⁽³⁸⁾ This feature is important because nutrient and oxygen availability play key roles in cellular metabolism, signaling, and drug responses.⁽³⁹⁾ For instance, cancer cells are known to have different metabolic adaptation pathways depending on the nutrient supply they have. Glycolytic cancers rely on glycolysis, whereas oxidative cancers depend on oxidative phosphorylation. As a result, they respond differently to drugs targeting tumor metabolism.⁽⁴⁰⁾ This metabolic heterogeneity cannot be effectively modeled in 2D cultures, as the uniform access to nutrients in these systems eliminates the gradients necessary for studying such adaptations. Additionally, hypoxia, a condition of reduced oxygen availability, is a hallmark of many solid tumors and significantly impacts tumor biology and therapy responses. In 3D cultures, hypoxia and its associated mechanisms, such as the activation of hypoxia-inducible factors (HIFs), can be modeled, providing insights into how tumors survive in oxygen-deprived environments. Hypoxia-induced changes include altered cell signaling, increased angiogenesis, and resistance to certain chemotherapeutics, which are absent in traditional 2D systems.⁽⁴¹⁾ Therefore, 3D cultures provide a more physiologically relevant platform for studying how cancer cells respond to drugs under conditions mimicking the tumor microenvironment, including metabolic and oxygen stress.

Tumor spheroids and organoids are among the most commonly used 3D cell models in oncology. Spheroids are simple aggregates formed from either a single cell type or a mixture of different cells, typically cultured as free-floating clusters. These spheroids develop an outer layer of cells exposed to the external environment, while inner layers are embedded deeper within the structure, creating gradients of nutrients and oxygen that mimic *in vivo* conditions.⁽⁴²⁾ Spheroids also exhibit distinct cellular phenotypes that resemble the architecture of actual tumors, including necrotic, proliferating, and non-proliferating cell populations. Spheroids form through the self-organization of individual cells, which can be derived from cancer cell lines or patient-derived cancer cells.⁽⁴³⁾

An example of using patient-derived tumor spheroid cultures in personalized cancer treatment is the study conducted by *Hofmann et al.*, where spheroids were grown *in vitro* from primary breast cancer tissue in 96-well plates and subjected to different anticancer drugs.⁽⁴⁴⁾

Several technical methods are used to create spheroids, each with its advantages and specific applications, depending on the cell types and research goals, including:

1. **Pellet Culture:** This technique uses centrifugal force to concentrate cells at the bottom of a tube, promoting cell-cell adhesion. The concentrated cells are then resuspended in a medium, transferred to a well plate, and allowed to form spheroids.⁽⁴⁵⁾ This method is particularly suitable for studying the differentiation of mesenchymal stem cells.⁽⁴⁶⁾
2. **Liquid Overlay:** This method prevents cell attachment to the surface by using non-adherent surfaces, typically made of agarose, to allow cells to self-assemble into spheroids.⁽⁴⁷⁾ Hyaluronic acid is more effective in creating a surface for cancer research as it interacts with tumor cell surface receptors, enhancing cellular signaling related to proliferation and resistance to cancer therapies. This method is highly beneficial for generating spheroids for drug testing in high-throughput systems.⁽⁴⁸⁾
3. **Hanging Drop:** In the hanging drop method, droplets containing suspended cells are placed on a surface. Then the surface is placed upside down, where surface tension and gravity allow the cells to aggregate into spheroids. This technique offers precise control over spheroid size by adjusting the volume of the droplet and the density of the cell suspension.⁽⁴⁹⁾ While it is often

used for small-scale experiments due to its simplicity and ability to generate uniform spheroids, it can also be scaled up to produce large numbers of spheroids quickly.⁽⁵⁰⁾

4. **Spinner Culture:** In spinner culture, a stirring bar mixes a cell suspension in a bioreactor, promoting the formation of spheroids through convectional force. This method is scalable and suitable for growing spheroids for drug testing or stem cell differentiation studies. However, controlling the stirring rate is critical, as too fast a rate may damage cells, while too slow may result in cells settling at the bottom of the bioreactor.⁽⁵¹⁾
5. **Rotating Wall Vessel:** This system mimics microgravity by rotating the culture vessel, keeping cells in a suspended state, which allows them to aggregate into spheroids. This method is useful in studying the effects of microgravity on cell growth and differentiation. It is particularly valuable for applications in tissue engineering and regenerative medicine.⁽⁵²⁾
6. **Magnetic Levitation:** In this technique, cells are mixed with magnetic particles and exposed to a magnetic field, causing them to levitate and aggregate into spheroids. This method is useful for co-culturing different cell types and maintaining the structural integrity of spheroids.⁽⁵³⁾

Organoids were initially developed from healthy tissues,⁽⁵⁴⁾ offering a 3D culture system that replicates the cellular architecture and function of specific organs. These organoids are typically derived from stem cells, which self-organize on extracellular matrix scaffolds, differentiating into various cell types that form complex tissue structures. This enables them to recapitulate the primary tissue's function and structure.⁽⁵⁵⁾ The development of tumor-derived organoids, known as "tumoroids" extended this approach to cancer research, enabling the modeling of tumors in vitro. While organoids and tumoroids share a 3D architecture, they differ fundamentally in their origins and characteristics. Organoids derived from healthy tissues are generated from stem cells and are inherently heterogeneous, consisting of multiple cell types that reflect the complexity of their tissue of origin. In contrast, tumoroids are formed directly from cancer cells, making them more homogeneous in composition.⁽⁵⁶⁾

Tumoroids and spheroids are both 3D cancer models. However, tumoroids are derived directly from patient tumors or cancer cell lines, retaining the genetic and phenotypic characteristics of the original tumor. In contrast, cancer spheroids are typically formed by aggregating cancer cells under

non-adherent conditions, resulting in a less structured and often less physiologically relevant model.⁽⁵⁷⁾

These 3D models are especially valuable for three key purposes: studying the mechanisms of cancer progression and resistance, conducting in vitro screening of anti-cancer therapies and replicating the unique characteristics of a patient's tumor in vitro, enabling personalized screening to identify the most effective treatments for each patient.⁽⁵⁸⁾

Despite these advantages, 3D cultures present certain challenges, such as difficulties in selecting immunofluorescence, often need modification for 3D models due to issues with staining penetration and sample clearing.⁽⁵⁹⁾ The generation of organoids from patient-derived tissue is often time-consuming, and, like 2D cultures, they can undergo changes during prolonged ex vivo growth, which can affect their accuracy in representing the original tumor and their reliability for drug testing.⁽⁶⁰⁾ While organoids offer a more realistic replication of the tumor environment compared to 2D models, they still lack essential components such as immune cells and vasculature, which are critical for cancer progression and this limits their ability to fully replicate the in vivo tumor environment.⁽⁶¹⁾

Moving beyond traditional culture systems, microfluidic devices represent cutting-edge tools in functional precision oncology. Microfluidic systems can provide a defined microenvironment that mimics key aspects of the tumor's physical and biochemical features. By controlling the flow of nutrients, oxygen, and drugs through small fluid channels, these devices allow researchers to more accurately replicate the tumor microenvironment.⁽⁶²⁾ This model is particularly valuable for studying how tumors respond to drugs under controlled environment that closely resemble those in the body.⁽⁶³⁾ They can also be used to create spheroids at a microscale and improve oxygen and nutrient diffusion within spheroids, making them suitable for long-term culture.⁽⁶⁴⁾ In a study conducted by *Schuster B. et al.*, an automated, high-throughput microfluidic device was developed for 3D organoid culture from tumor samples collected from human pancreatic ductal adenocarcinoma (PDAC) patients to facilitate preclinical research and personalized therapies.⁽⁶⁵⁾ Also, *Prince E. et al.* introduced a microfluidic spheroids-on-a-chip platform that enables the efficient growth of large arrays of tumor spheroids from a breast carcinoma cell line for multiplexed

anticancer drug testing. This system self-organizes cancer cells into gelling droplets, forming spheroids with consistent sizes within 72 hours in a hydrogel.⁽⁶⁶⁾

While microfluidic devices are highly customizable and can offer insights into tumor behavior that other models cannot, they are generally low throughput, making them less suitable for large-scale drug screenings.⁽⁶⁷⁾ Furthermore, despite their ability to recreate certain microenvironmental factors, they still miss some key components, such as immune interactions.⁽⁶⁸⁾

Finally, patient-derived xenografts (PDX) offer perhaps the most accurate in vivo model for studying tumor behavior and drug response. In PDX models, tumor cells from a patient are implanted into immunocompromised mice, allowing the tumor to grow in a living organism.⁽⁶⁹⁾ This model provides a highly realistic environment, capturing not only the architecture of the tumor but also incorporating pharmacokinetics—how drugs are absorbed, distributed, metabolized, and excreted in a living system. Additionally, PDX models provide a clear readout of drug toxicity, offering insights into both the efficacy and safety of treatments.⁽⁷⁰⁾

In a study by *Guillen K. et al.*, a bank of human PDXs and matched organoid cultures from challenging breast cancer cases, such as metastatic types were reported. These PDXs and PDX-derived organoids were used for cost-effective drug screening and in vivo validation. The study demonstrates the potential of these models for real-time precision oncology, as shown in a case of triple-negative breast cancer with early metastatic recurrence. The researchers identified an FDA-approved drug that showed high efficacy, resulting in a complete response and a significantly extended progression-free survival period for the patient.⁽⁷¹⁾

However, PDX models come with significant limitations. They are slow to expand, making them unsuitable for rapid drug testing. They are also costly to maintain and are not easily scalable for high-throughput studies. Furthermore, there are species differences between the human tumor and the mouse host, which can introduce variables that complicate the interpretation of results. Moreover, the immunocompromised state of the mice used in PDX models means that these systems lack the immune interactions that are crucial for understanding how the body's immune system responds to cancer therapies.⁽⁷²⁾

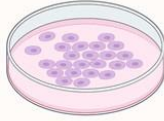
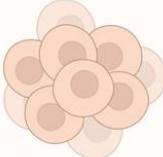

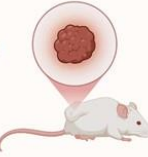
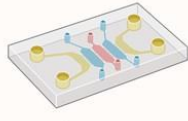
					
	2D cell culture	Spheroid	Organoid	PDX	Microfluidic device
Ease of system setup	✓	✓	✓	✓	✓
Ease of maintenance	✓	✓	✓	✓	✓
Duration of experiments	✓	✓	✓	✓	✓
Physiological relevance	✗	✓	✓	✓	✓
Cost	✓	✓	✓	✓	✓
Time needed for setup	✓	✓	✓	✗	✓/✓
<div> ✓ Best ✓ Good ✓ Partly suitable ✗ Not suitable </div>					

Figure 2. Comparison of biological models for precision oncology various features, including system setup simplicity, maintenance requirements, compatibility with long-term experiments, physiological relevance, cost and time needed for stabilising. The models evaluated are 2D cell cultures, spheroids, human organoids, patient-derived xenografts (PDX) and microfluidic devices. Each model demonstrates unique strengths and limitations, providing a framework for selecting the most suitable system based on research objectives. Inspired and modified from Nature Reviews Molecular Cell Biology 21, 571-584(2020).⁽⁷³⁾

Despite the significant advances in precision oncology, several key challenges remain. The most critical problem is the limited amount of cellular material that can be obtained from tumors, especially from small solid tumors.⁽¹⁴⁾ In many cases, a significant part of the patient's sample is used for diagnostic tests, such as pathology, immunohistochemistry, and genetic profiling, which leaves insufficient cellular material for DSRT. Precision oncology often relies on high-throughput drug screening, which typically requires a significant amount of cellular material to test multiple drug candidates and dosage levels. When only a small number of viable cells are available, it becomes difficult to generate meaningful results, particularly for personalized treatment plans that depend on testing a wide array of drugs.⁽¹⁷⁾

In most studies, the cells used for in vitro drug testing are obtained after surgical removal of the tumor which very often leads to obtaining sufficient number of cells for testing. However, this restricts the application of such tests to patients who undergo surgery. Therefore, many patients, particularly those with metastatic or recurrent tumors, cannot benefit from comprehensive drug testing, which could reveal critical information about their tumor's response to various therapies.⁽⁷⁴⁾

To overcome this limitation, needle biopsy samples offer a promising alternative. Needle biopsies are non-invasive and can be taken even from patients for whom surgery is not an option. Using needle biopsies for DSRT allows for the inclusion of a broader patient population in drug sensitivity tests.⁽⁷⁵⁾ However, needle biopsies yield fewer viable cells, making it even more difficult to perform comprehensive drug testing using traditional methods.

Another significant challenge in precision oncology is the high cost of reagents and anticancer therapies, particularly when using large compound libraries and newly developed targeted therapies, which can be expensive.⁽⁷⁶⁾ As mentioned earlier, precision oncology often involves high-throughput screening, where a wide array of drugs is tested to identify the most effective treatment for an individual patient. This can include hundreds of drug compounds, ranging from standard chemotherapies to more recent targeted therapies. The cost of using these drugs for comprehensive drug testing can significantly increase the overall expense, making these tests inaccessible for many patients.⁽¹⁷⁾ Additionally, the use of advanced models, such as PDX models, further increases the costs. These models require specialized facilities and high maintenance, making them an expensive option for testing.⁽⁷⁷⁾

Another significant challenge is the time it takes to establish and expand certain models, particularly PDXs and tumoroids. PDX models can take several months to grow. Similarly, organoids, while faster to establish than PDXs, still require several weeks to expand into a sufficient size for drug screening. For aggressive cancers or treatment-resistant tumors, this delay can be critical, as patients may not have the luxury of time for weeks of preclinical testing to identify an effective therapy.⁽⁷⁸⁾ This extended timeline creates a gap between obtaining patient samples and delivering actionable treatments, reducing the overall efficiency of the precision oncology workflow.

Miniaturization in precision oncology offers a promising solution to many of the challenges in the field. By reducing the scale of drug testing platforms, miniaturization has the potential to significantly lower the number of cells required for testing.⁽⁷⁹⁾ This is particularly helpful when working with small and limited tumor samples, such as those obtained from needle biopsies, where the cell count is very low. In miniaturized systems, even small quantities of cells can be sufficient to perform comprehensive drug testing, allowing more patients to benefit from precision oncology.

In addition, miniaturization significantly reduces the amount of reagents and drugs needed for tests. Traditional high-throughput screening methods often require large volumes of reagents, media, and drug compounds. By scaling down the assays, miniaturized platforms reduce these material requirements, making the process more cost-effective without compromising the quality or reliability of the results.⁽⁸⁰⁾ This reduction in reagent and drug use also lowers the overall expense of testing, making precision oncology more accessible to a broader patient population. Additionally, miniaturization enhances throughput by enabling the simultaneous testing of more drug compounds on a smaller scale.⁽⁸¹⁾ With the ability to test a larger number of conditions in parallel, miniaturized platforms can accelerate the drug screening process.

As the field continues to evolve, miniaturization holds the potential to transform how we approach precision oncology, making it more efficient and accessible.

1.4. The Droplet Microarray as Miniaturized Screening Platform

As high-throughput screening technologies evolve, the demand for platforms that enable more efficient drug testing is increasing, particularly in precision oncology, where time, cost, and sample availability are critical parameters. Miniaturization is essential to meet these demands, as traditional platforms like microtiter plates, while reliable, face limitations. Conventional microtiter plates, typically featuring 384 or 1536 wells, occupy relatively large surface areas (127×85 mm) and require microliter-scale volumes of reagents for each well. The working volume of a 384-well is about 50 μ L per well, accommodating four times more samples than a 96-well microplate. The typical working volume for a 1536-well plate ranges from about 2.5 to 10 μ L, with a standard volume of approximately 5 μ L per well.⁽⁸²⁾

This is problematic in precision oncology, where the available sample from patient biopsies is often minimal, and reagents, particularly novel and targeted therapies, can be expensive. The solid walls in microtiter plates might be necessary to prevent cross-contamination of neighboring wells, but they also lead to high adsorption and capillary effects which get more and more problematic the smaller the wells become, and also prevent the sample from direct contact with a second target placed on top, complicating their use as screening platforms when transitioning to smaller-scale volumes.⁽⁸³⁾

To overcome the limitations of microtiter plate, the Droplet Microarray (DMA) platform was introduced as a miniaturized solution for high-throughput screening in biological and chemical research, introduced by the *Levkin group* in 2011.⁽⁸⁴⁾ The DMA represents a significant improvement over traditional microtiter plates due to its compact design and its ability to form highly controlled liquid droplets in nanoliter volumes. The DMA uses patterned hydrophilic and superhydrophobic surfaces to confine liquid samples within specific geometries without the need for physical barriers necessary for conventional microtiter plates.⁽⁸⁵⁾

Wettability, which refers to how a liquid spread on a surface and the extent of its contact area, plays a key role in the DMA's function. Wettability is typically described using the water contact angle (WCA) (θ), defined as the angle formed at the junction of the liquid-solid and air-liquid interfaces. When a droplet comes into contact with a solid surface, it forms a contact line where the liquid, gas, and solid substrate intersect.⁽⁸⁶⁾ The WCA serves as a quantitative measure of the surface's affinity for water: smaller angles indicate better wettability (hydrophilicity), while larger angles indicate poorer wettability (hydrophobicity). Surfaces are classified into different wettability categories based on their contact angle values: hydrophilic ($\theta < 90^\circ$), hydrophobic ($90^\circ < \theta < 150^\circ$), superhydrophilic ($\theta < 10^\circ$), or superhydrophobic ($\theta > 150^\circ$).⁽⁸⁷⁾

The fabrication of DMA slides is based on manipulating surface wettability, particularly by creating hydrophilic and superhydrophobic patterned areas. *Jokinen et al.* (2008) demonstrated that droplets can be confined to hydrophilic zones if there is a significant difference in wettability. Superhydrophobic barriers surrounding hydrophilic areas effectively prevent droplet dispersion, while the precise combination of these contrasting wettability properties on a single surface can be achieved through photolithography, enabling the creation of well-defined, structured patterns.⁽⁸⁸⁾

In 2014, *Feng et al.* developed a rapid, initiator-free method for fabricating superhydrophilic-superhydrophobic micropatterns using sequential thiol-yne click chemistry.⁽⁸⁹⁾

The DMA platform is built on a standard microscope slide measuring 25×76 mm. These slides are modified through surface patterning techniques that create alternating hydrophilic and hydrophobic areas (Figure 3). One type of DMA platform is the HEMA-EDMA slide where initially, a thin porous polymer layer, poly(2-hydroxyethyl methacrylate-co-ethylene dimethacrylate) (HEMA-EDMA), is applied to the slide. This layer is then chemically modified using thiol-yne click chemistry, enabling the creation of hydrophobic and hydrophilic regions. Hydrophobic areas are formed using alkyne polymers modified with 1H,1H,2H,2H-perfluorodecanethiol, while hydrophilic areas are generated using cysteamine hydrochloride or similar polar thiols.⁽⁸²⁾

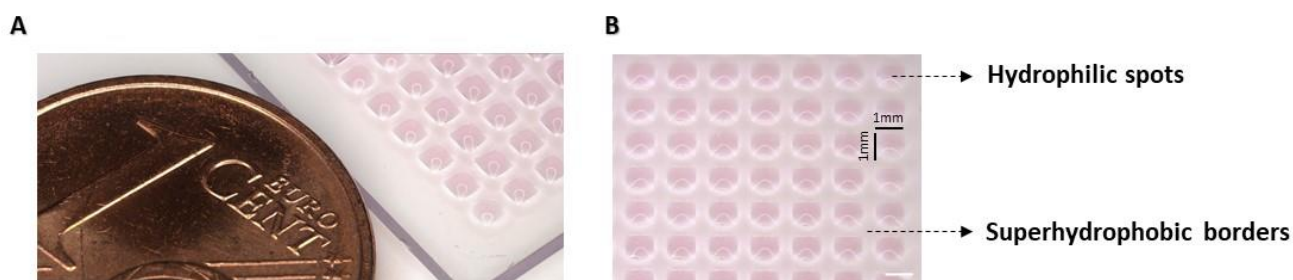


Figure 3. Photo of a part of Droplet Microarray (DMA). A) Comparison of the size of DMA spots to a 1-cent coin. B) The DMA platform features hydrophilic square-shaped spots, each measuring $1 \text{ mm} \times 1 \text{ mm}$, separated by superhydrophobic borders containing droplets of cell culture medium. Scale bar: 1 mm.

Early versions of DMAs, constructed from HEMA-EDMA polymers, encountered challenges such as uneven surface structure and a tendency to adsorb compounds. Therefore, for performing drug testing it required higher drug concentrations to achieve desired effects on cells. These drawbacks led to the development of the new coating by *Dr. Zheqin Dong* (unpublished), a more refined

version of the DMA, featuring a surface coated with silica nanoparticles. The nanoparticles, pre-functionalized with trimethoxyvinylsilane, are applied through spin-coating or spray-coating, and a UV-induced thiol-ene reaction is used to create the superhydrophobic and hydrophilic regions. The Z-Slide provides enhanced droplet stability, with highly repellant borders that allow for high-volume droplets that remain stable even when the slide is moved or inverted. The Z-Slide's surface is optimized for working with aqueous solutions, such as cell culture media, and reduces the issues associated with compound adsorption.

Due to the differences in wettability between the hydrophilic and superhydrophobic surfaces, liquid droplets can be trapped in each hydrophilic spot, creating a well-defined array format. This defined format allows researchers to accurately address each specific spot. Additionally, different reagents can be dispensed simultaneously onto various spots using liquid handling systems. The density of arrays and the size of each individual spot can be adjusted using different photomasks to suit the specific requirements of the experiments, enabling DMA to be applied to a wide range of samples and applications.

Miniaturization is a significant advantage of the DMA platform. The high-density array format and the ability to adjust spot sizes using various photomasks, allows for flexibility in experimental design. Arrays of square hydrophilic spots with side lengths of 1,000, 500, and 350 μm with 80, 9, and 3 nL volumes were successfully fabricated, of which the consumption were 600, 5,000, and 15,000 times less than that of 384-well plates, respectively.⁽⁹⁰⁾ This level of miniaturization reduces the volumes of reagents and samples required, significantly lowering the overall costs of experiments.

The ability to fabricate numerous spots on each slide makes DMA a powerful tool for high-throughput screening. Its compatibility with automated liquid dispensers accelerates workflows while minimizing human error. These dispensers can simultaneously dispense hundreds of spots in less than a minute, enhancing the platform's efficiency. Additionally, DMA can be integrated with other technologies, such as automated screening microscopes and printers, allowing for full automation of processes like sample dispensing and imaging, further improving the efficiency of high-throughput screening.

DMA's compatibility with a wide range of sample types, including biological samples like cells and 3D spheroids, chemical compounds, and materials such as hydrogels, along with its ability to integrate with other technologies, makes it a highly versatile tool for various experimental approaches (Figure 4).

In 2016, *Popova et al.* demonstrated the possibility of culturing adherent cell lines such as HEK293, HeLa, and A549 in droplet arrays ranging from 3 to 80 nL on the DMA platform. They introduced a single-step, pipetting-free medium exchange method, which allowed cells to be cultured on the DMA slide for up to five days. This process was followed by reverse transfection and small-molecule drug screenings within individual droplets. The miniaturization achieved in this study expanded the potential applications of live cell microarrays and drug screening on the DMA platform.⁽⁹⁰⁾

In 2021, *Chakraborty et al.* investigated cellular behavior when cultured on surfaces with different properties and in varying volumes. They conducted a transcriptomic analysis of HeLa-CCL2 cells cultured on multiple biocompatible surfaces used for DMA fabrication, with volumes ranging from 3 to 100 nL. Their findings revealed that HeLa-CCL2 cells cultured in nanoliter volumes, as small as 9 nL, on DMAs showed a transcriptomic profile similar to cells grown on conventional culture platforms. This highlights DMA's potential as a robust, miniaturized alternative for standard cell culture and high-throughput screening applications.⁽⁹¹⁾

Later in 2022, *Chakraborty et al.* performed the entire process of cell culture, lysis, mRNA isolation, and conversion of mRNA to cDNA on DMA slides using 200 nL droplets. Gene expression was then performed on obtained cDNA performing both qualitative gel electrophoresis and quantitative real-time polymerase chain reaction (PCR), demonstrating that the platform can support RNA analysis down to a single cell per droplet.⁽⁹²⁾

The DMA applications are not limited to 2D cell cultures. It has also been applied in the field of 3D cell structures, where uniform embryoid bodies were formed using a hanging droplet method. These 3D structures were then used for high-throughput drug screenings involving 774 FDA-approved compounds.⁽⁹³⁾ In addition, *Popova et al.* developed a miniaturized single-spheroid microarray of 3D spheroids on DMA slides using the hanging droplet method, presenting a novel approach for screening 3D cancer spheroids or microtumors.⁽⁹⁴⁾ This achievement led to another

study by *Cui et al.* where droplets containing spheroids were precisely merged to assemble multiple spheroids into complex multicellular architectures, further improving the resemblance of the 3D model to actual tissue.⁽⁹⁵⁾

Liu et al. expanded the application of DMA slide beyond cancer research and drug screening by using the human induced pluripotent stem cells (hiPSCs). They developed a workflow that allowed the seeding and immunostaining of hiPSCs in experimental volumes as low as 200 nL to assess the effects of recombinant human-derived proteins or protein mixtures coated on hydrophilic spots. By measuring the expression levels of several pluripotency markers, they identified 10 protein combinations that outperformed Matrigel in maintaining hiPSC pluripotency. Two of these conditions were successfully used to demonstrate the long-term culture and differentiation of hiPSCs on the DMA platform.⁽⁹⁶⁾

Lei et al. further demonstrated the application of the DMA beyond mammalian cell lines. The platform has been adapted for microbiological applications, such as the rapid generation of bacterial droplet arrays. In one study, a library of 2000 compounds were tested on carbapenem-resistant *Klebsiella pneumoniae* and methicillin-resistant *Staphylococcus aureus*, demonstrating DMA's capability for high-throughput antibacterial screening. By using a colorimetric readout method based on the metabolization of the tetrazolium dye in cell counting Kit-8, they developed a straightforward analysis which highlights the platform's adaptability for different types of bacteria and drug discovery efforts in infectious diseases.⁽⁹⁷⁾

Another example of DMA application beyond cell lines is the study by *Popova et al.*, where zebrafish embryos were individually cultured in 5 μ L droplets within single round spots of 3 mm diameter on a DMA slide. This setup allowed for treatment of embryos with fluorescently labeled peptides and toxicity screening via a sandwiching method.⁽⁹⁸⁾

Beyond biological applications, the DMA has also been used in material development, where an array of hydrogels with varying compositions was created and screened for their photodegradability.⁽⁹⁹⁾

The potential of DMA platform has been demonstrated across a wide range of biological applications (Figure 4). Many of them were usually carried out using microtiter plates with volumes

in the microliter range. DMA's capacity to handle volumes in the nanoliter range significantly reduces material consumption, allowing for a greater number of experiments to be conducted from a limited amount of starting material. As mentioned earlier, this is particularly important in cases involving patient-derived cells, where only a small quantity can be obtained without posing a significant risk to the patient. For instance, *Popova et al.* successfully used DMA for drug sensitivity and resistance testing of primary chronic lymphocytic leukemia cells. In this case, the material required for a single experiment was reduced to only 100 cells, 0.03 nmol of a compound, and 100 nL of medium, representing a 200-fold reduction in material compared to experiments performed in a 384-well plate.⁽¹⁰⁰⁾

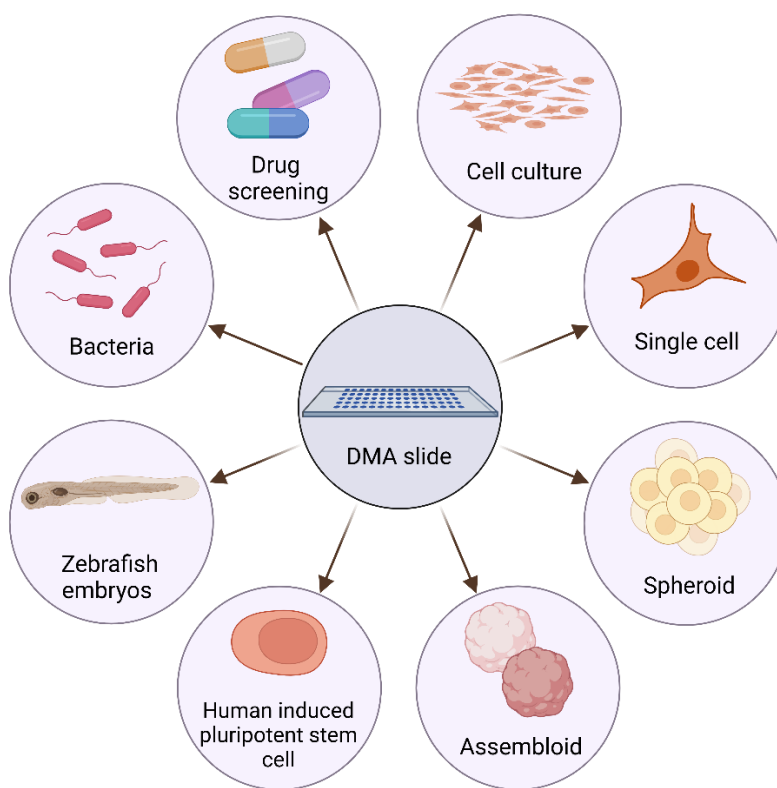


Figure 4. Overview of applications of the Droplet Microarray. From top left: Drug screening, Cell culture, Single cell culture, generating single spheroids, Assembloids, Culturing human induced pluripotent stem cell, Zebrafish embryos and Bacteria.

1.5. Objectives

Functional personalized oncology has the potential to significantly impact cancer treatment by offering a tailored approach for individual tumors. However, achieving such tailored treatments, particularly in solid tumors, requires innovative solutions that can overcome the limited availability of patient-derived samples and allow for rapid screening of multiple therapeutic options. This thesis is driven by the motivation to address this need by a miniaturized platform, Droplet Microarray (DMA) technology, providing a promising solution. By reducing the quantity of cells, drugs, and reagents required, miniaturization facilitates high-throughput drug sensitivity and resistance testing directly on primary patient-derived samples, which holds potential for rapid, individualized therapeutic screening.

Solid tumors, such as lung cancer and gliomas, represent some of the most challenging forms of cancer to treat due to their aggressive nature and complex biological behavior. Despite extensive research efforts, survival outcomes remain poor for many patients with these malignancies, highlighting an urgent need for more effective therapeutic strategies.

This thesis comprises three main chapters, each contributing to the aim of enhancing drug screening approaches for solid tumors:

1. **Developing a Miniaturized DSRT for Lung Cancer:** The first aim of this research is to develop a miniaturized DSRT platform using the DMA slide to rapidly evaluate the sensitivity of patient-derived lung cancer cells to chemotherapeutic agents, enabling high-throughput testing with minimal cell quantities, even from needle biopsies. This approach does not need time to expand and establish biological models for lung cancer, providing rapid workflow for personalized cancer treatment. The objectives of this study are:
 - 1.1. Establishing the protocol for tissue dissociation and cell isolation from surgical material
 - 1.2. Analyzing the tumor composition after cell isolation and also after 24 hours of incubation
 - 1.3. Establishing and validating the protocol for drug sensitivity tests for primary lung cancer cells using DMA slide

- 1.4. Investigating the influence of different cell densities on reproducibility and variability of drug sensitivity tests
 - 1.5. Investigating intratumor heterogeneity in drug sensitivity across distinct tumor regions
 - 1.6. Establishing the protocol for tissue dissociation and cell isolation from needle biopsy samples and validating the protocol for drug sensitivity tests
2. **High-Throughput Drug Screening on glioblastoma cells, exploring Combination Therapy with Decitabine:** The second aim of this thesis is to find novel therapeutic options for IDH1 wild-type glioblastoma by pre-treating cells with decitabine to enhance their sensitivity, followed by high-throughput drug screening to identify synergistic therapeutic combinations. The objectives of this study are:
- 2.1. Develop and optimize protocols for generating cell spheroids from IDH1 wild-type glioblastoma cell lines on a DMA slide.
 - 2.2. Investigate the effects of decitabine pre-treatment on cell viability and the ability of cells to form spheroids.
 - 2.3. Expose glioblastoma spheroids to a library of 722 CNS-penetrating drugs to identify potential therapeutic vulnerabilities.
 - 2.4. Evaluate drug responses under two conditions: pre-treatment with decitabine versus no pre-treatment. This analysis aims to determine whether decitabine sensitizes cells to therapy or induces resistance.
 - 2.5. Validate the identified hits, either as single agents or in combination with decitabine, using 384-well plate assays.
3. **Introducing Hydrogel-Based Cultures on the DMA Platform for High-Throughput Screening:** While liquid media-based cell culture on DMA slides is well-established, this study aims to expand the platform's capabilities by introducing a nanoliter-hydrogel array for the first time. The third aim of this thesis is to develop a stable nanoliter-volume hydrogel array capable of supporting cells and cell spheroids on the DMA chip. The objectives of this study are:
- 3.1. Establish protocols for incorporating cells into nanoliter hydrogel pads on the DMA slide.
 - 3.2. Evaluate the viability and proliferation of cells cultured within hydrogel pads over time.
 - 3.3. Confirm the stability of hydrogel pads on the DMA slide during washing procedures.

Objectives

- 3.4. Develop a method for gelating droplets containing spheroids on the DMA slide.
- 3.5. Design a protocol to selectively gelate specific droplets containing spheroids on the DMA slide and use a gelation-degelation cycle to sort the contents of selected spots.

This thesis aims to provide innovative tools and strategies for functional precision oncology, from lung cancer drug sensitivity testing to identifying potent glioblastoma treatments and developing hydrogel-based cultures and seeks to overcome key limitations in functional precision oncology approaches.

2. Results and discussion

2.1. Miniaturized drug sensitivity and resistance test on cells derived from lung cancer patients on Droplet Microarray platform

2.1.1. Project idea and background

Lung cancer is among the most common and deadly cancers globally, with a high mortality rate due to frequent late-stage diagnosis and aggressive nature. It is traditionally divided into two main subtypes: small-cell lung cancer (SCLC) and non-small-cell lung cancer (NSCLC). These categories are distinguished by their histological and genetic characteristics, with NSCLC representing approximately 85% of cases.⁽¹⁰¹⁾ NSCLC is further divided into adenocarcinoma, squamous cell carcinoma, and large cell carcinoma, each with unique histological features that influence prognosis and treatment choices. Adenocarcinoma is the most common subtype, originating from the mucus glands in the lungs, while squamous cell carcinoma arises from the flat cells lining the airway, and large cell carcinoma represents a more undifferentiated form of lung cancer. Tobacco smoking is a significant risk factor for lung cancer, yet there is a growing incidence among non-smokers, which highlights other risk factors like environmental pollutants, genetic predispositions, and exposure to carcinogens.⁽¹⁰²⁾

The era of personalized medicine for advanced NSCLC began in 2004 with the groundbreaking discovery of epidermal growth factor receptor (EGFR) mutations in patients who showed positive responses to the tyrosine kinase inhibitor gefitinib which shifted the ‘one-size-fits-all’ approach to personalized treatment choices based on molecular characteristics of the tumor, such as EGFR overexpression.⁽¹⁰³⁾ Today, multiple targeted therapies are approved for treatment of this type of cancer and this approach has shown a significant improvement in overall survival rates for many patients, with five-year survival rates ranging from 15% to 60%, depending on the specific biomarker targeted.⁽¹⁰⁴⁾ For instance, in Germany, around 30% of patients with advanced NSCLC have targetable genetic alterations.⁽¹⁰⁵⁾

Chemotherapy remains a standard treatment option for NSCLC, particularly for patients without actionable genetic mutations. Platinum-based doublet chemotherapy, which combines a platinum compound (cisplatin or carboplatin) with another agent, is the standard first-line approach.⁽¹⁰⁶⁾ The choice of the second agent depends on the histological subtype: pemetrexed is preferred for non-squamous NSCLC (e.g., adenocarcinoma),⁽¹⁰⁷⁾ while gemcitabine or paclitaxel is commonly used for squamous cell carcinoma.⁽¹⁰⁸⁾ Single-agent chemotherapy is often used for older patients, patients with poor performance status, or those unable to tolerate combination regimens. Drugs such as docetaxel, pemetrexed, or gemcitabine are frequently used in this context. While platinum-based doublets achieve higher response rates (30%-40%) compared to single agents, the latter offer reduced toxicity and better tolerability. For maintenance therapy, pemetrexed has demonstrated efficacy in prolonging progression-free survival for non-squamous NSCLC after initial treatment.⁽¹⁰⁹⁾

Despite these advancements, treatment response rates vary widely. For example, while targeted therapies often show initial high response rates (For example, 60%-70% for EGFR inhibitors), some patients develop resistance over time, leading to treatment failure.⁽¹¹⁰⁾ Chemotherapy response rates are even lower, with only 20%-30% of patients showing a significant response.⁽¹¹¹⁾ This highlights the need for strategies like DSRT to identify effective treatments tailored to individual patients.

As mentioned earlier, DSRT tests can help determining the most effective treatment, aiding in the design of personalized treatments for each patient. For these tests, patient-derived cells are usually cultured in microtiter plates, and the number of cells obtained from non-invasive biopsy might not be sufficient for the tests or could limit the number of drugs tested. For instance, *Kim, S. et al.* cultured patient-derived cells from lung cancer patients in 384-well plates (1000 cells per well) and exposed them to 64 chemotherapeutic agents.⁽³⁰⁾ Another example is organoids and *Kim, M. et al.* used organoids from five subtypes of lung cancer to test drugs targeting genetic alterations in the tumors.⁽⁷³⁾ Microfluidic systems, such as "organ-on-a-chip" models, offer another promising approach. *Ding, S. et al.* developed droplet Micro-Organospheres (MOS) for drug screening using patient-derived cells and exposed them to 119 FDA-approved drugs.⁽¹¹²⁾ Another example is PDX models, for instance, *Kita, K. et al.* established 10 PDXs from 30 patients with NSCLC and

demonstrated the use of a PDX model with an EGFR mutation for analyzing resistance to EGFR tyrosine kinase inhibitors.⁽¹¹³⁾

These methods demonstrate the potential of DSRT but highlight the challenge of limited cell availability. However, in most studies, in vitro tests rely on cells obtained after surgical removal of the tumor, which limits sensitivity profiling to patients undergoing surgery. Since many lung cancer cases are diagnosed at an advanced, inoperable stage, alternative methods for obtaining tumor cells are essential. For these patients, diagnosis relies heavily on extracting tumor cells for cytology or small tissue samples for molecular and morphological analysis, typically using image-guided core needle biopsy (CNB).⁽¹¹⁴⁾ Although CNB provides tissue for analysis, the amount of cells obtained is often limited. Since a significant portion of these samples is used for pathology and genetic profiling, there may be insufficient cellular material for DSRT.⁽¹⁷⁾

Miniaturization can be a promising solution to overcome this limitation by reducing the scale of testing platforms maximizing the utility of small biopsy samples. DMA slides enable the use of fewer cells and smaller volumes of reagents, allowing for a more comprehensive and efficient screening process. This miniaturized approach also increases throughput, enabling a broader range of drugs and conditions to be tested simultaneously, even with a limited cell sample. As a result, miniaturization not only makes DSRT more accessible for lung cancer patients with limited tissue samples but also supports faster and more personalized treatment decisions, contributing to the broader impact of functional precision oncology in lung cancer care.

This study is motivated by the need for a miniaturized DSRT method for lung cancer. The goal is to enable effective drug sensitivity testing using small quantities of cells from patient-derived lung cancer biopsies. This approach does not need time to expand and establish biological models for lung cancer. The focus will be on evaluating the sensitivity of lung cancer cells to a panel of 12 chemotherapy drugs that have been commonly used to treat this type of cancer over the past five years.

2.1.2. Tissue dissociation

Results and discussion

In this study, a miniaturized DSRT workflow for patient-derived lung cancer cells on the DMA slide is established. Figure 5 illustrates the concept and workflow of the miniaturized DSRT. The workflow was optimized on a DMA slide containing an array of 672 square hydrophilic spots, arranged in a 14×48 layout, each spot measuring $1 \text{ mm} \times 1 \text{ mm}$. Lung cancer tumor samples used in this study were collected within 24 hours post-surgery from patients diagnosed with stage I to III NSCLC who had not received any chemotherapy prior to surgery. Tumor samples were maintained in DMEM medium at 4°C during transport from the Thoraxklinik at the University Hospital of Heidelberg. The tumors ranged in size from $1.9 \times 1.8 \times 0.3 \text{ cm}$ (weighing 0.96 g) from Patient 1 to $3.1 \times 2.9 \times 0.4 \text{ cm}$ (weighing 4.19 g) from Patient 11, based on measurements of their largest dimensions.

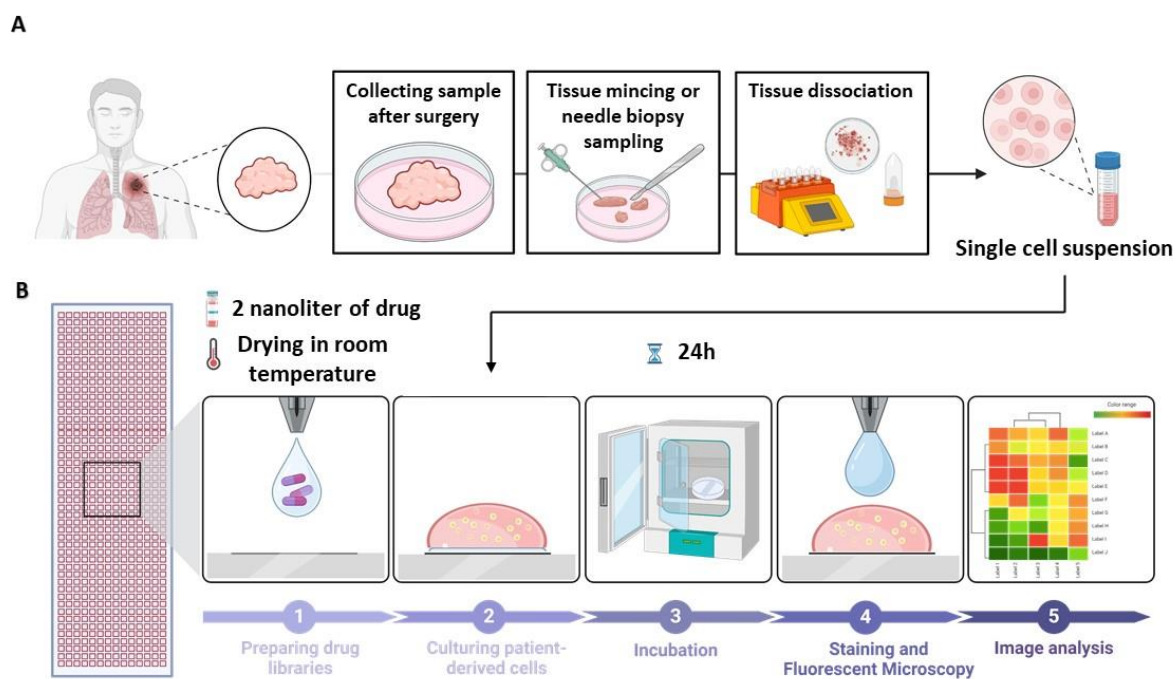


Figure 5. Concept and experimental workflow of miniaturized DSRT for patient-derived lung cancer cells on the DMA slide. A) Surgical material or artificial needle biopsies derived from surgical material, obtained from patients diagnosed with NSCLC are received after surgery and dissociated into a single-cell suspension. B) Drug libraries are prepared by dispensing 2 nL of drugs in desired concentration onto each

Results and discussion

spot of the DMA slide. The slides are dried at room temperature and stored in the dark dry conditions. The obtained cell suspension is then dispensed onto the pre-printed drug libraries, and cells are exposed to the drugs for 24 hours. Afterward, the cells are stained with fluorescent dyes Hoechst, Calcein-AM, and PI, and then imaged using an automated screening fluorescence microscope. The images are analyzed to determine cell viability.

In this study, two tumor dissociation methods were developed to isolate cell suspensions. The first method involved manually cutting tumor samples into 1–2 mm fragments using sterile scalpels, followed by mechanical dissociation through pipetting in a 50 mL Falcon tube. After centrifugation, Liberase DH (0.28 Units/mL) in DMEM medium was added to the pellet, and the sample was incubated on an overhead rotator at 37°C for 2 hours. The cell suspension was then filtered through 100 µm and 40 µm cell strainers to remove undigested tissue fragments. The filtered cells were resuspended in PBS and loaded on top of Histopaque, which, during centrifugation, separates high-density tumor components, such as red blood cells, allowing the remaining cells to be isolated. The resulting cell suspension was then diluted in culture medium. Cell count and viability data obtained with this method are shown in Table 1 for patients 4, 5, 6, 7, 8, and 9. On average, the method yielded 2.12×10^6 cells per tumor sample (calculated from six samples, standard deviation: 1.04) with an average viability of 72.66% (standard deviation: 11.5).

To shorten the isolation process, enable simultaneous processing of multiple samples, and increase the yield of isolated cells from tumors, a semi-automated dissociation approach was introduced using the gentleMACS™ Octo Dissociator with Heaters and its Tumor Dissociation Kit (Miltenyi Biotec). In this method, tumor samples were minced using two scalpels and placed into gentleMACS™ C Tubes containing an enzyme mix and DMEM medium. The tubes were then loaded onto the gentleMACS™ Octo Dissociator with Heaters, and the dissociation program was run for 1 hour. The resulting cell suspension was filtered through 100 µm and 40 µm strainers and loaded on top of Histopaque as described. The remaining samples (Table 1) were dissociated using this method, with corresponding cell counts and viability reported. On average, this method yielded 3.19×10^6 cells per tumor sample (calculated from thirteen samples: Patients 1, 2, 3, 10, 11, 12,

Results and discussion

and 13; standard deviation: 3.86), with an average viability of 75% (standard deviation: 13.72). Considering that samples from Patients 2, 12, and 13 were cut into three smaller pieces, each dissociated separately, these tissues were smaller in weight, ranging from 0.26 to 0.55 grams. This was significantly smaller than other tissues, where the smallest piece weighed 0.96 grams. The results show that the semi-automated dissociation approach increased the yield of isolated cells from tumors by raising the average number of isolated cells from 2.12×10^6 to 3.19×10^6 cells. This improvement is likely due to the gentleMACS™ Dissociator's ability to provide consistent and controlled mechanical dissociation across samples. The combination of automated mechanical processing and enzymatic digestion ensures thorough tissue dissociation.

These results indicate that cell viability was consistently high across surgical materials after tumor dissociation, ranging from 53% to 98%, with an average of 74.26% across all samples. Furthermore, between 0.21×10^6 and 13.8×10^6 cells were successfully isolated from each tumor, providing sufficient quantities for drug sensitivity testing. The observed variation in the number of cells isolated from each tumor likely reflects differences in tumor size, cellular density, and tissue characteristics, such as the presence of necrotic cells.

Results and discussion

Patient ID	Diagnosis	Sex	Age	Pathological stage	Total cells of tissue sample (x10 ⁶)	Cell viability after isolation (%)	Cell isolation method
Patient 1	Lung squamous cell carcinoma	male	80	IIB	13.8	90	Semi-automated
Patient 2-1					0.91	67	Semi-automated
Patient 2-2	Lung adenocarcinoma	male	60	IIIA	1.28	73	Semi-automated
Patient 2-3					1.26	84	Semi-automated
Patient 3	Lung adenocarcinoma	female	59	IB	6.35	86	Semi-automated
Patient 4	Lung adenocarcinoma	female	73	IIB	1.47	58	Manual
Patient 5	Lung adenocarcinoma	male	62	IIIB	1.49	89	Manual
Patient 6	Lung adenocarcinoma	male	69	IB	1.83	65	Manual
Patient 7	Lung squamous cell carcinoma	male	61	IIB	2.1	83	Manual
Patient 8	Lung squamous cell carcinoma	male	63	IA	1.64	69	Manual
Patient 9	Lung squamous cell carcinoma	male	78	IIB	4.2	72	Manual
Patient 10	Lung squamous cell carcinoma	male	56	IIIA	6.9	98	Semi-automated
Patient 11	Lung adenocarcinoma	male	68	IIB	2.3	78	Semi-automated
Patient 12-1					0.71	61	Semi-automated
Patient 12-2	Lung adenocarcinoma	female	70	IB	0.21	59	Semi-automated
Patient 12-3					0.21	53	Semi-automated
Patient 13-1					0.92	74	Semi-automated
Patient 13-2	Lung adenocarcinoma	female	61	IIIB	2.7	88	Semi-automated
Patient 13-3					3.87	64	Semi-automated
Patient 14	Lung adenocarcinoma	male	54	IIB	0.17	26	Manual
Patient 15	Lung large cell carcinoma	male	74	IIA	0.19	84	Semi-automated
Patient 16	Lung adenocarcinoma	female	85	IIIA	0.2	81	Semi-automated
Median (range)			65.5 (54-85)		1.48	73.5	

Table 1. List of patient-derived tumor samples used in the study. For each patient, the tumor type, number of viable isolated cells (in millions), post-isolation cell viability (%) and the method for cell isolation are provided. Patients are listed according to their appearance in the results section. Samples from Patients 2, 12, and 13 were each divided into three pieces, and cells were isolated from each piece separately. The number of isolated cells and the viability of isolated cells for each piece are provided. Eight artificial needle biopsies were obtained from the samples of patients 14, 15, and 16, which were dissociated into cell suspensions. The number of isolated cells and their viability for each sample are reported.

To confirm that cancer cells were present in the cell suspension, remained intact during tissue dissociation, and were still present after 24 hours, the incubation period for drug sensitivity testing, the isolated cells were stained with an anti-EpCAM (epithelial cell adhesion molecule) antibody

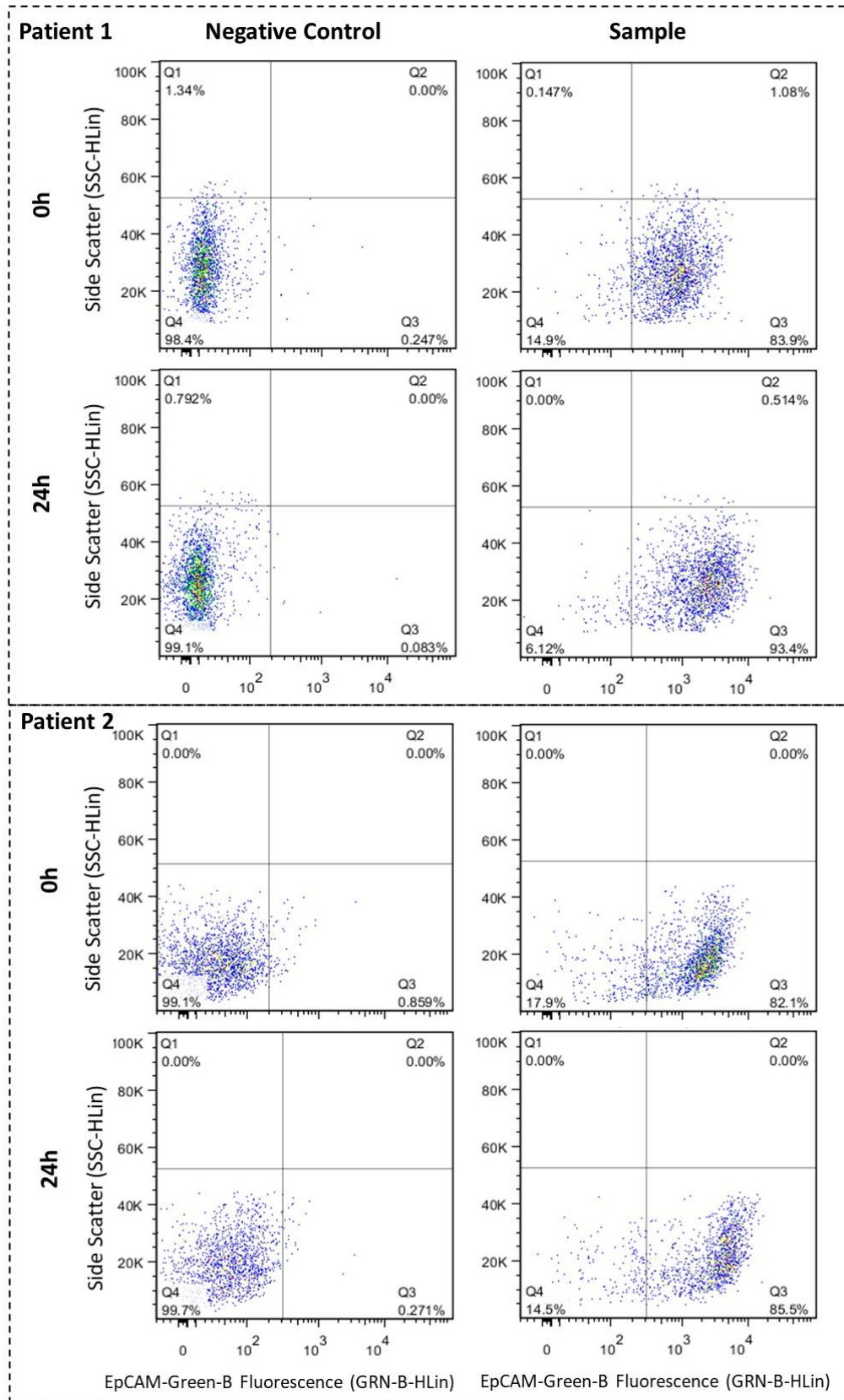
Results and discussion

and analyzed by flow cytometry. EpCAM is a well-known tumor antigen expressed in epithelial tumors, circulating tumor cells, and cancer stem cells.⁽¹¹⁵⁾

Identifying cancer cell biomarkers for all three subtypes of NSCLC can be challenging. Lung tumors can be highly heterogeneous, with different regions or cells within the same tumor exhibiting varied expression of biomarkers. This intra-tumor heterogeneity makes it challenging to rely on a single biomarker to identify cancer cells accurately across samples.⁽¹¹⁶⁾ Additionally, not all biomarkers are compatible with all detection techniques, such as flow cytometry. EpCAM was selected as a marker because all subtypes can express it; however, studies have shown that EpCAM expression can be low in lung cancer tumors,⁽¹¹⁷⁾ which may mean the actual number of cancer cells in the sample could be higher than detected.

To stain the cells with the anti-EpCAM antibody, one fraction of cells was stained immediately after isolation, and another fraction was cultured in a 6-well plate for 24 hours and then stained to ensure EpCAM-positive cells were not lost during the incubation period. Cells were washed with PBS to remove the culture medium, fixed with 4% paraformaldehyde, and then blocked with a Blocker BSA solution for 1 hour at room temperature. The samples were then incubated with the conjugated anti-EpCAM antibody overnight at 4°C. The following day, the samples were rinsed with PBS to remove unbound antibody and analyzed by flow cytometry, as shown in Figure 6. Each sample included two negative controls, one after cell isolation and one after 24 hours of incubation, in which the conjugated anti-EpCAM antibody was not added.

The results (Figure 6) indicate that the proportion of EpCAM-positive cells ranged from 71.6% to 83.9% immediately after cell isolation, and from 67.4% to 93.4% after 24 hours of incubation, confirming that cancer cells were present in the cell suspension, even after 24 hours of incubation.



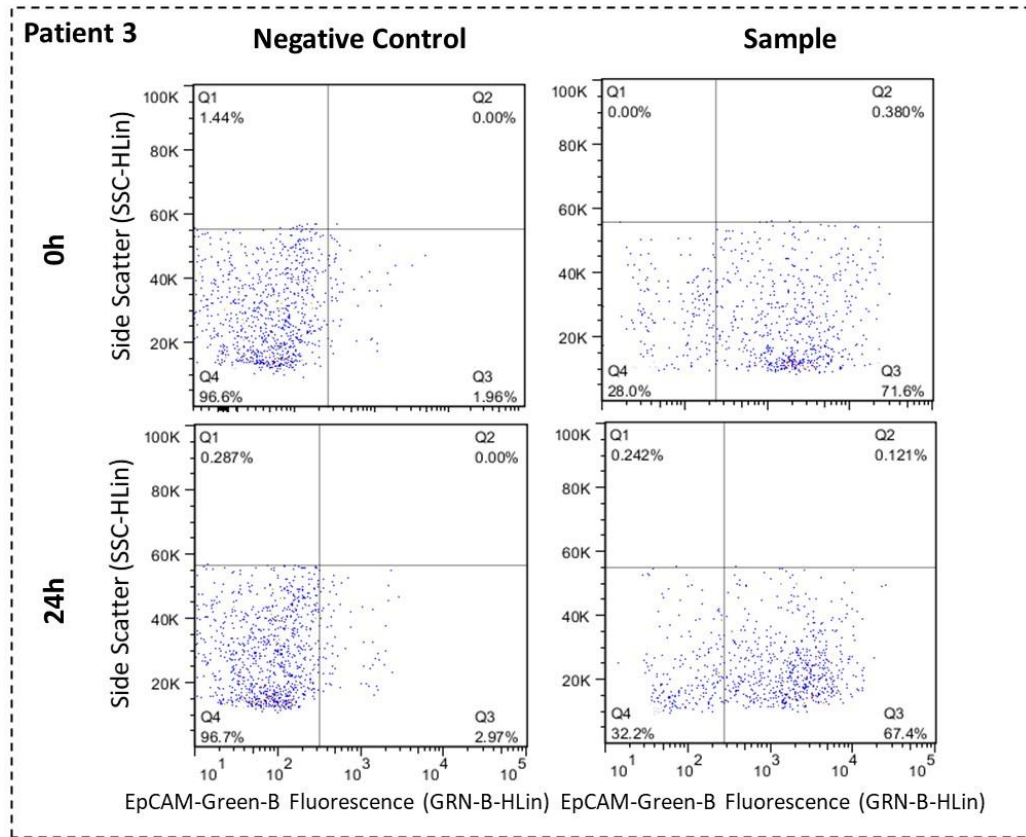


Figure 6. Detection of EpCAM-positive cancer cells in cell suspensions post-isolation and after 24-hour incubation. Cells were stained with a conjugated anti-EpCAM antibody detected in the Green B fluorescent channel. Cell populations were graphed as side scatter vs. Green B fluorescence, where Q4 represents the EpCAM-negative population and Q3 represents the EpCAM-positive population. Negative controls, without anti-EpCAM antibody staining, were included for each time point.

The concentration of isolated cells was adjusted to achieve 300 cells per 200-nanoliter droplet. To evaluate cell viability and variability of controls, cells isolated from Patient 9 were cultured on 134 spots of the DMA slide. Cells were dispensed on the DMA slide using an automated liquid dispenser IDOT-One. Humidity during dispensing was maintained at 70% using a humidifier connected to the IDOT-One. Following dispensing, the DMA slide was immediately placed inside a humidity-controlled Petri dish (referred to as a humidity chamber) and incubated in a standard cell culture incubator for 24 hours. After incubation, a staining solution containing Hoechst 33342,

Results and discussion

Calcein-AM, and Propidium Iodide (PI) was dispensed onto each spot using IDOT-One liquid dispenser. Each spot was imaged using an automated fluorescence microscope in brightfield and three fluorescent channels. Cell viability was calculated by dividing the number of live cells (Calcein-positive) by the total number of cells (Calcein-positive + PI-positive), as shown in Figure 7.

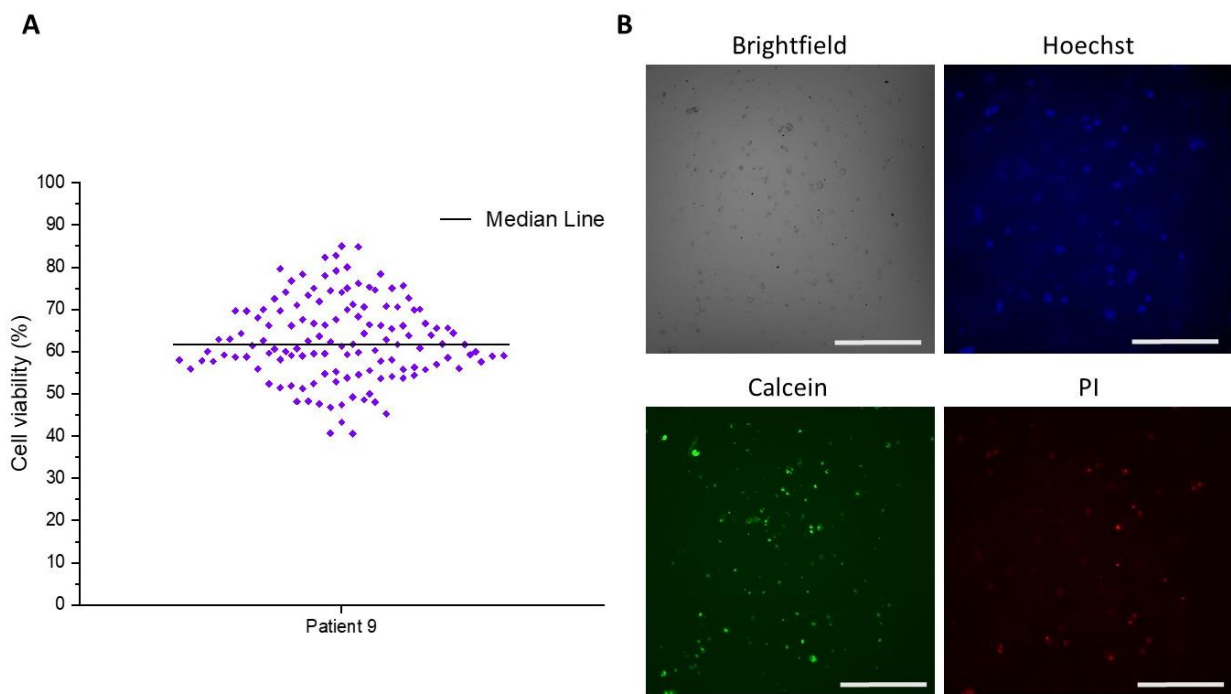


Figure 7. Cell viability of isolated tumor cells cultured on the DMA slide. A) A total of 300 cells per 200-nanoliter droplet were cultured on 134 spots of the DMA slide. After 24 hours of incubation, cells were stained with Hoechst 33342, Calcein-AM, and PI. Cell viability was calculated as the ratio of Calcein-positive cells to the total number of cells (Calcein-positive + PI-positive). B) Representative images of a single DMA spot containing isolated tumor cells stained with Hoechst 33342, Calcein-AM, and PI. Scale bar: 200 μm.

2.1.3. Drug sensitivity test on patient-derived cells

To perform drug sensitivity tests on patient-derived cells, drug libraries were first prepared. Twelve anticancer chemotherapy drugs commonly used in lung cancer treatment over the past five years were selected and printed on a DMA slide at five different concentrations, with five replicates for each concentration (Table 2). The drug concentrations were selected based on their IC₅₀ distribution for lung adenocarcinoma and lung squamous cell carcinoma, obtained from the Genomics of Drug Sensitivity in Cancer (GDSC) database.⁽¹¹⁸⁾ The concentrations were created through 2-fold serial dilution, maintaining a consistent dilution factor. Details of the drug names, mechanisms of action, and concentrations used in this study are provided in Table 2. For each drug, 10 mM stock solutions were prepared in DMSO. A non-contact dispensing system (Scienion) was used to print 2 nL of each drug solution onto each spot of the DMA slide. As a control, 2 nL of DMSO was also printed on the slide. The drug-printed DMA slides were dried in the dark at room temperature for 24 hours to ensure evaporation of the DMSO. The pre-dispensed slides were then stored in a dark box containing silica gel until use.

Results and discussion

Drug	Mechanism of action	Concentration (μM) C1-C5
Vinorelbine	Inhibition of microtubule polymerization	0.06 - 1
Pemetrexed	Inhibition of thymidylate synthase	6.25 - 100
Paclitaxel	Stabilization of microtubules, preventing depolymerization	0.06 - 1
Gemcitabine	Inhibition of DNA synthesis	0.06 - 1
Docetaxel	Stabilization of microtubules, preventing depolymerization	0.03 - 0.5
Etoposide	Inhibition of DNA topoisomerase II	1.8 - 30
Cisplatin	DNA cross-linking/alkylation	6.25 - 100
Carboplatin	DNA cross-linking/alkylation	6.25 - 100
Vincristine	Inhibition of microtubule polymerization	0.3 - 5
Topotecan	Inhibition of DNA topoisomerase I	0.6 - 10
Doxorubicin	Inhibition of DNA topoisomerase II, intercalation into DNA	0.06 - 1
Cyclophosphamide	DNA cross-linking/alkylation	6.25 - 100

Table 2. Anticancer cytotoxic drugs used in this study, including their mechanisms of action and the concentrations (in μM) at which they were tested. The concentrations range from C1 (lowest concentration) to C5 (highest concentration). These concentrations were created through 2-fold serial dilution, with each subsequent concentration being half of the previous one, maintaining a consistent dilution factor.

Chemotherapy targets not only cancer cells but also affects the broader cellular environment of the tumor, which plays a critical role in shaping therapeutic response. The interactions between cancer cells and other cellular components, such as immune cells, fibroblasts, and endothelial cells, are known to influence drug sensitivity and resistance.^(119, 120) Therefore, in this study, the entire cellular population isolated from each tumor was used for drug testing to capture these complex, clinically relevant dynamics and provide a more accurate representation of in vivo drug efficacy.

In total, 2×10^5 cells were used per library to assess cell viability in response to 12 drugs tested at 5 concentrations each, with 5 replicates per concentration. The concentration of isolated cells was adjusted to achieve 300 cells per 200-nanoliter droplet, which were printed onto pre-printed drug libraries using the IDOT-One liquid dispenser. After incubation, a staining solution containing Hoechst 33342, Calcein-AM, and PI was dispensed onto each spot. Each spot was then imaged

Results and discussion

using an automated screening fluorescence microscope in brightfield and three fluorescent channels. Cell viability was measured and is presented in Figure 8B.

In Figure 8B, the left panel shows drug response data for patients 4, 5, and 6, who were diagnosed with adenocarcinoma, while the right panel displays data for patients 7, 8, and 9, diagnosed with squamous cell carcinoma. Results showed that the platform effectively captured inter-patient variations in drug response. For example, in adenocarcinoma patients, vinorelbine reduced cell viability to 33.8% at 1 μ M in cells from patient 4, but to 58.5% and 57.0% in cells from patients 5 and 6, respectively.

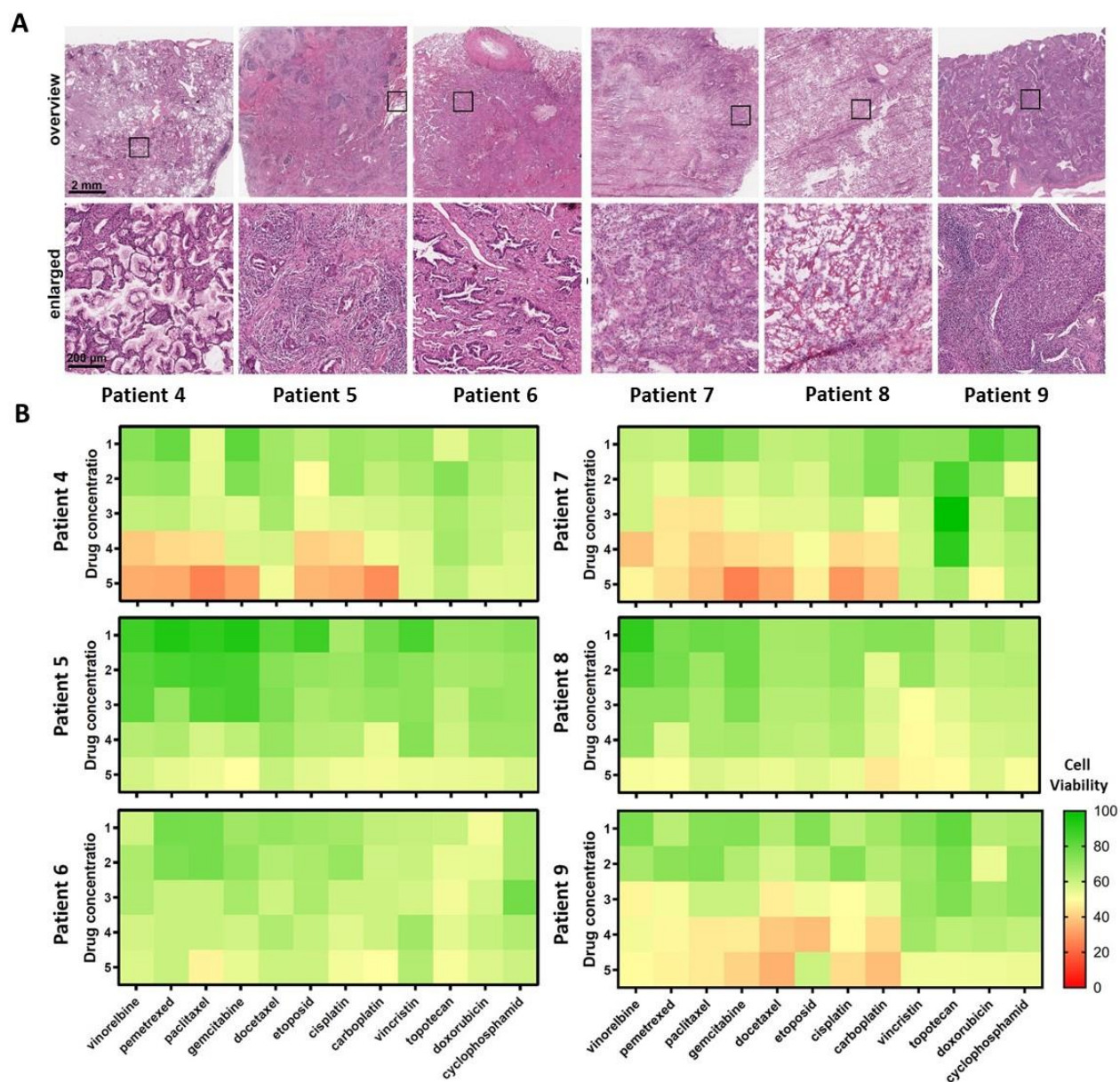


Figure 8. Drug sensitivity test on patient-derived cells. A) H&E staining of six NSCLC samples provided by pathology. The upper panel shows the full tissue sections, while the lower panel provides an enlarged view. Patients 4, 5, and 6 were diagnosed with adenocarcinoma, while patients 7, 8, and 9 were diagnosed with squamous cell carcinoma. B) Drug sensitivity results for the six samples after 24 hours of drug incubation. Cells were stained with a solution containing Hoechst 33342, Calcein-AM, and PI. Drug concentration 1 represents the lowest concentration, and Drug concentration 5 represents the highest. Green spots indicate cell viability greater than 60%, yellow spots indicate viability between 60% to 40%, and red spots indicate viability below 40%.

To study these variations more closely, dose-response curves for each drug were generated using data from cell viability assays after 24 hours of drug incubation, comparing the responses of six different samples to the same panel of drugs (Figure 9). The IC₅₀, which represents the half-maximal inhibitory concentration of a drug, was determined from the dose-response curves. The dose-response curves show the differences in drug sensitivity between the different patient's tumor. For example, the IC₅₀ for vinorelbine in Patient 4 was 0.37 μ M, whereas for Patients 5 and 6, 50% inhibition was not achieved within the tested concentration range. Additionally, Patients 7 and 9, both diagnosed with stage IIB squamous cell carcinoma, displayed similar responses to some drugs, such as carboplatin and cisplatin, with IC₅₀ values of 25.11 μ M and 24.54 μ M, respectively. However, they showed variation in response to doxorubicin, where Patient 7 reached an IC₅₀ of 1 μ M, while Patient 9 did not achieve 50% inhibition within the tested concentration range.

In a study by Wu M. *et al.*, cancer cell cultures established from the pleural effusion of a patient with NSCLC were used. A total of 1×10^4 cells were cultured in each well of a 96-well plate and treated with cisplatin, gemcitabine, pemetrexed, or docetaxel, or combinations of these drugs, for 48 hours.⁽¹²¹⁾ In another study by Andus I. *et al.*, three patient-derived cell lines of different NSCLC (Adenocarcinoma, squamous cell carcinoma and pleomorphic carcinoma) were generated and seeded in a 96-well plate ($1-2 \times 10^4$ cells per well) in 150 μ l/well standard medium and subjected to chemotherapy for 72 hours.⁽¹²²⁾ In contrast, our results demonstrate the platform's ability to detect patient-specific drug sensitivity using only 2×10^5 cells for the entire library of 12 anticancer drugs tested at 5 different concentrations with 5 replicates per concentration in nanoliter-volume droplets. Compared to the two studies mentioned, using microtiter plates, this represents a 90% reduction in cell usage (from 1×10^4 cells/well to 300 cells per droplet) and a 99.87% reduction in assay volume (from 150 μ l/well to 200 nanoliters per droplet). This represents a significant reduction in the number of cells and volume of the tests, offering a more efficient approach to drug screening.

Results and discussion

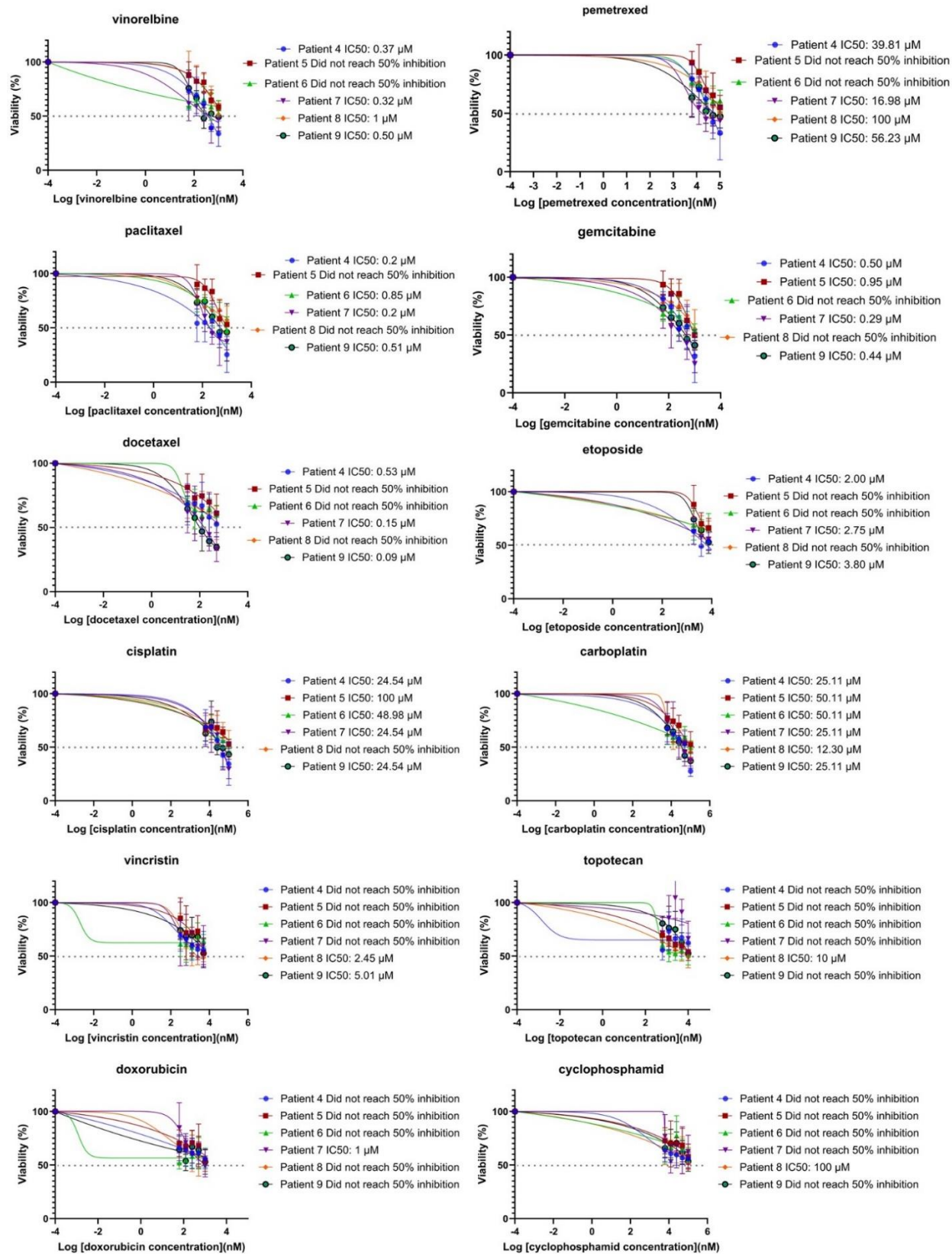


Figure 9. Comparison of dose-dependent effects of compounds on primary patient-derived cells cultured on a DMA slide. A total of 300 cells were cultured in 200-nanoliter droplets and exposed to drugs for 24 hours. After incubation, cells were stained with Hoechst 33342, Calcein-AM, and PI, and imaged using an automated fluorescence microscope. The IC₅₀ (half-maximal inhibitory concentration) of each drug was determined. The average was taken from five repeats, with error bars indicating standard deviations.

To evaluate how different number of cells can influence reproducibility, variability and statistics of drug responses, a dedicated workflow was designed, as illustrated in Figure 10. Drug libraries were prepared by dispensing four blocks of vinorelbine, pemetrexed, and doxorubicin at five different concentrations, with five replicates for each concentration on a single chip (Figure 10, Step I). The concentration of isolated cells (Figure 10, Step II) was then adjusted for four cell densities: 700, 500, 300, and 150 cells per 200-nanoliter droplet. Each cell density was printed in one block of the DMA slide containing the three drugs at varying concentrations, with all densities tested on the same chip (Figure 10, Step III). Cells were exposed to the drugs for 24 hours, followed by staining and imaging as previously described (Figure 10, Step IV).

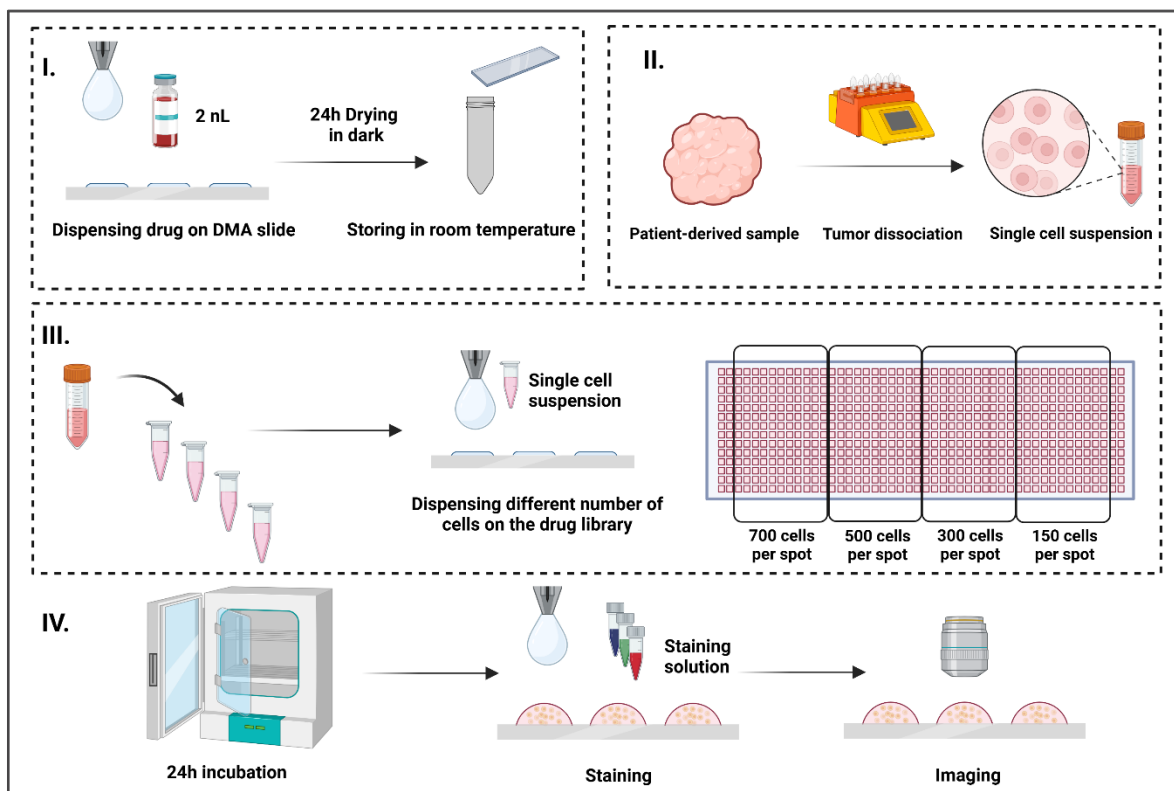


Figure 10. Workflow for evaluating the reproducibility of drug sensitivity tests on patient-derived cells. (Step I) Preparation of drug libraries by dispensing four arrays (11×14) of vinorelbine, pemetrexed, and doxorubicin at five concentrations with five replicates for each concentration on a single chip. (Step II) Adjusting the concentration of isolated cells to four cell densities (700, 500, 300, and 150 cells per 200-nanoliter droplet). (Step III) Printing of each cell density onto array of 11×14 on the DMA slide containing the drug libraries. (Step IV) Incubation of cells with drugs for 24 hours, followed by staining and imaging to assess cell viability and drug response reproducibility.

Figure 11 shows the results of drug sensitivity tests conducted on different cell densities using cells isolated from three patient-derived samples. Across all four cell densities (700, 500, 300, and 150 cells per spot), cell viability decreased consistently with increasing drug concentrations. The similarity of the graphs for 700, 500, and 300 cells per spot suggests that the drug testing platform delivers consistent and reproducible results at these densities. The effect of cell density on cell

Results and discussion

viability was evaluated as not significant, except for the Patient 10 sample exposed to doxorubicin, where significant effects were observed at 0.5 μM ($P < 0.0001$) and 1 μM ($P = 0.0030$). This result may be attributed to the higher variability observed at 150 cells per spot, indicating that assay performance may be more sensitive to cell density at lower levels.

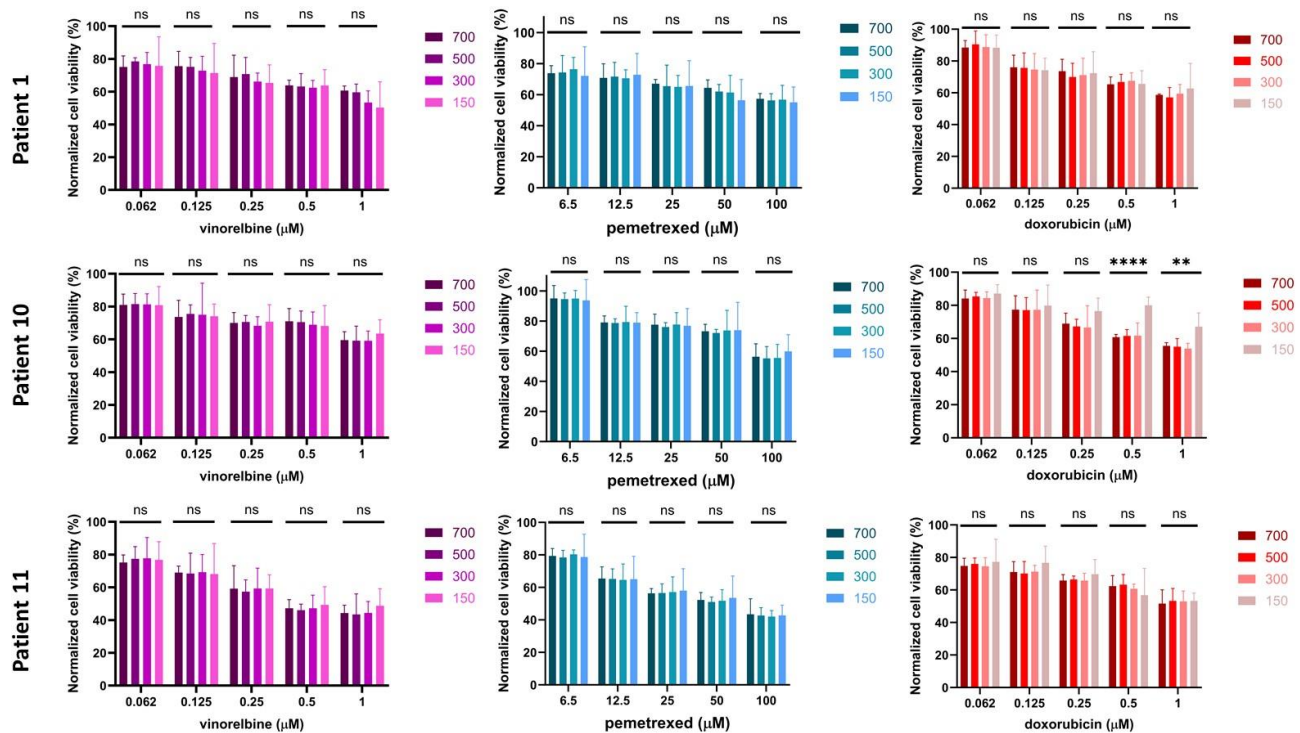


Figure 11. Reproducibility of drug sensitivity testing across different cell densities. The cell viability of cells subjected to three drugs (vinorelbine, pemetrexed, and doxorubicin) was normalized to DMSO control and is shown across three patient-derived samples. Each drug was tested at five concentrations, with each concentration represented by five replicates, across four cell densities (700, 500, 300, and 150 cells per 200-nanoliter droplet). Error bars indicate standard deviation derived from the five replicates at each concentration. The effect of cell density on cell viability was evaluated as not significant ($P = 0.2721$ – 0.9994), except for the Patient 10 sample exposed to doxorubicin, where the effect was extremely significant ($P < 0.0001$) at 0.5 μM concentration and significant ($P=0.0030$) at 1 μM concentration. Statistical significance was determined using one-way ordinary ANOVA, with highly significant differences (****p

Results and discussion

< 0.0001, *** p < 0.001, ** p < 0.01) for comparisons between different groups, while “NS” indicates nonsignificant statistical difference between the data groups.

One of the major challenges in precision oncology is intratumor heterogeneity, the presence of genetically and phenotypically distinct cell populations within a single tumor. This heterogeneity can contribute to differences in drug sensitivity among various regions of the tumor, impacting treatment efficacy and potentially leading to partial drug response and tumor recurrence.^(123, 124) To investigate this, the current study assessed drug sensitivity across distinct regions of patient-derived tumors.

To evaluate if it is possible to capture intratumor variation in drug responses, each tumor was divided into three sections (Fig. 12A), with cells isolated separately from each region. Then the isolated cells were printed onto 3 copies of a drug library to assess the variability in their responses. After a 24-hour exposure to the drugs, cells were stained with a staining solution and imaged to analyze viability and response (Fig. 12B).

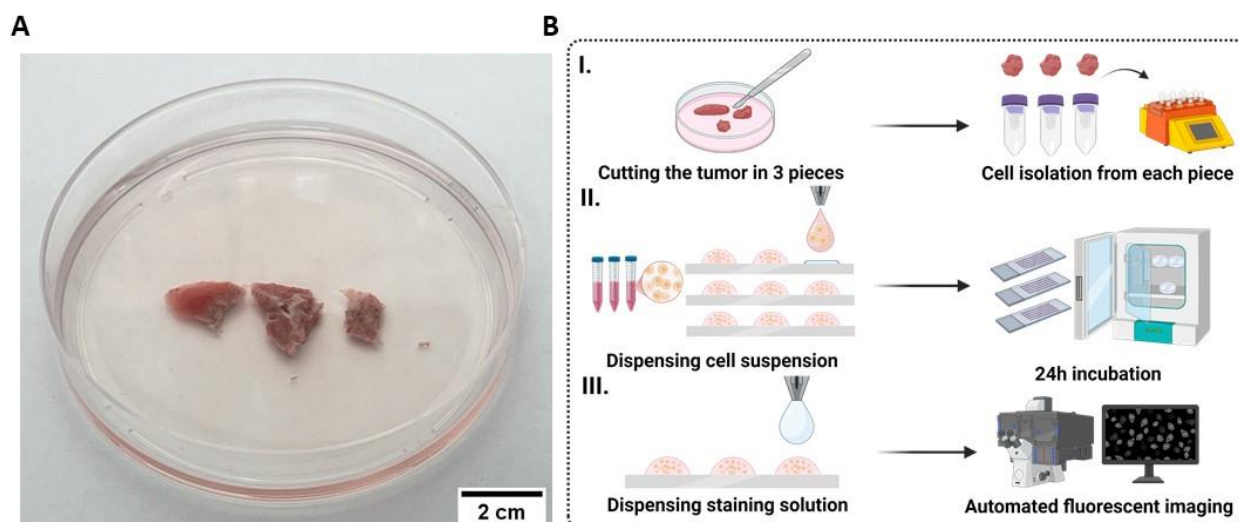


Figure 12. Workflow of evaluating intratumor heterogeneity in drug sensitivity across distinct tumor regions. A) Each tumor was divided into three sections to capture potential intratumor variation. B)

Results and discussion

Schematic workflow of the intratumor heterogeneity drug sensitivity test. In Step I, cells were isolated separately from each section. Each cell population was diluted to achieve a concentration of 300 cells per 200 nanoliters and dispensed onto a drug library containing 12 anticancer drugs at 5 different concentrations, with 5 replicates per concentration (Step II). Following a 24-hour incubation, cells were stained with a staining solution and imaged (Step III).

Three tumors were assessed using this method; however, only the results from the first tumor are presented in Figure 13, as analysis of the other two samples is ongoing. Figure 13A displays the drug sensitivity responses of cells derived from each section of the tumor to a panel of 12 anticancer drugs in three different heatmaps. Figure 13B shows the dose-response curves for each drug, comparing the responses of three different sections from Patient 12. These dose-response curves were generated using data from cell viability assays after 24 hours of drug incubation. The IC₅₀ was determined from the dose-response curves. The curves show the differences in drug sensitivity between the different regions of the patient's tumor. For example, across the tumor sections, responses to vinorelbine, gemcitabine, and topotecan were consistent, showing no significant differences in sensitivity. However, slight variations in drug response were observed for some drugs. For example, cisplatin decreased cell viability in all three sections, but the second and third section showed a stronger response, with the IC₅₀ of 15.48 and 13.38 μ M respectively, compared to section one, which showed a reduction to 16.98%. Another example is carboplatin, with the IC₅₀ of 16.21 and 13.18 in section one and three respectively, whereas in section two IC₅₀ was 33.11 μ M.

While this analysis only included half of the tumor, divided into three sections, the findings suggest that intratumor heterogeneity may impact drug response, though the sample size may have been too small to capture the full extent of this variability. Nevertheless, the results highlight the potential of sampling different regions of a tumor to explore the variation in drug sensitivity. This approach could allow clinicians to better understand how heterogeneity within a tumor might

Results and discussion

influence treatment efficacy and to tailor drug choices according to the specific responses of different tumor regions.

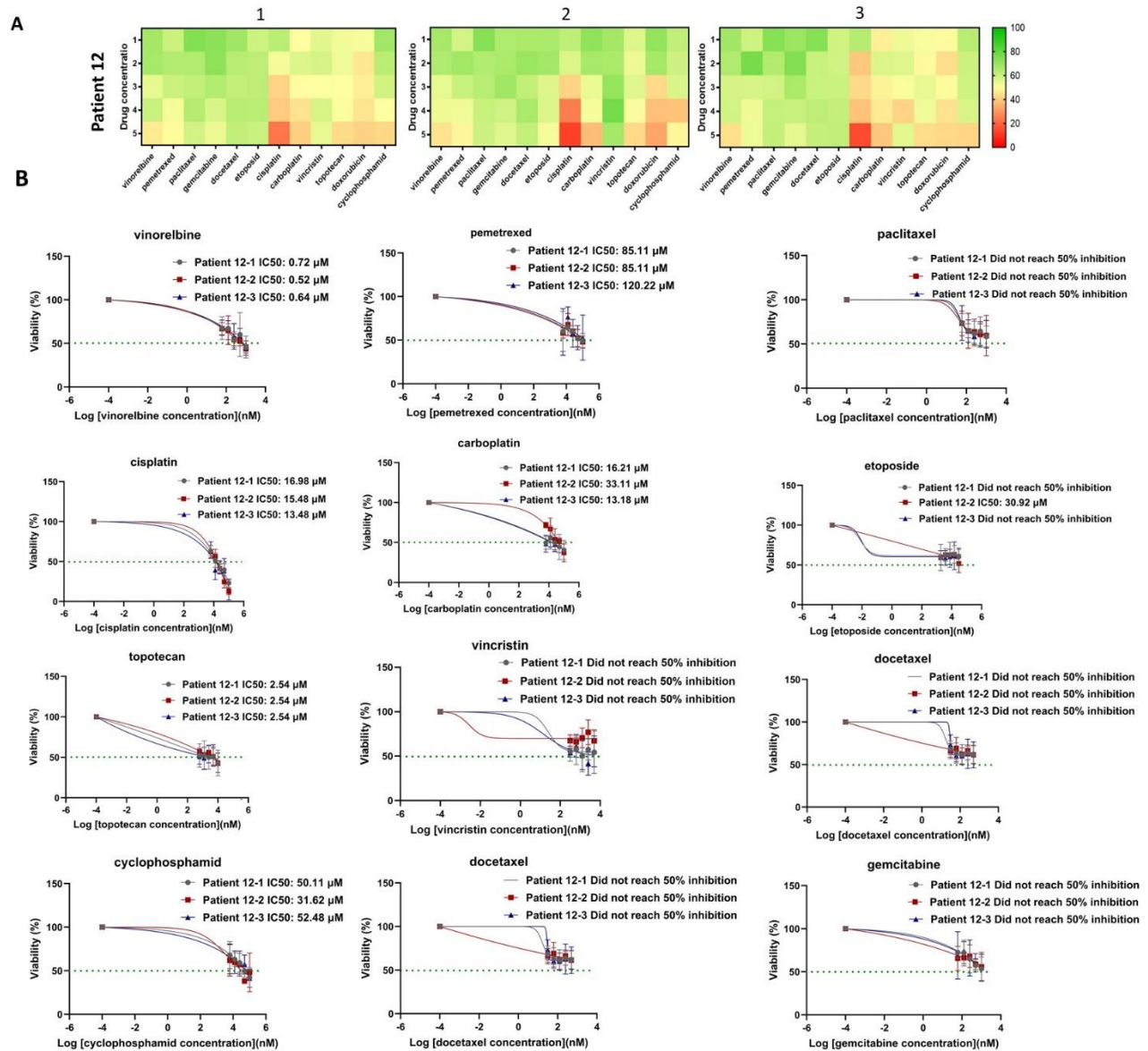


Figure 13. Drug sensitivity across different regions of a single tumor specimen. A) Each heatmap represents the drug responses of one section of the tumor to 12 anticancer drugs which corresponds to the left (1), center (2) and the right (3) section. Drug sensitivity results were assessed after 24 hours of incubation with drugs. Cells were stained with a solution containing Hoechst 33342, Calcein-AM, and PI. Drug

Results and discussion

concentration 1 represents the lowest concentration, and Drug concentration 5 represents the highest. Green spots indicate cell viability greater than 60%, yellow spots indicate viability between 60% to 40%, and red spots indicate viability below 40%. B) Dose-response curves generated using data from cell viability assays after 24 hours of drug incubation from cells isolated from three sections of Patient 12's sample. Viability percentages at different drug concentrations were plotted, and the curves were fitted using nonlinear regression analysis. The IC₅₀ (half-maximal inhibitory concentration) of each drug for each section was determined using the curves. The average was calculated from five repeats, and error bars represent standard deviations.

So far, the application of drug sensitivity tests is largely limited to tumors obtained through surgical resection. This means that the current approach may primarily benefit patients who undergo surgery. However, for patients with advanced-stage cancers or metastasis, tissue samples are typically collected through needle biopsies, which yield a much smaller amount of cellular material.⁽¹¹⁴⁾ This limited cell count poses a significant challenge, as it may not be sufficient for traditional drug sensitivity testing.⁽¹⁷⁾

To address this problem, the potential of the DMA platform for conducting drug sensitivity tests on needle biopsy-derived cells was investigated. A total of 8 artificial biopsies were obtained from 3 different tumors, weighing approximately 0.02 g each, the minimum tissue size that the gentleMACS device can reliably process. To maximize the yield from these small samples, cell isolation procedures were adjusted: only a single 100 μ m cell strainer was used to remove undigested tissue while retaining as many viable cells as possible (Figure 14B, Step I). Table 1 shows the results of cell isolation, revealing that cells derived from biopsies of patient 14 had a viability of only 26%, which was too low for drug sensitivity tests. However, cells isolated from patients 15 and 16 yielded in total 0.19×10^6 and 0.2×10^6 cells, respectively, sufficient for drug sensitivity testing. The concentration of cells was adjusted to 300 cells per 200-nanoliter droplet and printed onto the pre-dispensed drug libraries, as previously described (Figure 14B, Step II). After 24 hours of drug incubation, cells were stained and imaged to assess viability (Figure 14B, Step III).

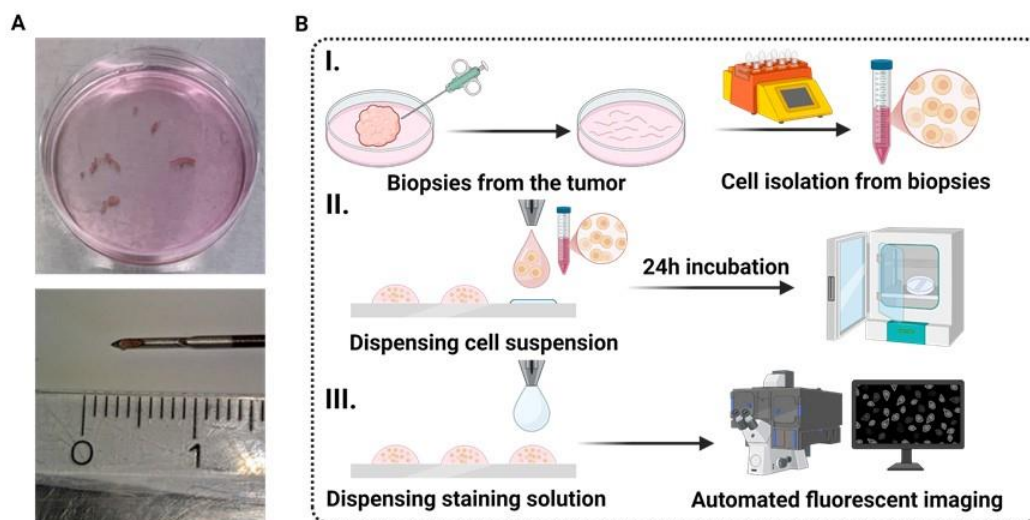


Figure 14. Workflow for drug sensitivity testing using needle biopsy samples. (A) Eight artificial biopsies obtained from a tumor (upper panel) and a close-up showing biopsy size (lower panel). (B) Schematic workflow of the drug sensitivity testing on needle biopsy samples: Biopsies were taken from a resected tumor and processed to obtain a single-cell suspension (Step I). Isolated cells were diluted to a concentration of 300 cells per 200-nanoliter droplet and dispensed onto a drug library containing 12 anticancer drugs at five concentrations, with five replicates per concentration (Step II). Following a 24-hour incubation, cells were stained and imaged (Step III).

Figure 15A shows the results from patient 15 and patient 16's biopsy-derived cells, highlighting the platform's effectiveness in performing DSRT on limited samples such as needle biopsy samples. However, due to a technical issue during image acquisition, some images for Patient 16 were lost and image analysis was not possible for some drug concentrations, as indicated by a cross sign in the heatmap. Figure 15B shows the dose-response curves for each drug, comparing the responses of biopsy-derived cells from Patient 15 and Patient 16. These dose-response curves were generated using data from cell viability assays after 24 hours of drug incubation. The IC₅₀ was determined from the dose-response curves. The curves illustrate the differences in drug sensitivity between the two patients' cells. For example, the responses to topotecan varied between the two samples: in Patient 15 the IC₅₀ was 0.81 μ M while Patient 16 did not achieve 50% inhibition within

Results and discussion

the tested concentration range. This highlights the variability in drug sensitivity between the two patients' cells.

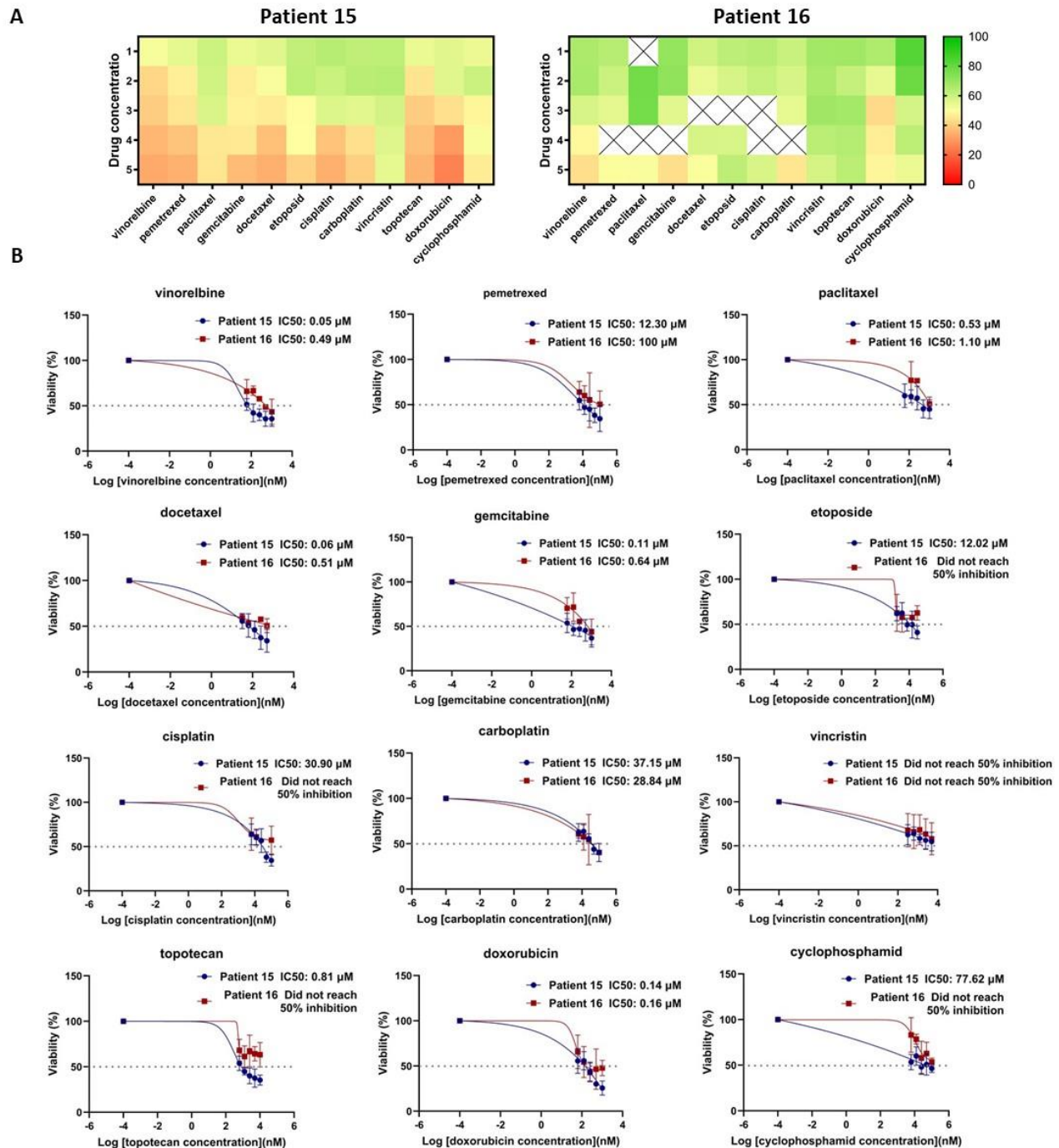


Figure 15. Drug sensitivity testing using needle biopsy samples. A) Drug sensitivity results for the two artificial needle biopsy samples after 24 hours of drug incubation. Cells were stained with a solution containing Hoechst 33342, Calcein-AM, and PI. Drug concentration 1 represents the lowest concentration,

and Drug concentration 5 represents the highest. Green spots indicate cell viability greater than 60%, yellow spots indicate viability between 60% to 40%, and red spots indicate viability below 40%. Some spots could not be analyzed due to technical issues during image acquisition, and these are marked with a cross sign. B) Dose-response curves generated using data from cell viability assays after 24 hours of drug incubation from cells isolated from Patient 15's and Patient 16's artificial needle biopsies. Viability percentages at different drug concentrations were plotted, and the curves were fitted using nonlinear regression analysis. The IC₅₀ (half-maximal inhibitory concentration) of for both samples was determined using the curves. The average was calculated from five repeats, and error bars represent standard deviations.

2.1.4. Summary

Lung cancer remains one of the leading causes of cancer-related death worldwide, NSCLC accounts for approximately 85% of lung cancer cases. Advances in personalized medicine have shifted treatment strategies for NSCLC from standardized approaches to personalized tailored therapies based on the tumor's molecular characteristics. However, personalized treatment selection faces challenges, especially for patients diagnosed with advanced, inoperable stages, where small cell samples from core needle biopsies are often the only available source of tumor cells.

DSRT plays a critical role in identifying effective treatments but is typically limited to tumors obtained through surgical resection, which yields millions of cells. For patients who rely on needle biopsy for diagnosis, limited cellular material often restricts the application of DSRT. Additionally, time is an important factor; patients with advanced-stage cancer cannot afford to wait for the weeks or months required to expand and establish in vitro models. This study addresses these limitations by developing a miniaturized DSRT platform using DMA technology, enabling efficient testing directly on cells isolated from patient-derived lung cancer biopsies. By using a scaled-down approach, the DMA platform requires fewer cells and smaller reagent volumes, allowing for rapid and comprehensive screening with small biopsy samples, without the need for extended cell expansion.

In this study tumor samples were obtained from patients with stage I to III NSCLC post-surgery and dissociated into single-cell suspensions using two methods: manual dissociation with Liberase DH and a semi-automated gentleMACS™ Octo Dissociator. Drug libraries comprising 12 commonly used chemotherapy drugs were printed on the DMA slide at five concentrations. Isolated cells were printed onto the pre-dispensed slides and incubated for 24 hours. Viability was assessed using fluorescence staining and imaging. In addition, the cell isolation method was optimized for isolating cells from needle biopsy samples to maximize the yield of cells obtained from these minimal samples.

The miniaturized DSRT platform demonstrated the ability to test drug sensitivity with as few as 300 cells per spot, showing consistent and reproducible results. The platform captured both inter- and intra-patient variability in drug responses. The study also explored intratumor heterogeneity by analyzing drug responses from three distinct tumor regions, revealing differences in sensitivity to certain drugs like cisplatin. Furthermore, the platform successfully conducted DSRT on cells derived from artificial needle biopsies, demonstrating its potential for miniaturized DSRT tests.

The miniaturized DSRT platform using the DMA slide represents a significant advancement in precision oncology. By requiring minimal cell input, it facilitates drug sensitivity testing even for patients with limited tumor material, enabling more personalized and rapid treatment decisions. This approach provides a high-throughput, efficient solution to overcome the limitations of traditional DSRT methods.

2.2. High-Throughput Screening to Uncover Therapeutic Vulnerabilities in Decitabine-Treated Glioma cells using Droplet Microarray

2.2.1. Project idea and background

Gliomas are a diverse category of primary brain tumors that include glioblastoma (GBM), astrocytoma, and oligodendroglioma. Among these, GBM is the most aggressive and frequently occurring one, more than 60% of all brain tumors in adults.⁽¹²⁵⁾ Despite the variety of modern therapies available for GBM, it remains a deadly disease with an extremely poor prognosis.

Standard treatments for gliomas include surgical resection, radiation, and chemotherapy with agents such as temozolomide.⁽¹²⁶⁾ However, these therapies often lead to limited success and glioblastoma progression, despite standard care.⁽¹²⁷⁾ Less than 5% of glioblastoma patients survive 5 years after their initial diagnosis and this rate has hardly improved over the past century and this emphasizes the critical need to identify and develop new treatment strategies.⁽¹²⁸⁾

Epigenetics plays an important role in the development and progression of glioblastoma, as it involves reversible modifications to the genome that regulate gene expression without altering the DNA sequence itself.⁽¹²⁹⁾ The two key modifications include DNA methylation and histone modifications, which can impact tumorigenesis and therapeutic response in GBM. In GBM, abnormal DNA methylation patterns, such as the silencing of tumor suppressor genes and the activation of oncogenes, are commonly observed.⁽¹³⁰⁾ The dysregulation of these epigenetic processes not only contributes to the malignancy of GBM but also complicates treatment strategies, as epigenetic alterations can lead to drug resistance and tumor recurrence.⁽¹³¹⁾ Understanding these epigenetic mechanisms offers potential for targeted therapies that could restore normal gene expression patterns, providing a promising avenue for improving the treatment of GBM.

In recent years, using epigenetic therapies for solid tumors has emerged, with the potential to disrupt tumor cell epigenetics and sensitize them to existing chemotherapies.^(132, 133) Among these, decitabine (DAC), a DNA methyltransferase inhibitor, has shown particular promise in reactivating silenced tumor suppressor genes, potentially sensitizing the cells to chemotherapy.^(134, 135) It works by incorporating into DNA and inhibiting DNA methyltransferase enzymes (DNMTs), which are responsible for adding methyl groups to cytosine residues in DNA. By inhibiting DNMTs, decitabine leads to a gradual loss of DNA methylation marks, specifically at CpG sites.⁽¹³⁶⁾ This hypomethylation can reactivate the expression of tumor suppressor genes and other genes that are often silenced in cancer due to abnormal methylation, potentially restoring more normal cellular function and making cancer cells more susceptible to other treatments.⁽¹³⁷⁾ DAC is already utilized in treating certain hematological malignancies,⁽¹³⁸⁾ and there is growing interest in its role as a part of combination therapies for solid tumors, particularly in tumors with complex epigenetic landscapes like gliomas.

Combining decitabine with other therapeutic agents in solid tumors is an area of active investigation however, despite DAC's therapeutic promise, its clinical application in gliomas has been limited by challenges in model development. Preclinical glioma models are difficult to culture due to the low proliferation of primary patient-derived tumorspheres (PDTs).⁽¹³⁹⁾ This lack of robust models for gliomas restricts the potential for drug discovery.

In this study, screening of a library of 722 CNS-penetrating compounds is being performed on patient-derived 3D tumorsphere cell lines with and without decitabine pre-treatment, with the goal to identify those that show greater therapeutic potential when combined with DAC. This approach is designed to assess whether pretreatment with decitabine reveals potential therapeutic vulnerabilities in gliomas.

To facilitate these screenings, the DMA platform is used. The DMA platform generates hundreds of nanoliter-scale droplets, supporting single tumorsphere array, making it particularly suitable for drug testing in slow-growing glioma cells. With reduced reagent consumption, the DMA platform allows for high-throughput, cost-effective screenings.

This research aims to broaden the therapeutic landscape for glioblastoma patients by introducing scalable, efficient methodologies to identify drug combinations with enhanced efficacy in DAC-pretreated cells.

2.2.2. Culturing glioma spheroids

In this study, two patient-derived glioma tumorspheres were used, L0125 and L0512 (provided by Prof. Dr. Sevin Turcan, Neurology Clinic and National Center for Tumor Diseases, University Hospital Heidelberg, Germany). L0512 cells grow as cell spheroids while L0125 cells grow as cell aggregates in culture. As the first step, the hanging drop method was employed to rebuild the 3D structure of the cells on the DMA, aiming to recapitulate the 3D growth characteristics of the PDTs. The DMA used in this study consisted of 672 square hydrophilic spots (1 mm × 1 mm). Previous studies have demonstrated the DMA platform's ability to generate a single 3D cell spheroid per droplet using the hanging drop method with HeLa, MCF-7, and HEK293 cell lines.⁽⁹⁴⁾

To demonstrate spheroid formation on the DMA slide using the hanging drop method, MCF-7 cells, commonly used in previous studies, were chosen. In this procedure, an anti-adherence rinsing solution was applied to coat hydrophilic spots and minimize cell adhesion on DMA spots. Initially, the anti-adherence rinsing solution was dispensed onto the DMA spots and allowed to dry. A cell suspension was then dispensed onto the treated DMA spots, and the slide was immediately inverted after dispensing. The inverted slide was placed on a 'Spheroid table' to culture cells using the hanging drop method. Here, a single spheroid array was formed using the MCF-7 breast cancer cell line (Figure 16). The MCF-7 cells were dispensed onto spots coated with the anti-adherence solution, which prevented the cells from adhering to the surface. Instead, the cells adhered to each other, forming cell aggregates, as shown in Figure 16. Over time, these aggregates became more compact, resulting in the formation of round spheroids.

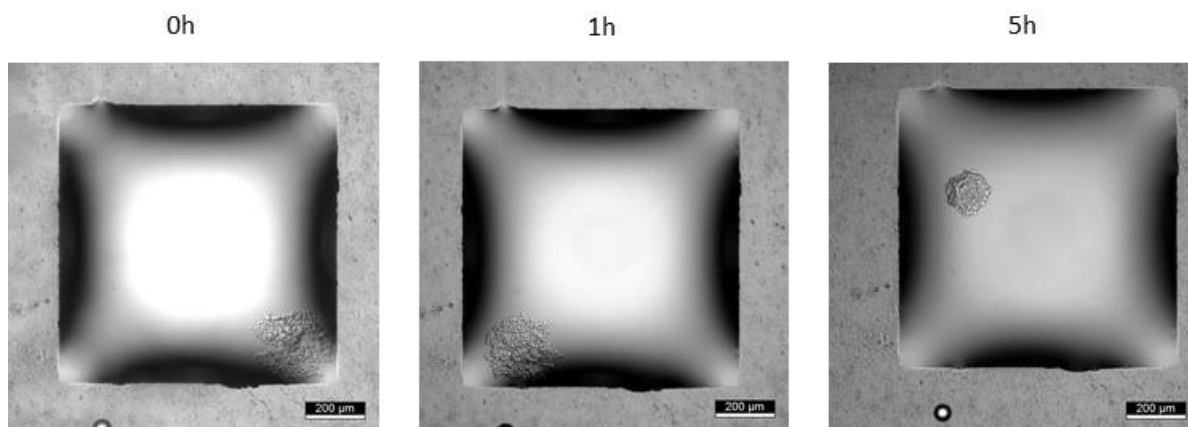


Figure 16. Formation of a single cell spheroid on a spot of the DMA slide. 500 MCF-7 cells were dispensed in the volume of 200 nL on the DMA slide and incubated in an inverted position for 24 hours. After dispensing, the cells begin attaching to each other (0 hours), forming a cell aggregate after 1 hour, which becomes more compact after 5 hours, leading to the formation of a single roundish cell spheroid on the DMA slide. Scale bar: 200 μm .

Results and discussion

To ensure that the hanging drop method is compatible with L0125 and L0512 tumorspheres and can be used to create cell spheroids for these lines on the DMA slide, the concentration of both cell lines was adjusted to 300 cells per droplet with a volume of 200 nanoliters and printed onto a separate DMA slide with spots coated with the anti-adherence rinsing solution. The slide was then inverted, with the spots facing down, and placed on a Spheroid Table inside a humidity-controlled petri dish. The slides were incubated for 48 and 72 hours. After each incubation period, some spots on the slide were stained with Calcein-AM and imaged using a fluorescence microscope, as shown in Figure 17. These images confirmed that both cell lines were able to form single cell spheroids using the hanging drop method on the DMA slide.

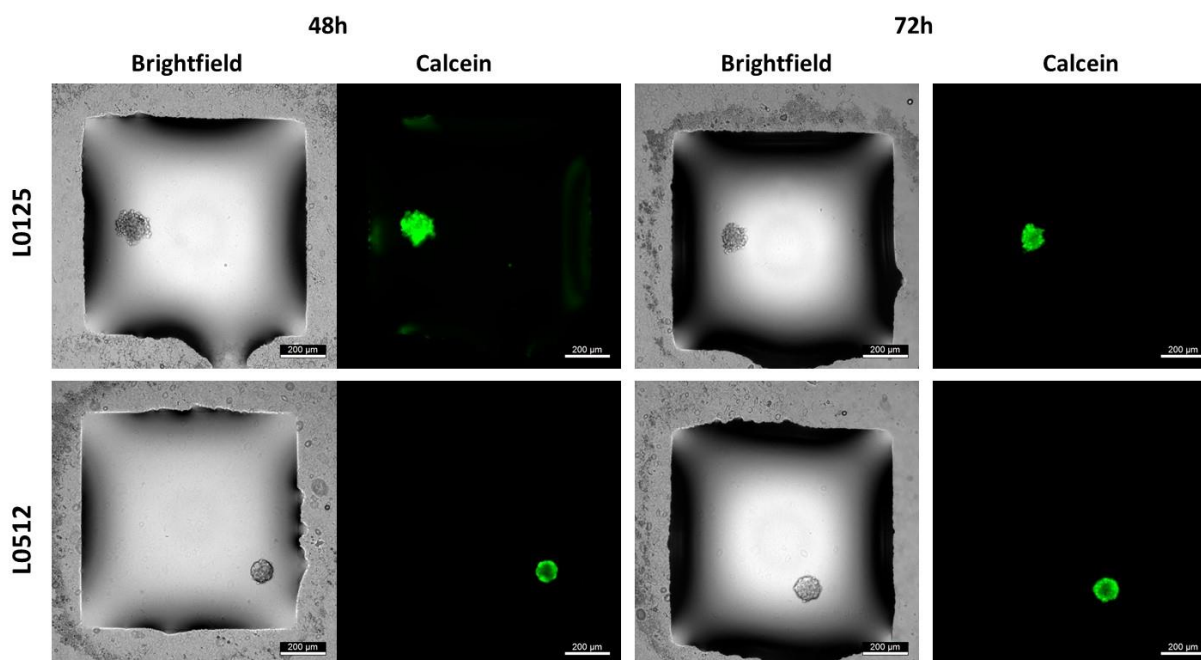


Figure 17. Single-cell spheroids of L0125 and L0512 on DMA slides. The upper panel shows L0125 spheroids formed after 48 hours (left) and 72 hours (right) in brightfield and Calcein channel. The lower panel shows L0512 spheroids formed after 48 hours (left) and 72 hours (right) in brightfield and Calcein channel. 300 cells per droplets of 200 nL were dispensed on the DMA spots. The slides were incubated for 48h and 72h in an inverted position. After incubating, cells were stained with Calcein. Scale bar: 200 μm.

To determine the optimal cell number per spot for generating single spheroids on the DMA slide, varying conditions were tested, with 300 to 600 cells per droplet in a 200-nanoliter volume, across 24 and 48 hours for the L0125 cell line. Cells were printed onto a DMA slide pre-coated with an anti-adherence rinsing solution, and the DMA slide was then inverted, with the spots facing down, on a Spheroid Table. After 24 hours, the slide was imaged in brightfield (Figure 18A) and subsequently incubated in a humidity chamber for an additional 24 hours before being imaged again. The images were then processed using Grid Screener, a tool for estimating grid parameters and extracting grid elements which was developed in collaboration with Prof. Markus Reischl, Institute for Automation and Applied Informatics (IAI). Using the grid data, Grid Screener facilitated spot-wise processing to automatically measure the diameter of single spheroids cultured on the DMA slide in brightfield.⁽¹⁴⁰⁾

The diameters of L0125 cell spheroids, cultured under different cell densities on the DMA slide, were measured after 24 and 48 hours of incubation, as shown in Figures 18B and 18C, respectively. The results indicated that spheroids formed successfully across all tested cell densities, with spheroid diameters increasing after 48 hours of incubation compared to 24 hours. To meet the objective of miniaturization, a density of 300 cells per spot was selected for further experiments and screenings.

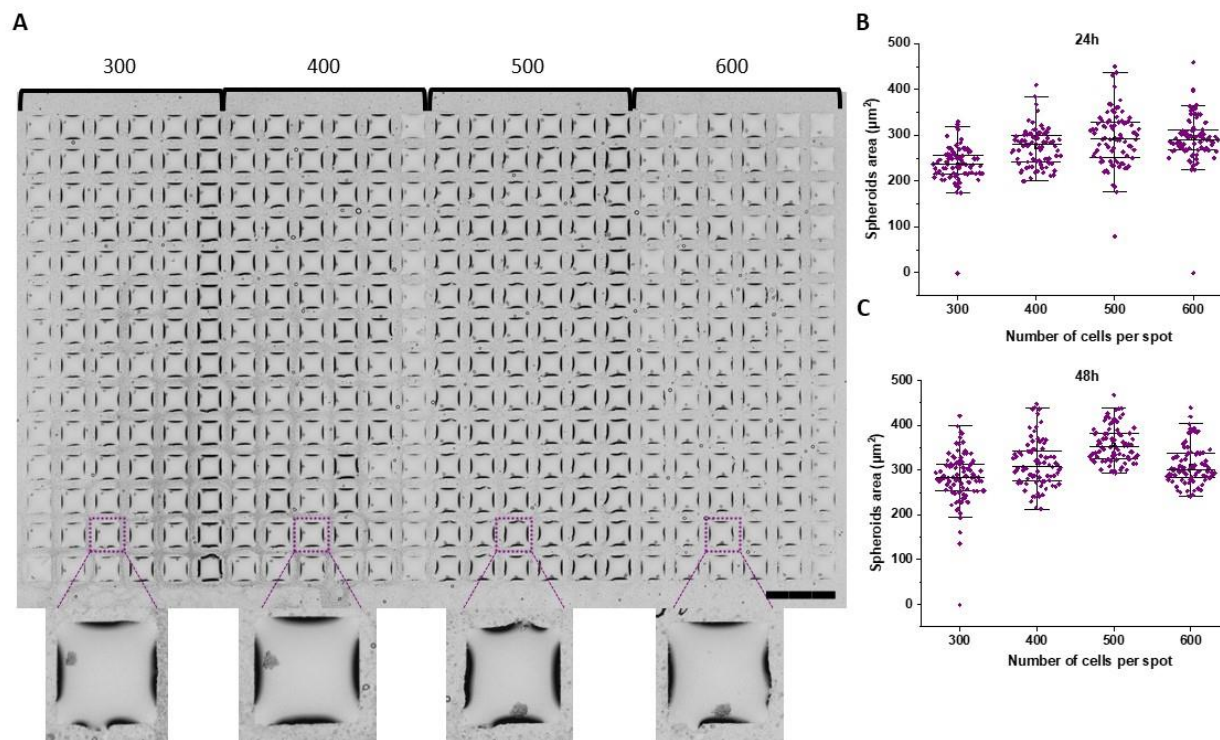


Figure 18. Optimization of cell density for single spheroid formation on DMA slide using L0125 cells. A) Array of 14×24 spots on a DMA slide, showing spheroids formed after 24 hours of incubation from 300, 400, 500, and 600 L0125 cells per droplet in a 200-nanoliter volume using the hanging drop method. Scale bar: 3 mm. The lower panel displays a close-up of one representative spot from each block, with each spot measuring 1×1 mm. B) Diameter of spheroids generated from 300, 400, 500, and 600 L0125 cells per droplet after 24 hours of incubation on the DMA slide, measured in brightfield using Grid Screener. C) Diameter of spheroids generated from 300, 400, 500, and 600 L0125 cells per droplet after 48 hours of incubation on the DMA slide, measured in brightfield.

To optimize cell density for spheroid formation of the L0512 cell line on the DMA slide, cell densities ranging from 300 to 600 cells per droplet in a 200-nanoliter volume were tested. After printing the cells onto a DMA slide pre-coated with an anti-adherence solution, the slide was inverted onto a Spheroid Table and incubated in a humidity-controlled environment. Brightfield images were captured after 24 hours (Figure 19A), and the slide was incubated for an additional 24

Results and discussion

hours before imaging again. The Grid Screener tool was used to analyze these images, enabling spot-wise diameter measurements of the spheroids.

Diameter measurements for L0512 spheroids at different cell densities after 24 and 48 hours of incubation are shown in Figures 19B and 19C, respectively. The results confirmed that spheroids formed successfully across all tested cell densities, with spheroid diameters increasing over time. Based on these findings and to maintain miniaturization, 300 cells per spot was chosen for the following experiments and screenings.

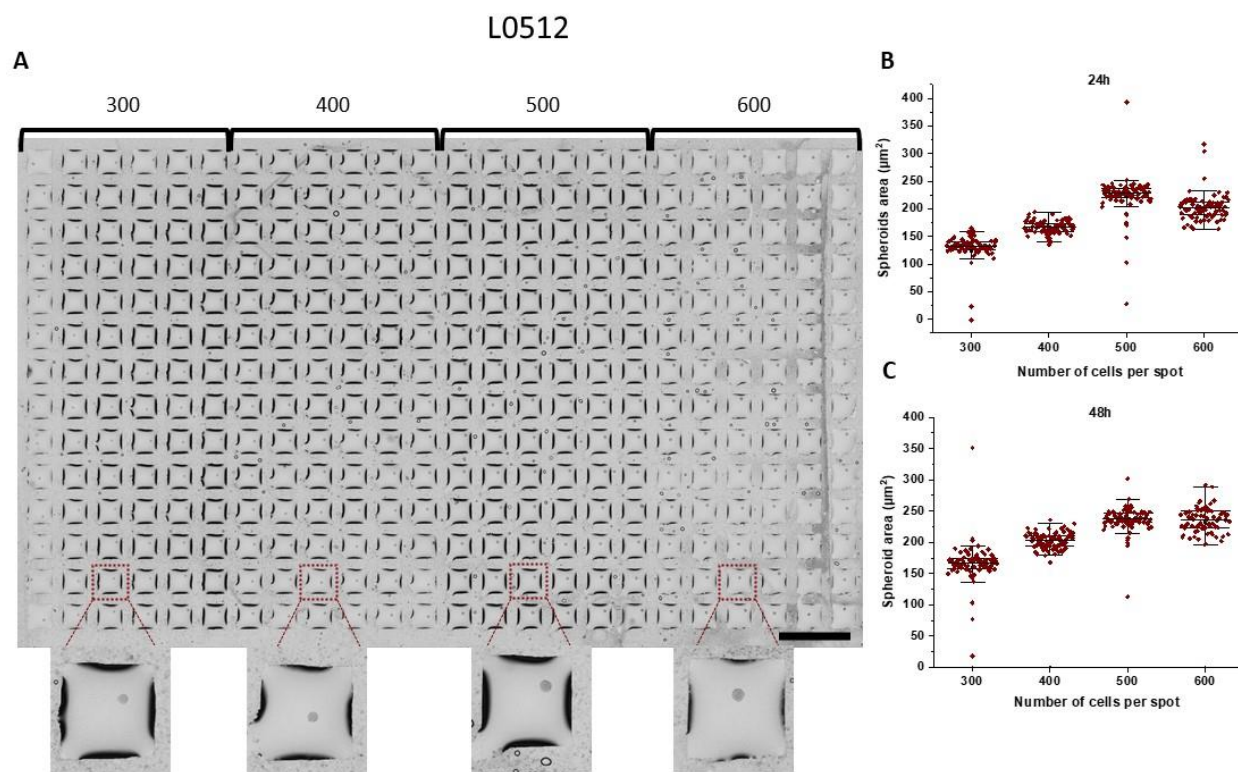


Figure 19. Optimization of cell density for single spheroid formation on DMA slide using L0512 cells. A) Array of 14 × 24 spots on a DMA slide, showing spheroids formed after 24 hours of incubation from 300, 400, 500, and 600 L0512 cells per droplet in a 200-nanoliter volume using the hanging drop method. Scale bar: 3 mm. The lower panel displays a close-up of one representative spot from each block, with each spot measuring 1 × 1 mm. B) Diameter of spheroids generated from 300, 400, 500, and 600 L0512 cells per

Results and discussion

droplet after 24 hours of incubation on the DMA slide, measured in brightfield using Grid Screener. C) Diameter of spheroids generated from 300, 400, 500, and 600 L0512 cells per droplet after 48 hours of incubation on the DMA slide, measured in brightfield.

In the next step, the growth of spheroids generated from 300 cells per spot in 200-nanoliter droplets over 7 days on the DMA slide was investigated. Cells were printed onto a DMA slide pre-coated with an anti-adherence rinsing solution, and the slide was then inverted, with the spots facing down, on a Spheroid Table. The slide was incubated in a humidity-controlled environment for 7 days, with brightfield images captured every 24 hours (Figure 20A). Images were processed using Grid Screener to measure the diameter of single spheroids cultured on the DMA slide.

The diameters of spheroids from both cell lines over the 7-day period are shown in Figure 20B. Results indicated that spheroid diameters increased over time; however, as no medium change was performed, the growth of L0512 spheroids stopped after 72 hours, while L0125 spheroids showed increased size variation over time. The culturing period for spheroids on the DMA slide could be extended up to 14 days with medium changes using a sandwiching method.⁽¹⁴¹⁾ However, since the drug screening in this study did not require longer culture durations, medium change techniques were not applied here.

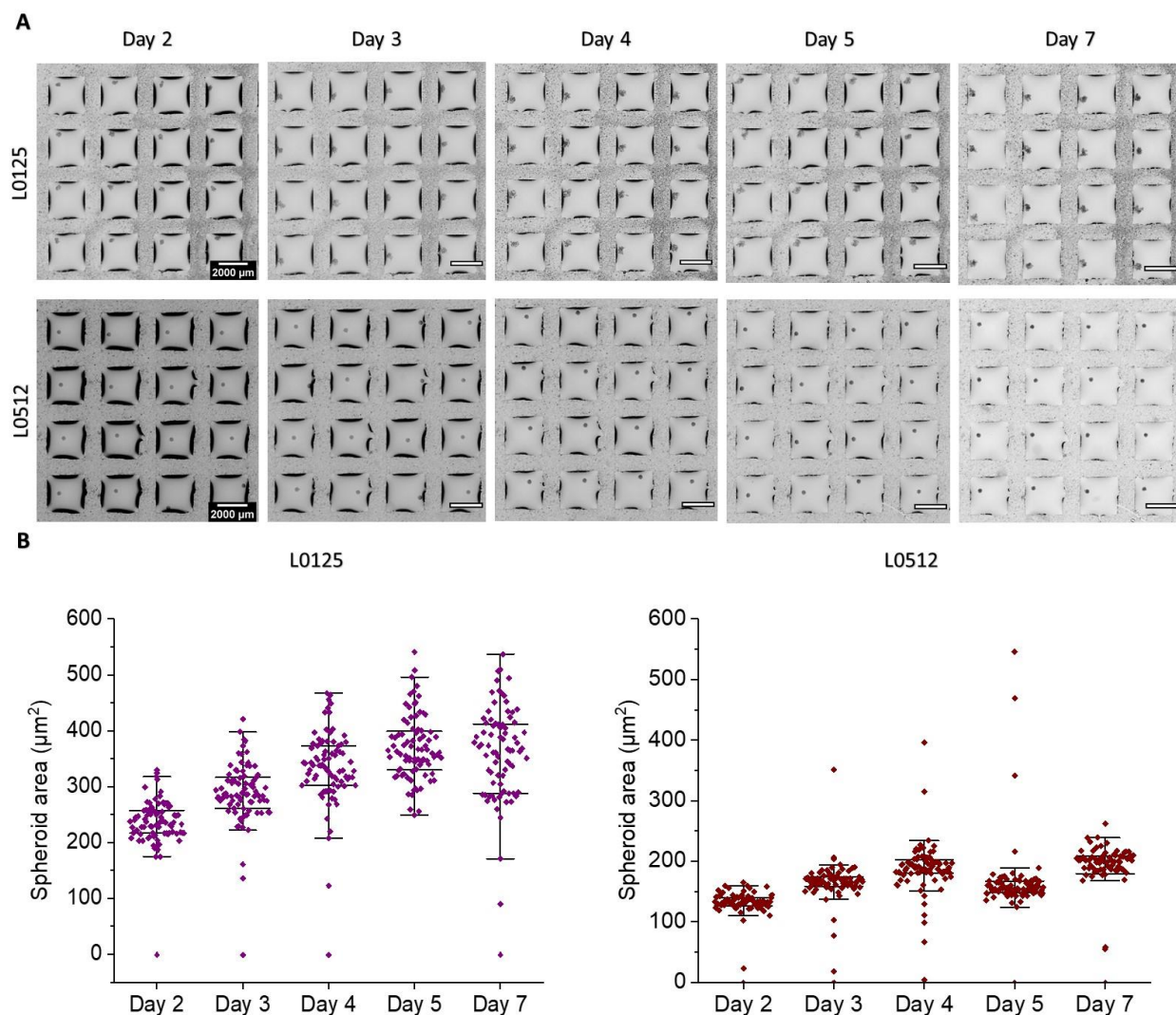


Figure 20. Culture and growth analysis of single spheroids on DMA slide over 7 days. A) Brightfield images of a 4×4 array on the DMA slide showing single-cell spheroids cultured over 7 days. Day 1 represents the day cells were printed on the slide, and Day 2 is 24 hours post-printing. Scale bar: 1 mm. B) Diameter measurements of spheroids generated from 300 L0125 cells (left panel) and L0512 cells (right panel) per droplet over 7 days of incubation on the DMA slide, obtained using Grid Screener in brightfield.

Decitabine is a DNA methyltransferase inhibitor and has shown potential in reactivating silenced tumor suppressor genes by inhibiting DNMT enzymes responsible for DNA methylation. Through

Results and discussion

this inhibition, decitabine promotes hypomethylation at CpG sites, potentially restoring tumor suppressor gene expression and sensitizing cancer cells to chemotherapy.^(136, 137)

The possible effects of decitabine on cell viability and spheroid formation were evaluated prior to high-throughput drug screening. Pre-treatment with decitabine was performed on L0125 and L0512 glioma cell lines. 3×10^5 cells of each line were seeded into two wells of a 6-well plate. After an initial 24-hour incubation, cells were tested in two conditions, with or without decitabine. Cells were harvested from each well: one sample was centrifuged and resuspended in standard culture medium, and the other was resuspended in medium containing 250 nM decitabine.

Following treatment period, cells were collected and prepared as single-cell suspensions. Cell viability was assessed using Trypan blue, showing that decitabine treatment resulted in decreased viability for both cell lines: L0125 cells had a viability of 77% post-treatment compared to 89% for untreated cells, while L0512 cells showed 81% viability with decitabine versus 86% without. These results confirmed that decitabine-treated cells retained sufficient viability for subsequent drug screening. These cells were then seeded on a DMA slide coated with anti-adherence solution to assess whether decitabine pretreatment affected spheroid formation. After a 48-hour incubation, imaging (Figure 21) showed that pretreatment did not interfere with spheroid formation, confirming the feasibility of using decitabine-pretreated spheroids for drug screening.

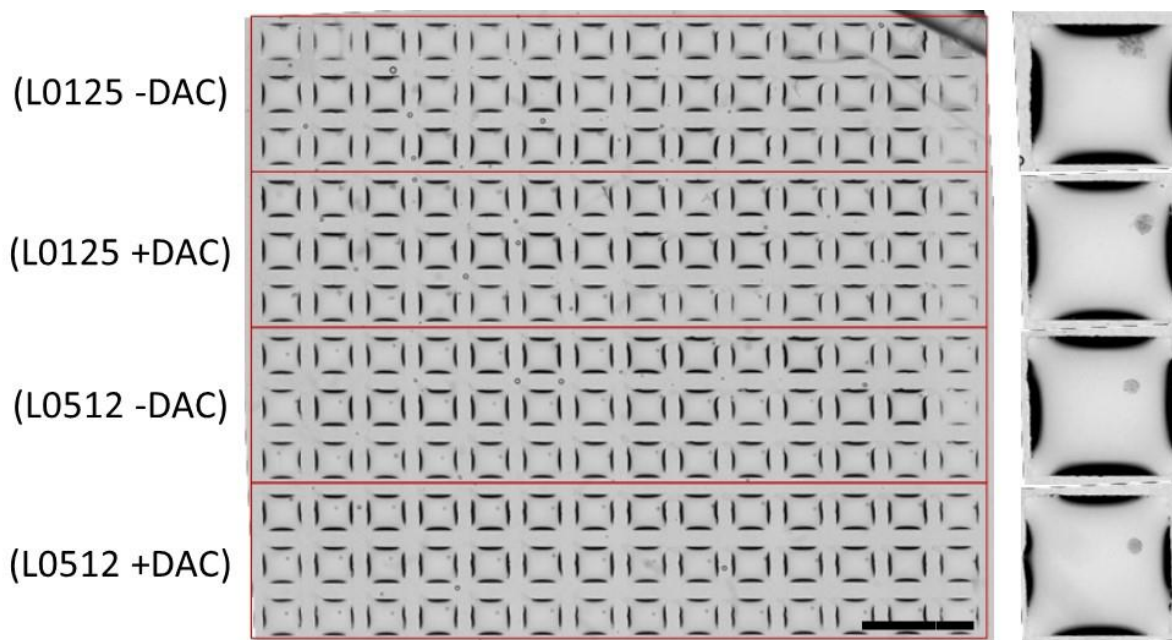


Figure 21. Spheroid formation in L0125 and L0512 cells following decitabine pretreatment. The left panel shows four blocks of a 3×14 array on the DMA slide, containing cell spheroids generated from L0125 cells (untreated and decitabine-treated) and L0512 cells (untreated and decitabine-treated), imaged in brightfield. Scale bar: 3 mm. The right panel displays a close-up of one representative spot from each block, with each spot measuring 1×1 mm.

2.2.3. High-throughput drug screening

To conduct high-throughput drug screening on L0125 and L0512 cells, the DMA slides were first coated with an anti-adherence rinsing solution and dried under a clean bench. A library of 722 CNS-penetrant compounds with known biological activity in neurological research was prepared (listed in Appendix 1). Each drug was printed onto a DMA slide at a concentration of $5 \mu\text{M}$ with five replicates per compound. A non-contact dispensing system (Scienion) was then used to print 2 nL of each drug solution onto individual spots on the DMA slide. DMSO (2 nL) was also printed as a control. This approach, which allows for high-throughput screening on 3D cell spheroids, has previously been validated by *Cui H. et al.* in IDH1-mutant glioma PDTs.⁽¹⁴²⁾ Once printed, the slides were dried in the dark at room temperature for 24 hours to ensure DMSO evaporation, then stored in dark with silica gel to maintain dryness until use.

Results and discussion

To prepare the cells, 3×10^5 cells of each line (L0125 and L0512) were seeded into two wells of a 6-well plate and incubated for 24 hours. Following this incubation, cells were harvested from each well: one sample was centrifuged and resuspended in standard culture medium, and the other was resuspended in medium containing 250 nM decitabine. Both groups of cells were cultured in two separate wells of a 6-well plate for an additional 24 hours. After decitabine treatment, cells were collected, and the concentration was adjusted to 300 cells per 200 nL for seeding onto the pre-printed drug libraries. Cells were then exposed to the drugs for 72 hours.

After drug exposure, the slides were first imaged in brightfield. A dual-readout method was used, combining both colorimetric and fluorescent assays. For the colorimetric assay, cells were stained with Kit-8 and incubated for 2 hours in a humidity chamber to allow for the formation of formazan, a colorimetric indicator of viable cells. The Kit-8 assay is designed to measure cell viability and proliferation. When added to live cells, the reagent is reduced by mitochondrial dehydrogenases to produce formazan, a yellow-orange colored compound. This reduction process occurs only in viable cells with active metabolism. The greater the number of viable cells, the higher the intensity of the color, which serves as an indicator of cell viability. After staining, the entire slide was scanned with a standard document scanner to capture the color intensity, which correlates with cell viability. For the fluorescent readout, cells were stained with a solution containing Hoechst, Calcein-AM, and PI, incubated for 30 minutes, and then imaged using an automated screening fluorescence microscope.

Currently, a method for analyzing the Kit-8 staining using Grid Screener is being developed in collaboration with Prof. Markus Reischl, Institute for Automation and Applied Informatics (IAI). This approach aims to quantify the color intensities and assign precise values for each spot.

So far, screening for 533 drugs on L0125 and 356 drugs on L0512 cell lines, under both decitabine-pretreated and untreated conditions, have been completed. Screening of the remaining drugs is ongoing. By comparing the Kit-8 colorimetric changes in drug-treated spots to the DMSO control, several drug candidates were identified as potential hits that show efficacy in the DAC-treated L0125 cells. These hits were further evaluated by overlaying the Calcein (live cells) and PI (dead cells) fluorescent channels. Effective drugs were expected to show an increase in PI signal intensity, indicating cell death. However, this fluorescent signal for the potential hits has not yet

Results and discussion

been quantified. The increased PI signal observed in all drug-treated spots aligns with the results from the Kit-8 assay, confirming these seven drugs as hits. The effects of these drug candidates were also evaluated on DAC-untreated cells, using both Kit-8 staining and fluorescent imaging. Table 3 lists the names of the identified drugs.

Number	Name of drug
1	Vorinostat
2	Obatoclax Mesylate
3	Trametinib
4	Givinostat
5	Flavopiridol HCl
6	GNE-317
7	Epoxomicin

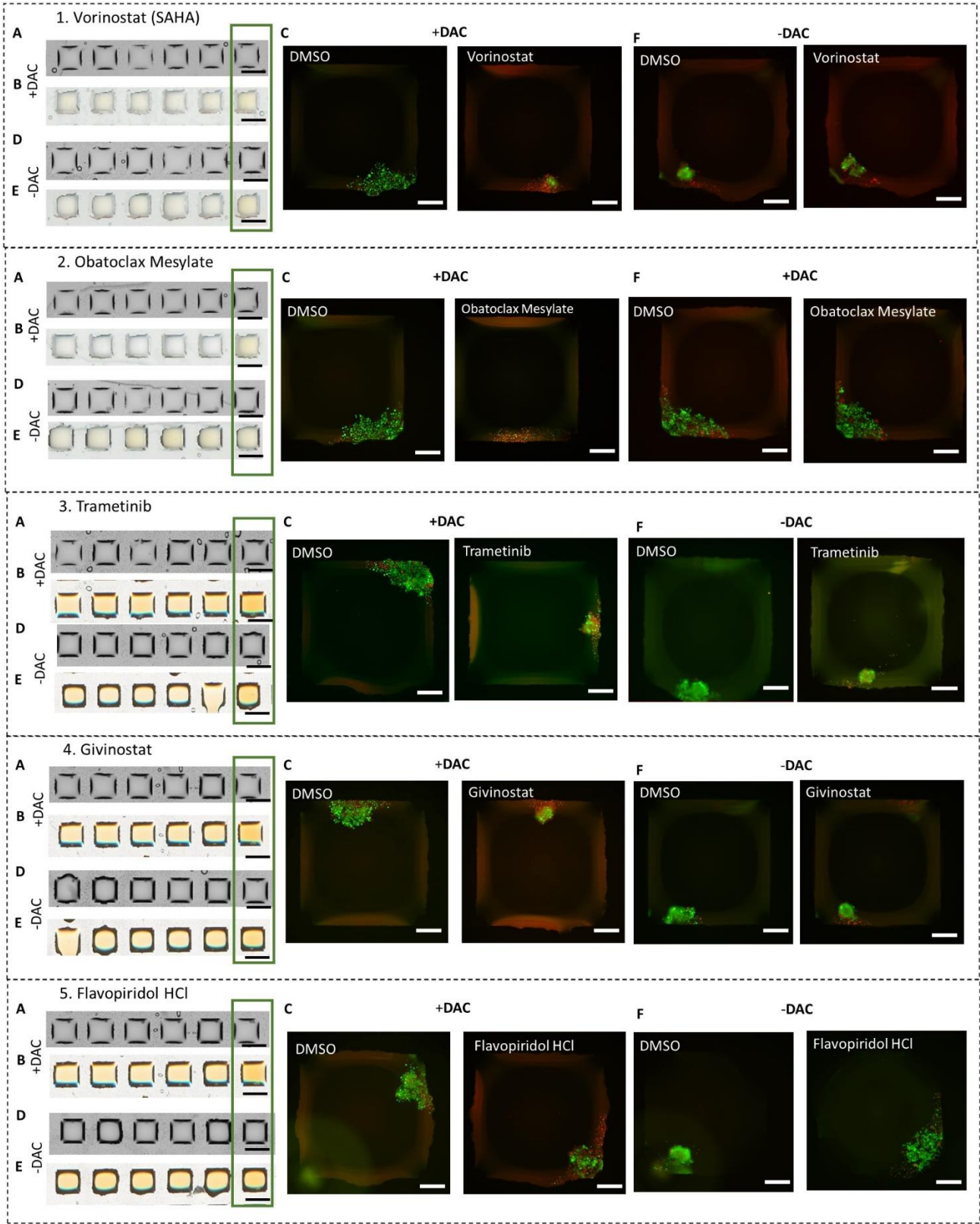
Table 3. Identified Hits from high-throughput screening of L0125 Cells. The table presents the names of seven drugs identified as potential hits during high-throughput screening. These hits were determined by analyzing the color change in Kit-8 staining images relative to the DMSO control and by observing an increase in the PI signal in fluorescent images. The observed color change and PI signal increase were consistent across all five replicates of the drug-treated spots

Figure 22 shows all hits in the DAC-pretreated condition, with their corresponding brightfield images after 72 hours of drug incubation, prior to performing the readouts (A), the image obtained from the scanner for the Kit-8 staining (B), and one representative drug-treated spot compared to its DMSO control (C). The green box in the brightfield and Kit-8 images (A and B) highlight the DMSO control spot, which appears yellow in the Kit-8 figures due to the higher number of viable cells in comparison to the pale drug-treated spots. Panel C shows an overlay of Calcein (green) and PI (red) staining, where Calcein-positive cells represent live cells, and PI-positive cells indicate dead cells. The image on the left panel shows the DMSO control, and the right panel shows one spot treated with drugs. To compare the effect of DAC-pretreatment on the efficacy of the drugs,

Results and discussion

the brightfield images after 72 hours of drug incubation, prior to performing the readouts (D), the image obtained from the scanner for the Kit-8 staining (E), and one representative drug-treated spot compared to its DMSO control (F) of the DAC-untreated cells exposed to the same drugs were presented.

Results and discussion



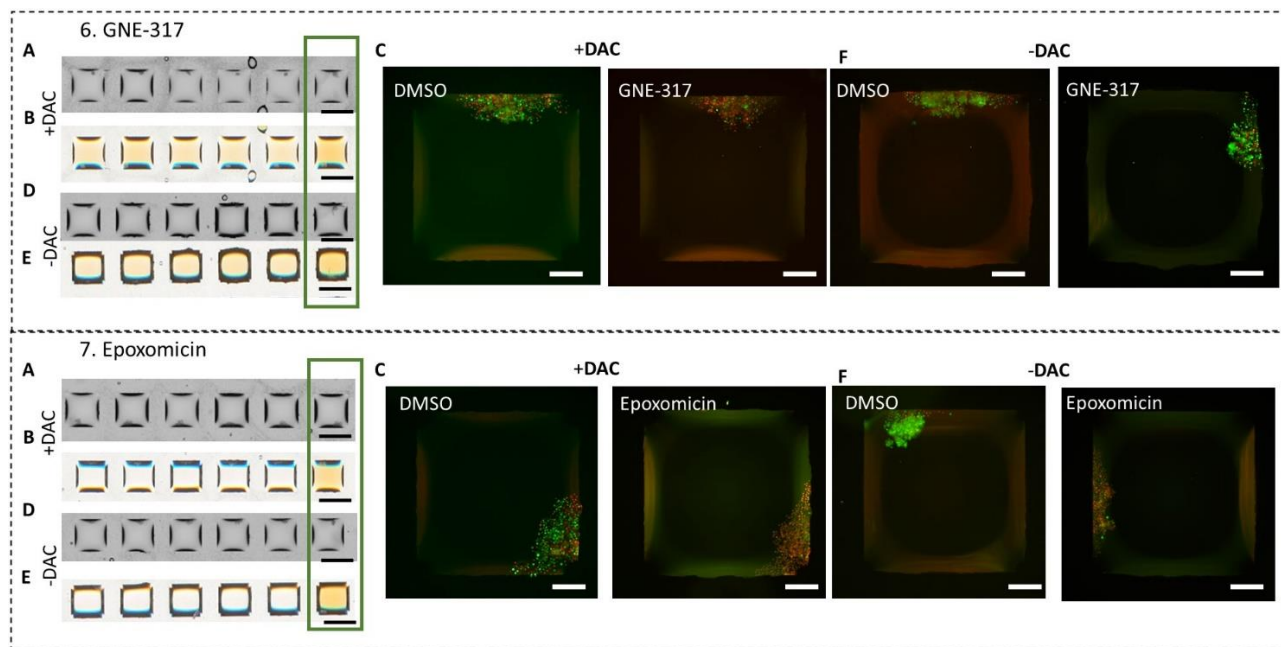


Figure 22. Drug hits for L0125 cell line using dual read-out. A) Brightfield image of drug-treated spots in DAC-pretreated cells after 72 hours of incubation. The image has been rotated 180° to align the DMSO control spot with the corresponding Kit-8 image. B) Image from the Kit-8 staining scan, showing cell viability in drug-treated spots for DAC-pretreated cells. The green box in both the brightfield (A) and Kit-8 images (B) highlight the DMSO control spot, which appears yellow due to the presence of more viable cells compared to the pale drug-treated spots. Scale bar: 1 mm. C) Overlay of Calcein (green) and PI (red) staining, showing the DMSO control on the left and one drug-treated spot on the right in DAC-pretreated cells. Calcein-positive cells indicate live cells, while PI-positive cells represent dead cells. The fluorescent signal for PI in drug-treated spots is expected to increase if the drug is effective in inducing cell death. Scale bar: 200 μ m. D) Brightfield image of drug-treated spots in DAC-untreated cells after 72 hours of incubation. The image has been rotated 180° to align the DMSO control spot with the corresponding Kit-8 image. E) Image from the Kit-8 staining scan, showing cell viability in drug-treated spots for DAC-untreated cells. The green box in both the brightfield (D) and Kit-8 images (E) highlight the DMSO control spot, which appears yellow due to the presence of more viable cells compared to the pale drug-treated spots. Scale bar: 1 mm. F) Overlay of Calcein (green) and PI (red) staining, showing the DMSO control on the left and one drug-treated spot on the right in DAC-untreated cells. Calcein-positive cells indicate live cells, while PI-positive cells represent dead cells. Scale bar: 200 μ m.

Obatoclax Mesylated, Trametinib, Givinostat, Flavopiridol HCl and GNE-317 did not show significant effects in the DAC-untreated condition. However, when DAC-pretreated cells were exposed to the same panel of drugs, the Kit-8-stained spots became pale compared to the control, and the PI signal increased. This suggests that DAC pretreatment sensitizes the cells, enhancing the efficacy of these CNS-penetrating drugs and highlighting their greater therapeutic potential when combined with DAC.

The Bcl-2 inhibitor Obatoclax has shown promise in targeting patient-derived glioblastoma stem-like cells.⁽¹⁴³⁾ Trametinib is a MEK1/MEK2 inhibitor that has been evaluated in clinical trials for various cancers, including gliomas. In 2023, the FDA approved the combination of dabrafenib and trametinib for pediatric patients with low-grade glioma harboring a BRAF V600E mutation.⁽¹⁴⁴⁾ Givinostat, a histone deacetylase inhibitor, has demonstrated anti-tumor effects on both 2D and 3D glioblastoma models.⁽¹⁴⁵⁾ Flavopiridol is a potent cyclin-dependent kinase (CDK) inhibitor that works by disrupting the cell cycle, thereby preventing cell division and promoting apoptosis. It has been evaluated in various cancers, including gliomas, and has shown activity against glioma cell lines in vitro.⁽¹⁴⁶⁾ GNE-317 is a brain-penetrant Phosphatidylinositol 3-kinase (PI3K) inhibitor. PI3K pathway deregulation has been implicated in glioblastoma,^(147, 148) and GNE-317 has demonstrated inhibition of this pathway in mouse models, achieving tumor growth inhibition of 90% and 50%, along with survival benefits.⁽¹⁴⁹⁾

This study suggests that DAC pretreatment can increase the efficacy of these drugs in treatment of GBM cells by sensitizes the cells.

Vorinostat and Epoxomicin demonstrated effects on L0125 cells in both DAC-pretreated and untreated conditions. Kit-8-stained spots became pale compared to the control, and the PI signal intensity increased in both cases. This suggests that DAC pretreatment does not inhibit the activity of these drugs on this cell line. Quantification of Kit-8 staining and PI signal intensities will help clarify whether DAC enhances the efficacy of these drugs.

Vorinostat, another histone deacetylase inhibitor, has been studied for its effects on recurrent glioblastomas but⁽¹⁵⁰⁾ Epoxomicin has not been specifically reported to target glioblastoma. This study indicates its potential as a treatment for glioblastoma, either as a single agent or in combination with DAC.

Results and discussion

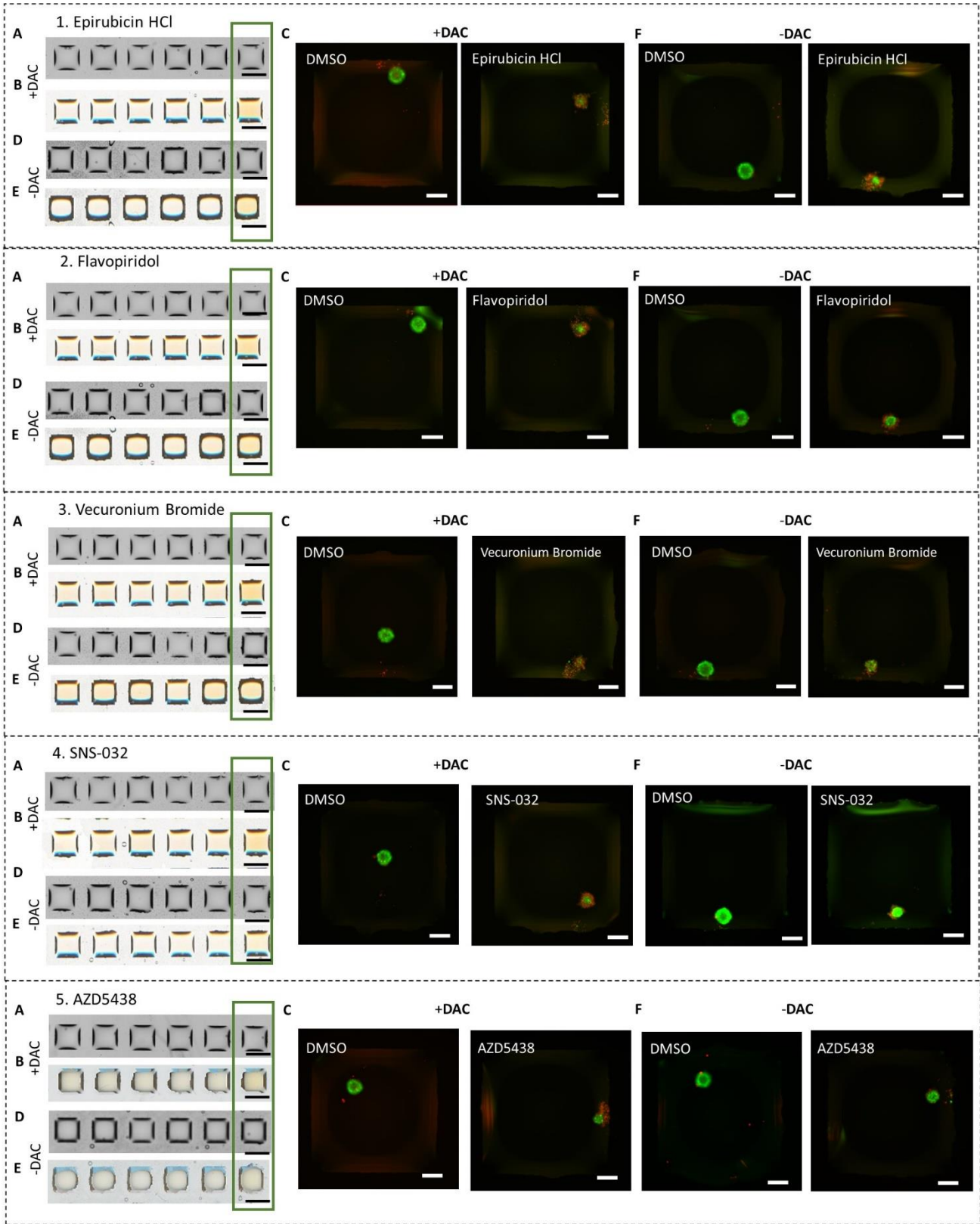
To identify drug hits in the other cell line, L0512, Kit-8 colorimetric changes in drug-treated spots were compared to the DMSO control. Several drug candidates were identified as potential hits that show efficacy in the DAC-treated L512 cells. These hits were further evaluated by overlaying the Calcein (live cells) and PI (dead cells) fluorescent channels. Effective drugs were expected to show an increase in PI signal intensity, indicating cell death. However, this fluorescent signal for the potential hits has not yet been quantified. The increased PI signal observed in all drug-treated spots aligns with the results from the Kit-8 assay, confirming these six drugs as hits. The effects of these drug candidates were also evaluated on DAC-untreated cells, using both Kit-8 staining and fluorescent imaging. Table 4 lists the names of the identified drugs.

Number	Name of drug
1	Epirubicin HCl
2	Flavopiridol
3	Vecuronium bromide
4	SNS-032
5	AZD5438
6	Givinostat

Table 4. Identified Hits from high-throughput screening of L0512 Cells. The table presents the names of six drugs identified as potential hits during high-throughput screening. These hits were determined by analyzing the color change in Kit-8 staining images relative to the DMSO control and by observing an increase in the PI signal in fluorescent images. The observed color change and PI signal increase were consistent across all five replicates of the drug-treated spots

Figure 23 shows all hits in the DAC-pretreated condition, with their corresponding brightfield images after 72 hours of drug incubation, prior to performing the readouts (A), the image obtained from the scanner for the Kit-8 staining (B), and one representative drug-treated spot compared to its DMSO control (C). The green box in the brightfield and Kit-8 images (A and B) highlight the DMSO control spot, which appears yellow in the Kit-8 figures due to the higher number of viable cells in comparison to the pale drug-treated spots. Panel C shows an overlay of Calcein (green) and PI (red) staining, where Calcein-positive cells represent live cells, and PI-positive cells indicate dead cells. The image on the left panel shows the DMSO control, and the right panel shows one spot treated with drugs. To compare the effect of DAC-pretreatment on the efficacy of the drugs, the brightfield images after 72 hours of drug incubation, prior to performing the readouts (D), the image obtained from the scanner for the Kit-8 staining (E), and one representative drug-treated spot compared to its DMSO control (F) of the DAC-untreated cells exposed to the same drugs were presented.

Results and discussion



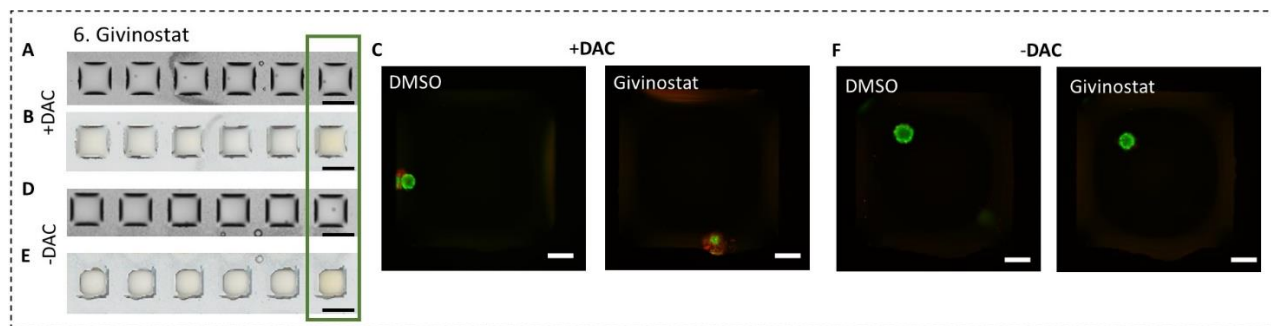


Figure 23. Drug hits for L0512 cell line using dual read-out. A) Brightfield image of drug-treated spots in DAC-pretreated cells after 72 hours of incubation. The image has been rotated 180° to align the DMSO control spot with the corresponding Kit-8 image. B) Image from the Kit-8 staining scan, showing cell viability in drug-treated spots for DAC-pretreated cells. The green box in both the brightfield (A) and Kit-8 images (B) highlight the DMSO control spot, which appears yellow due to the presence of more viable cells compared to the pale drug-treated spots. Scale bar: 1 mm. C) Overlay of Calcein (green) and PI (red) staining, showing the DMSO control on the left and one drug-treated spot on the right in DAC-pretreated cells. Calcein-positive cells indicate live cells, while PI-positive cells represent dead cells. The fluorescent signal for PI in drug-treated spots is expected to increase if the drug is effective in inducing cell death. Scale bar: 200 μm . D) Brightfield image of drug-treated spots in DAC-untreated cells after 72 hours of incubation. The image has been rotated 180° to align the DMSO control spot with the corresponding Kit-8 image. E) Image from the Kit-8 staining scan, showing cell viability in drug-treated spots for DAC-untreated cells. The green box in both the brightfield (D) and Kit-8 images (E) highlight the DMSO control spot, which appears yellow due to the presence of more viable cells compared to the pale drug-treated spots. Scale bar: 1 mm. F) Overlay of Calcein (green) and PI (red) staining, showing the DMSO control on the left and one drug-treated spot on the right in DAC-untreated cells. Calcein-positive cells indicate live cells, while PI-positive cells represent dead cells. Scale bar: 200 μm .

Flavopiridol and Givinostat were also identified as hits for L0125, showing increased efficacy when DAC-pretreated cells were exposed to them in both cell lines.

Epirubicin is an anthracycline chemotherapy drug commonly used to treat various cancers, including breast cancer. It works by intercalating into DNA, inhibiting DNA synthesis, and inducing apoptosis. Epirubicin HCl has been investigated in glioma and glioblastoma models.⁽¹⁵¹⁾

Vecuronium bromide is a non-depolarizing neuromuscular blocker used primarily for muscle relaxation during surgery and anesthesia. The effect of this drug in lung cancer cells A549 proliferation, migration and viability in the presence of a cytotoxic drug, cisplatin has been investigated⁽¹⁵²⁾ but there is no study on the effect of this drug in Glioma. SNS-032 is a selective CDK2/7/9 inhibitor, which, like Flavopiridol, disrupts the cell cycle and induces cell death. It has shown efficacy in various cancer types, including gliomas.⁽¹⁵³⁾ AZD5438 is a CDK inhibitor and has been studied in various cancers, including gliomas, due to its ability to disrupt cancer cell proliferation.⁽¹⁵⁴⁾

Epirubicin demonstrated effects on L0512 cells in both DAC-pretreated and untreated conditions. Kit-8-stained spots became pale compared to the control, and the PI signal intensity increased in both cases. This suggests that DAC pretreatment does not inhibit the activity of this drug on this cell line. Quantification of Kit-8 staining and PI signal intensities will help clarify whether DAC enhances the efficacy of these drugs.

In this study, a combination therapy approach at the nanoliter scale was used, where cells were pretreated with DAC and cultured as miniaturized cell spheroids. DAC pretreatment is hypothesized to sensitize the cells, making them more susceptible to the cytotoxic effects of the tested drugs therefore, improving their therapeutic potential. Currently, methods for quantifying the results from Kit-8 and fluorescent staining are in progress, which will help determine whether DAC enhances the efficacy of these drugs.

Drug testing on the remaining compounds in the library is ongoing, with the goal of identifying additional therapeutic options for glioblastoma patients. To validate the results obtained so far (listed in Tables 3 and 4) and to generate dose-response curves, eleven concentrations of each drug will be prepared. The cell lines will then be tested with these concentrations in both DAC-pretreated and untreated conditions using 384-well plates.

2.2.4. Summary

Gliomas, particularly GBM, are a heterogeneous and highly aggressive group of primary brain tumors. While standard treatments, including surgery, radiation, and chemotherapy with agents like temozolomide, are commonly used, they often fail. One major factor contributing to this resistance is epigenetic dysregulation, highlighting the urgent need for alternative therapeutic strategies. This study aims to introduce a novel approach that targets these epigenetic mechanisms to improve treatment outcomes.

The aim of this study is to find new therapeutic options for GBM by pre-treating glioblastoma cells with decitabine (DAC), a DNA methyltransferase inhibitor, and screening for synergistic drug combinations using high-throughput drug testing. This approach aims to enhance the efficacy of blood-brain barrier-penetrating drugs in DAC-pretreated glioma cells. The study uses the DMA platform for high-throughput screening of 722 drugs, where assay miniaturization reduces reagent consumption and increases throughput. Additionally, the glioblastoma tumor sphere cell lines used in this study, L0125 and L0512, are slow-growing, and the DMA platform helps minimize the number of cells required for testing. This approach is designed to identify potential therapies that could overcome the epigenetic resistance mechanisms present in glioblastoma.

In this study, GBM cells were pre-treated with DAC to sensitize them to a library of 722 CNS-penetrating drugs. The DMA platform was used for high-throughput drug screening by culturing only 300 cells per spots with the volume of 200 nanoliter. The drug effects were assessed in DAC-pretreated and untreated conditions, and the efficacy of the treatments was compared to identify drugs that showed enhanced activity in DAC-sensitized cells. The results were validated by using fluorescent staining techniques and comparing them with the Kit-8 cell viability assay.

The drug screening identified several potential hits. Among the identified drugs, Obatoclax Mesylate, Trametinib, Givinostat, Flavopiridol HCl, GNE-317, Epirubicin HCl, Vecuronium bromide, SNS-032 and AZD5438 showed enhanced toxicity in the DAC-pretreated cells compared to untreated cells, suggesting DAC's ability to sensitize the cells to these drugs. These findings demonstrate that DAC pretreatment can enhance the therapeutic potential of several CNS-penetrating drugs by overcoming the epigenetic resistance present in glioblastoma.

This study successfully introduced a novel combination therapy strategy on DMA slide by using DAC pretreatment to sensitize glioma cells to a broad panel of drugs. The use of the DMA platform enabled high-throughput screening and the identification of promising drug combinations that can be further explored in future clinical studies. The results support the concept that DAC can enhance the efficacy of existing CNS-penetrating drugs, making them more effective in treating glioblastoma. This approach represents a promising direction in glioma therapy, particularly for tumors that exhibit resistance to conventional treatments. Additionally, the DMA platform holds potential for rapid, scalable testing of other therapeutic agents, offering a powerful tool for future high-throughput drug screening in gliomas and other types of cancer.

2.3. Nanoliter Hydrogel Array for High Throughput 3D Cell Screening, Spheroid Sorting and Patterning

Disclaimer: This chapter, associated sections and images are published in [§1] and have been adopted for this thesis.

[§1] Salarian M, Levkin P, Popova A. Nanoliter Hydrogel Array for Cell Screening and Cell Spheroid Sorting. Advanced Materials Technologies. Dec 2024. DOI: 10.1002/admt.202401159

Some of the content has been rewritten for a better understanding of this thesis work.

2.3.1. Project idea and background

Cells in tissues and organs naturally exist within a 3D microenvironment, interacting dynamically with the ECM and neighboring cells.⁽¹⁵⁵⁾ As a result, there has been a shift from traditional 2D cell culture models to more advanced 3D models to better replicate in vivo conditions.^(156, 157) It was also mentioned that 3D cell culture models are divided into two main categories: scaffold-based methods and scaffold-free approaches.⁽¹⁵⁸⁾ Scaffold-based methods often involve using 3D matrices, such as hydrogels, to incorporate and support cells.

Hydrogels are continuously evolving and have become the preferred choice for creating innovative 3D systems in areas like tissue engineering, organoid culture, and bioprinting. Furthermore,

hydrogels have played an important role in overcoming the challenges of integrating 3D cultures into high-throughput screening workflows, serving as supportive scaffolds for cells. In this project, hydrogels have been combined as scaffolds for culturing cells with nanoliter array format on the DMA platform.

Hydrogels are hydrophilic material composed of three-dimensional networks of crosslinked natural or synthetic polymers. These networks allow hydrogels to absorb significant amounts of water and expand while maintaining their structural stability.⁽¹⁵⁹⁾ They are often used as analogs of ECM and sometimes are functionalized with ECM components to further mimic the native environment.^(160, 161) The crosslinked structure of hydrogels resembles the fibrillar architecture found in biological tissues, providing mechanical support similar to the natural ECM.⁽¹⁶²⁾ This support is essential for cell adhesion, growth and the overall maintenance of cellular functions.⁽¹⁶³⁾ As a result, hydrogels closely replicate the functionality of the native ECM by surrounding and instructing cells. Because of their structural and functional properties, hydrogels find applications in areas such as drug delivery,⁽¹⁶⁴⁾ wound healing,⁽¹⁶⁵⁾ tissue engineering,^(166, 167) disease modeling including cancer⁽¹⁶⁸⁾ and high-throughput drug screening.⁽¹⁶⁹⁾ In addition to supporting cell structures, 3D hydrogel matrices can compartmentalize cells, making them useful for studying interactions between cancer cells and other cell types, including immune cells⁽¹⁷⁰⁾ and stromal fibroblasts.⁽¹⁷¹⁾ For example, *Huang et al.* integrated hydrogels with encapsulated cells into microfluidic device for precise control of cell culture microenvironment.⁽¹⁷²⁾ *Ding et.al* added cells from primary tissues to Matrigel to generate high-throughput microfluidic-based droplet Micro-Organospheres with the goal to facilitate drug screening and precision oncology treatment.⁽¹¹²⁾

However, integrating 3D cultures into HTS workflows presents several challenges, particularly the need for hydrogels to be compatible with automated liquid handling systems.⁽¹⁶⁹⁾ This difficulty arises due to the high viscosity of hydrogel matrices like collagen or Matrigel, which can complicate precise dispensing. In addition, the polymerization of such gels is highly sensitive to environmental conditions, including temperature, therefore, requiring precise environmental control during printing. The miniaturization of HTS workflows combined with hydrogel-like matrices is even more challenging due to the small volumes.⁽¹⁷³⁾

DMA platform offers a solution for conducting miniaturized and high-throughput cell-based assays. Culturing cells in liquid media on DMA slides is a well-established approach, but this project focuses on introducing hydrogel-based cultures to the DMA system for HTS workflows for the first time. The aim is to develop a stable array of nanoliter-volume hydrogels capable of supporting cells or cell spheroids. These hydrogels should be efficiently and precisely dispensed onto a DMA chip in an automated, high-throughput manner while maintaining stability on the chip surface. Each hydrogel array should be capable of being cultured in its own medium droplet, allowing compartmentalization for screening multiple conditions. Additionally, the potential for incorporating cell spheroids into the hydrogel pads will be explored. This could enable various protocols, such as long-term culture, spheroid sorting, and automated high-throughput imaging of hydrogel arrays, without risking the loss of non-adherent cells or structures like spheroids or organoids.

2.3.2. Protocol optimization

A DMA chip, featuring 672 square hydrophilic spots arranged in a 14×48 grid with each spot measuring $1 \text{ mm} \times 1 \text{ mm}$, and a Dextran-PEG hydrogel system, was utilized throughout the project. This specific hydrogel was selected for its slow gelling properties, which improve printability and compatibility with automated liquid handling systems. Two methods were explored to incorporate cells into nanoliter hydrogel pads on the DMA (Figure. 24A and B). In the first method, cells at the desired density were pre-mixed with hydrogel precursors, and 150 nL of this mixture was dispensed onto DMA spots using the non-contact liquid dispenser IDOT-One (Figure. 24A). In the second

method, a droplet of liquid media containing either cell suspension or spheroids was gelated at a chosen time point by adding hydrogel precursors directly to the droplet on the DMA (Figure. 21B).

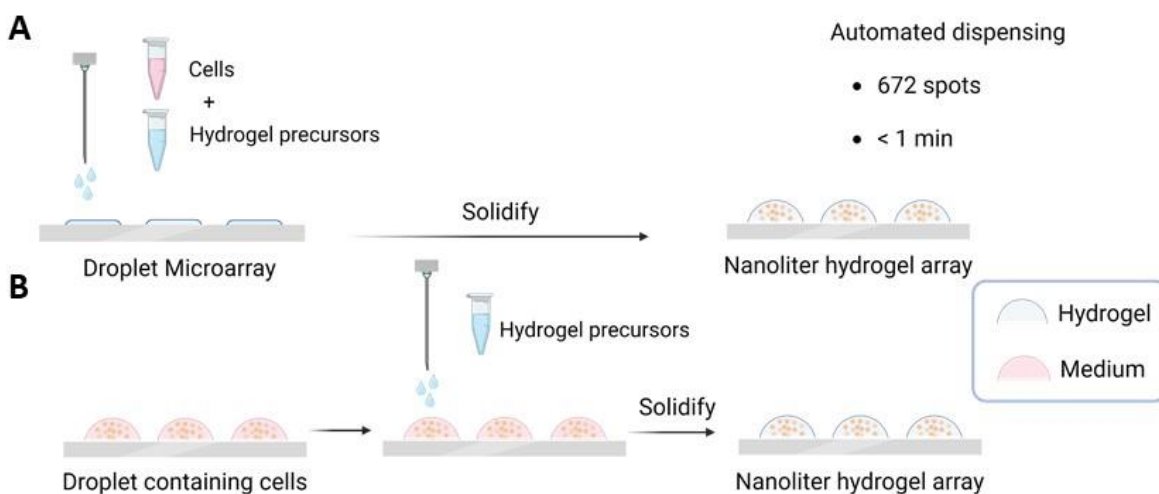


Figure 24. Nanoliter hydrogel array on the DMA platform. A) Hydrogel precursors can be mixed with a cell suspension and dispensed onto the 672 spots DMA slide using a liquid dispenser in less than 1 minute. B) Hydrogel precursors can be dispensed onto cell-containing droplets on the DMA at any point during their culture, leading to the gelation of the droplets.

Both approaches have been optimized and demonstrated fabrication of 672 hydrogel pads on a single slide in less than 1 minute (Figure 25), achieving precise control over hydrogel volumes and number of cells per gel (Figure 25).

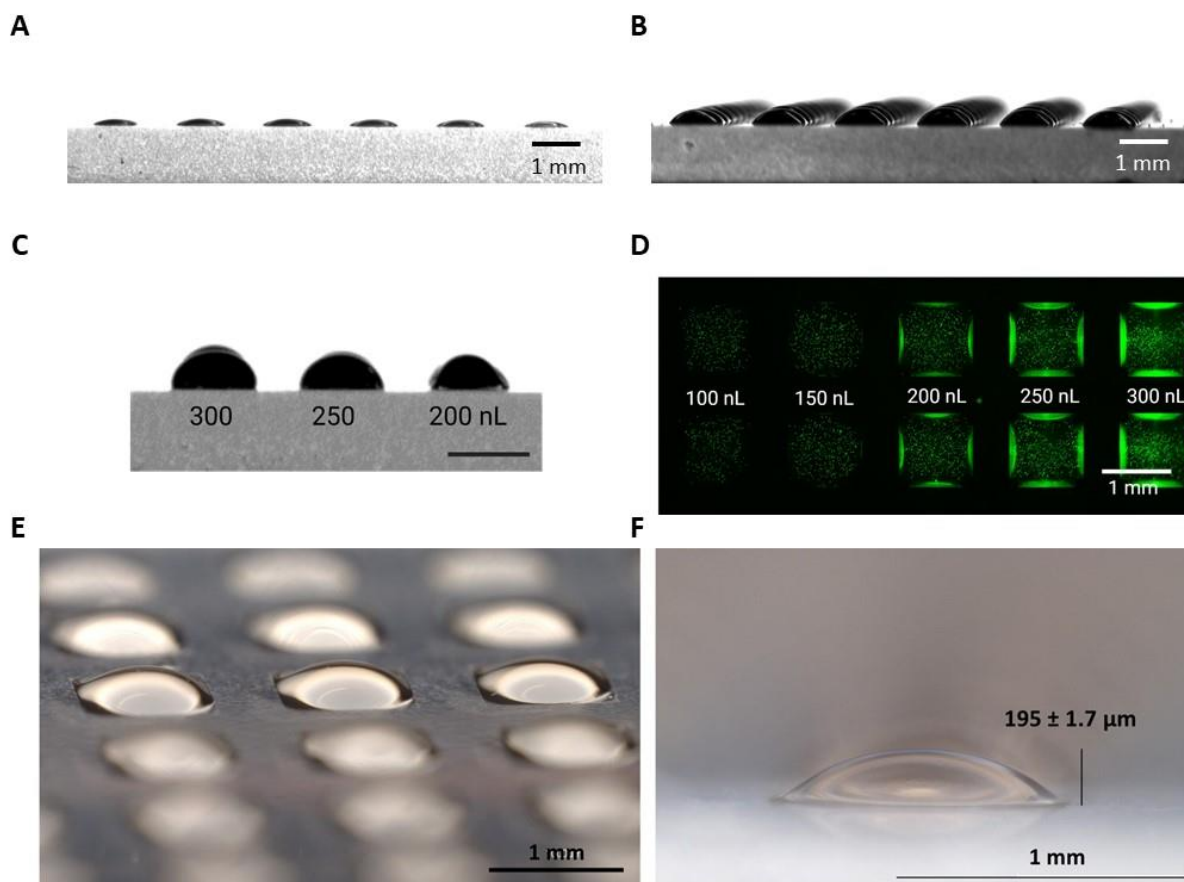


Figure 25. Homogeneity of hydrogels. A) A side view of the hydrogels formed on the DMA slide. B) A side view of the hydrogels with medium dispensed on them. Scale bar: 1mm. C) Side and (D) top view of hydrogel droplets of different volumes ranging from 100 to 300 nL formed on the DMA chip. Scale bar: 1mm. D) Microscope image of Jurkat human T lymphocyte cells stained with Calcein incorporated in hydrogel pads. E) Microscope image of an array of hydrogel pads on a DMA slide, each with a volume of 150 nanoliters; scale bar: 1 mm. F) Photo of a single hydrogel pad with a vertical dimension of $195 \pm 1.7 \mu\text{m}$ (standard deviation of 1.77); scale bar: 1 mm (right panel).

After optimizing the nanoliter hydrogel array dispensing process, this study expanded on previous work that exclusively cultured and screened cells in liquid media on the DMA platform, as detailed in earlier publications.^(174, 175) In this study, cell culture within hydrogel was further investigated and compared to conventional cell culture in liquid media on a DMA chip. Jurkat human T

Results and discussion

lymphocyte cells were pre-mixed with hydrogel precursors, Dextran and PEG-link, and 150 nL of this cell-containing mixture, averaging 300 cells per hydrophilic spot, was dispensed onto each spot of the DMA slide. Following a 45-minute solidification, 150 nL of culture medium was added to each hydrogel pad (Figure. 26).

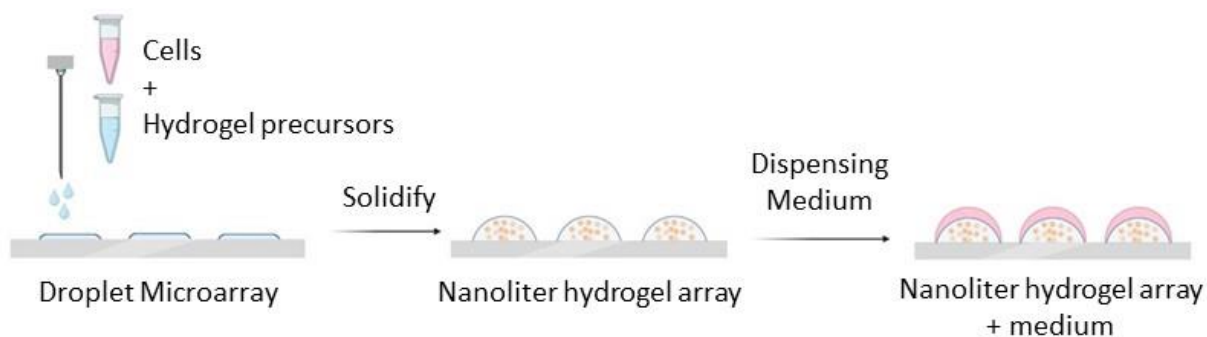


Figure 26. Cell culture in nanoliter hydrogel array. Schematic representation of the workflow for creating nanoliter hydrogel array containing cells. A suspension of cells was pre-mixed with hydrogel precursors and the mixture was dispensed onto DMA spots in a volume of 150 nL. After the hydrogel solidified for 45 minutes in a cell culture incubator, 150 nL of culturing medium was dispensed on top of each hydrogel pad.

As the next step, the viability of cells cultured in hydrogels for four days without medium change was measured. Every 24 hours, 50 nL of staining solution containing Hoechst 33342, Calcein-AM, and PI was dispensed onto each hydrogel pad for staining. Cell viability was calculated by dividing the number of live cells (Calcein positive) by the total number of cells (Calcein positive + PI positive). Cells cultured in hydrogel pads demonstrated viabilities of 94.6%, 93.5%, and 91.3% at 24, 48, and 72 hours of incubation, respectively, while those in liquid medium showed viabilities of 98%, 90.7%, and 88.8% at the same time points. For both the liquid medium and hydrogel-based droplets, cells maintained high viability within the first 72 hours of culture (Figure. 27B). A decrease in cell viability was observed after a 96-hour culture period in both media, which is expected due to the lack of medium change. Jurkat cells were cultured in both hydrogel pads and

Results and discussion

liquid medium on the same chip, following the previously described method. After dispensing, the slide was placed in a humidity chamber and imaged using brightfield microscopy. Following imaging, the slide was incubated in a standard cell culture incubator. Cells were imaged every 24 hours in both the hydrogel pads and liquid medium. As shown in Figure. 27C, cells proliferated the same in both environments. These results suggest that the nanoliter hydrogel array can be used for cell culture on the DMA platform, similarly to previously demonstrated liquid droplet arrays.

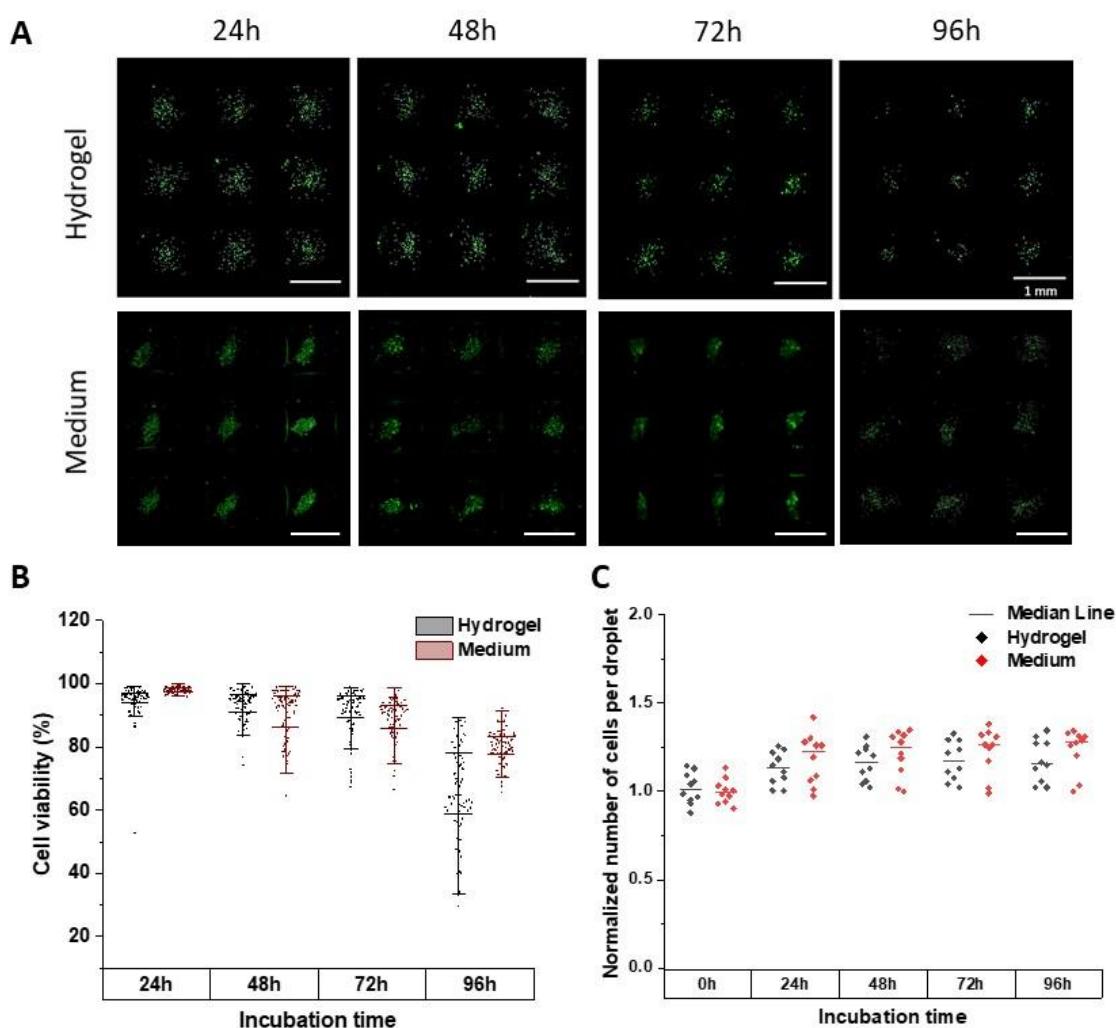


Figure 27. Comparison of cell culture in nanoliter hydrogel array and in array of liquid droplets. A) Representative fluorescence images of a 3 x 3 of nanoliter hydrogel (top panel) and liquid droplet (bottom

Results and discussion

panel) containing Jurkat cells, stained with Calcein-AM after 24, 48, 72 and 96 hours of culture. Scale bar: 1mm. B) Viability of cells cultured in hydrogels and liquid droplets for 24, 48, 72 and 96 hours. The data are presented as scattered boxplots. The box represents the interquartile range (IQR, 25th–75th percentiles), and the whiskers extend to 1.5 times the IQR. Each condition includes data from 84 replicates. C) Proliferation of cells cultured in hydrogel pads and liquid medium droplets over 96 hours. The data are normalized to the cell count at 0 hours and are presented as scattered boxplots with bar indicating the median of 12 replicates per condition.

The stability of the hydrogels on the DMA slide was evaluated by dispensing hydrogel precursors mixed with cells onto a DMA slide, following the previously described procedure (Figure. 24A). Cells were then stained with Hoechst and Calcein-AM to enable visualization. The nanoliter hydrogel array was then washed twice with PBS, and the integrity of the hydrogels on the DMA chip was assessed by comparing the positions and number of cells before and after the washing steps (Figure. 28B).

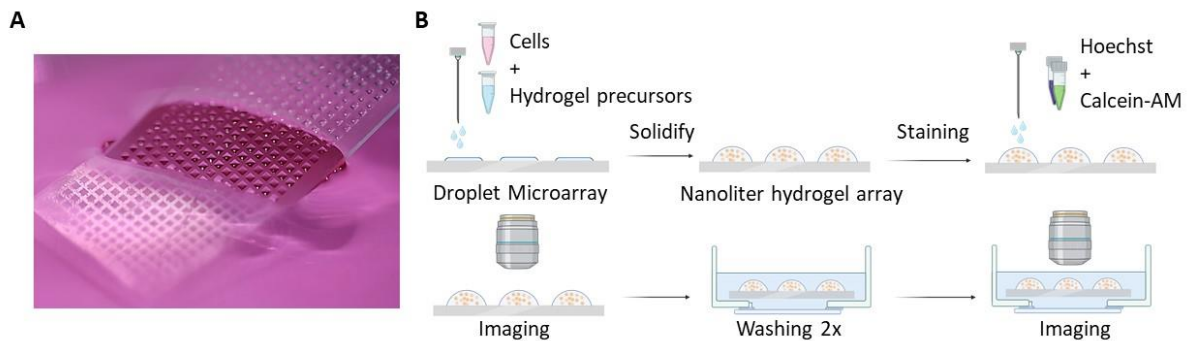


Figure 28. Validation of the stability of hydrogel pads on the DMA slide during washing procedure. A) A photograph of the nanoliter hydrogel array immersed in culture medium. B) Schematics representation of experimental workflow for validation of hydrogel intactness on the DMA slide. First, hydrogel array was dispensed on the DMA chip, after the gelation the cells in hydrogels were stained and the hydrogel array was imaged, then the whole array was immersed in PBS and washed twice, finally, the array was imaged again to compare number and position of cells before and after the procedure.

Figure 29A and B demonstrate an array of hydrogels and a close-up of a single hydrogel before and after immersion in PBS, respectively. As shown in Figure 29C, the cell count within the same hydrogels remained unchanged following the washing step. Additionally, it was demonstrated that cell positions also remained stable after washing (Figure. 29D). These findings suggest that the number and position of cells were unaffected by the washing procedure, indicating that the hydrogels are stable on the hydrophilic spots of the DMA chip.

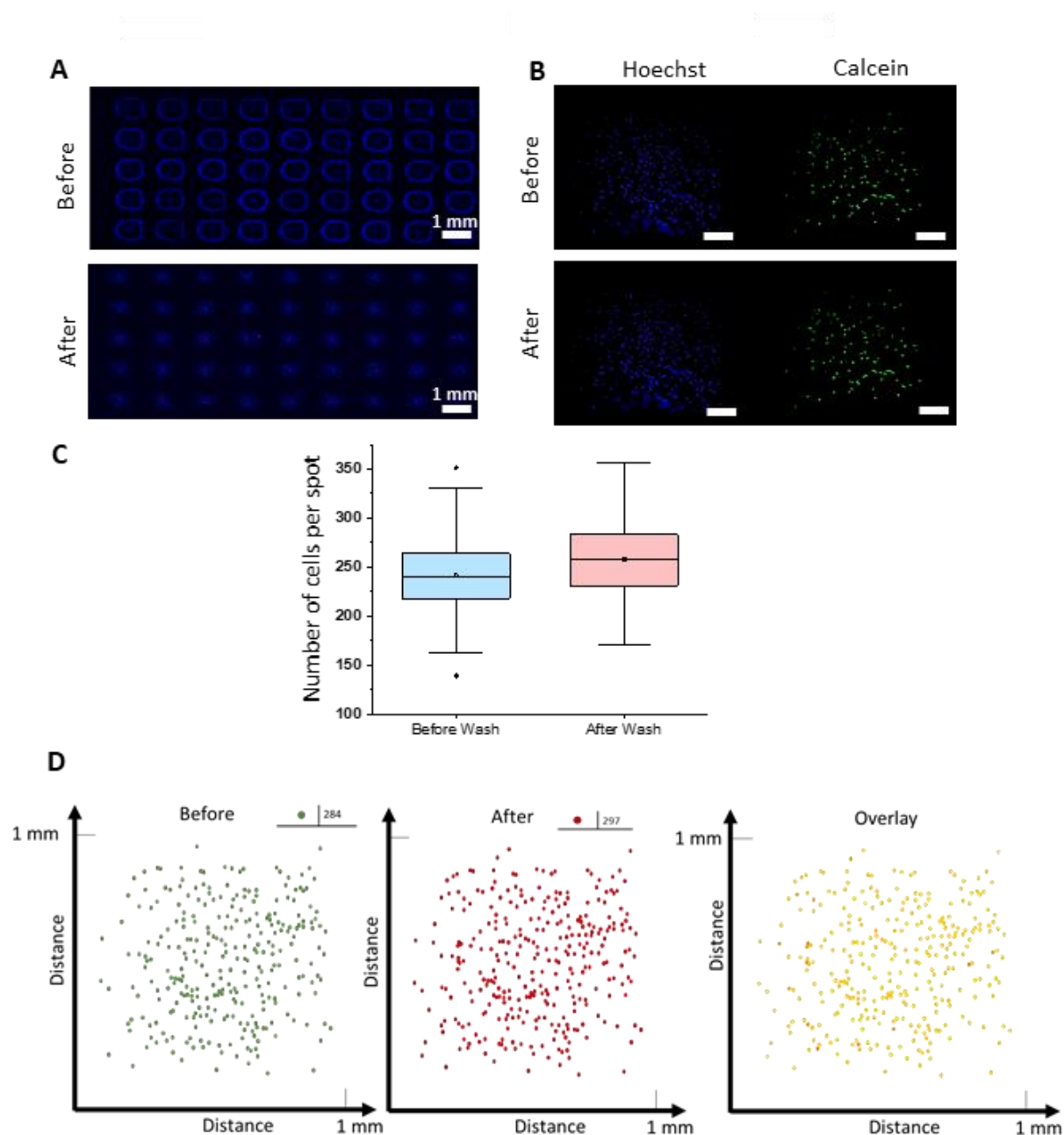


Figure 29. Stable nanoliter hydrogel array. A) Microscope images of nanoliter hydrogel array before (upper panel) and after (lower panel) the washing steps. B) Microscope image of a single hydrogel containing cells before (upper panel) and after (lower panel) the washing steps. The scale bar: 200 μm . C) Graph showing the number of cells cultured in hydrogel on the DMA slide before and after immersion in PBS from 84 spots. D) A 2D model showing the positions of each cell within a hydrogel before (in green) and after (in red) the washing procedure. The overlay image combines both sets of data, with yellow indicating regions

where the positions of cells before and after washing completely overlap. This model is based on the example of a single hydrogel.

2.3.3. Selective sorting of spheroids

In the next step, the possibility of gelation of liquid droplets on the DMA chip at any stage of an experiment was demonstrated (Figure. 24B). For this, liquid media droplets containing 3D spheroids were selected. The DMA platform's potential to create a single 3D cell spheroid per droplet using the hanging drop method has been shown in several prior studies^(142, 176-178); however, these studies exclusively used liquid medium, and this is the first application of hydrogel on the DMA slide to encapsulate cell spheroids.

Before demonstrating the possibility of droplet gelation with spheroids, first the stability of hydrogels on the DMA surface after coating hydrophilic spots with the anti-adherence solution used in the protocol for single spheroid array formation was assessed (Figure. 30A). The stability of hydrogels on the coated hydrophilic spots was successfully demonstrated by comparing the number and positions of cells before and after washing steps (Figure. 30B and 30C).

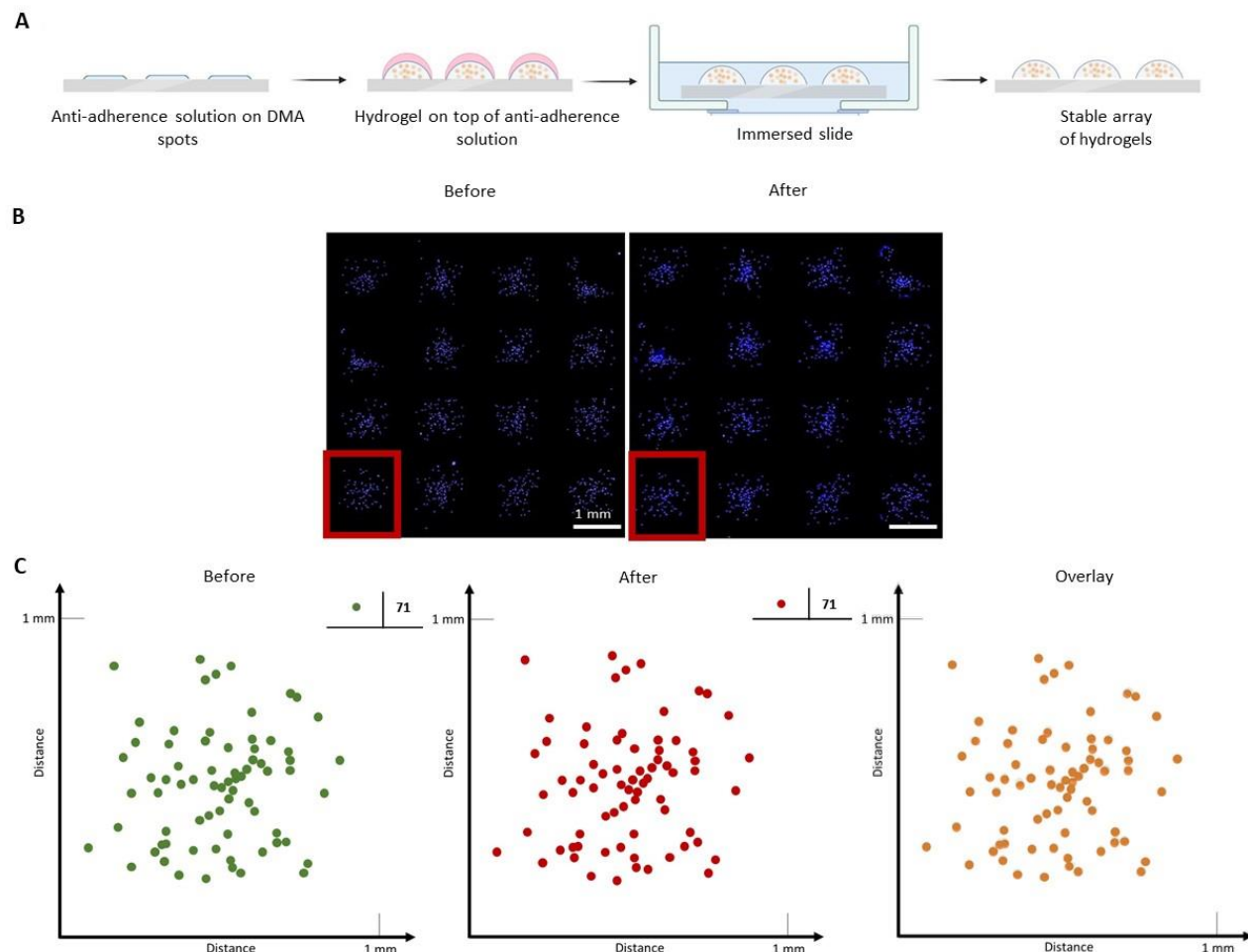


Figure 30. Stability of hydrogels on coated DMA spots. A) Schematics representation of the workflow for checking if anti-adherence coating of hydrophilic spots influences the stability of hydrogels on the surface. B) Microscope image of the array of 4 x 4 hydrogels containing cells stained with Hoechst on anti-adherence coating before and after immersion in PBS. C) The 2D model of positions of each cell in hydrogel before (in green) and after (in red) washing procedure, modeled on the example of a single hydrogel.

Next, to generate spheroids, MCF-7 cells were cultured on the DMA slide using a hanging drop method for 48 hours allowing for the formation of a single 3D spheroid per liquid media droplet. After 48 hours of incubation, hydrogel precursors were dispensed into each liquid droplet on the DMA chip keeping the ratio necessary for the gelation (Figure. 31).

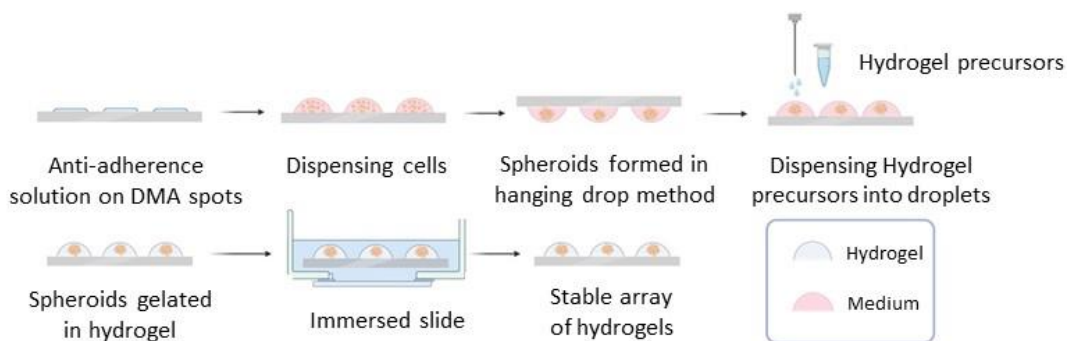


Figure 31. Gelation of single spheroid array on the DMA slide. Schematic representation of the workflow for the generation and subsequent gelation of single spheroid array. MCF-7 cells were dispensed into hydrophilic spot coated with anti-adherence solution and cultured for 48 hours in inverted position. Afterwards, the hydrogel precursors were dispensed into each droplet to gelate the liquid droplets.

To demonstrate the gelation of the droplets containing spheroids and showcase their stability on the slide during washing procedures, the DMA slide containing spheroids in hydrogels was imaged before and after immersion in PBS (Figure. 32B). We have shown that spheroids stayed at the same positions after the washing (Figure. 32B), which was not the case for the spheroids in liquid droplets, that were washed away after the immersion in the liquid (Figure. 32A). Therefore, we have demonstrated the gelation and stability of hydrogels formed by dispensing of hydrogel precursors in the droplets on DMA slide. In addition, the gelation of droplets and immersion of the slide in PBS improved imaging by eliminating the edge reflection observed in images taken before immersion in PBS (Figure. 32B). Edge effects can interfere with the analysis of the size and shape of spheroids positioned near the edges of the spots. Eliminating edge reflection ensures that all spheroids cultured on the chip can be analyzed.

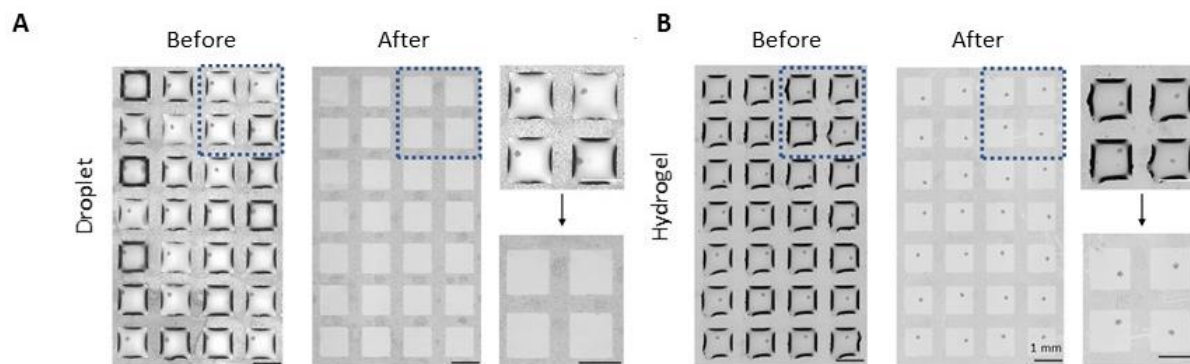


Figure 32. Gelation and stability of spheroids in hydrogels on DMA slide. The gelation and immersion of the slide in PBS and comparison presence and positioning of single spheroids inside hydrogels before and after the washing. A) and B) Microscope images of array of 4 x 7 liquid droplets (A) and hydrogels (B) containing single spheroids before and after immersion in PBS. Scale bar: 1mm.

In the next step, the selective sorting of cell spheroids was demonstrated through the gelation of spots of choice followed by the removal of content from the remaining spots on the DMA platform (Figure. 33A). This method enables precise control over which spheroids are retained and which are discarded, presenting significant implications for downstream applications. Initially, MCF-7 cells were used to create an array of cell spheroids on the DMA platform via the hanging drop method. Following 48 hours of incubation, the cell spheroids were successfully formed. To introduce selective differences, a staining solution containing Calcein-AM was applied to the droplets containing the spheroids in a pattern that spelled ‘KIT’, representing the author's affiliation (Figure. 33B). After a 30-minute incubation, hydrogel precursors were dispensed in the spots containing the Calcein-positive spheroids. Following an hour of incubation, the DMA slide was submerged in one well of a 4-well plate filled with PBS. The slide was then moved to another well of the same plate filled with PBS and imaged (Figure. 33C), demonstrating that the spheroids encapsulated in the hydrogel remained adhered to the DMA slide. The spots lacking Calcein-positive spheroids remained in liquid droplets, allowing for the collection of spheroids from these spots in the first well of the 4-well plate through a straightforward washing procedure. This approach showcases the successful selective gelation of targeted spots and the retrieval of spheroids of interest. The selective encapsulation of spheroids in hydrogel on the DMA platform is

Results and discussion

particularly advantageous for applications such as drug screening and the investigation of signaling pathways. For instance, previous studies have used the DMA platform for high-throughput drug screening, showcasing its ability to evaluate drug effects on spheroids.⁽¹⁷⁸⁾ Additionally, the propagation of Wnt signaling in spheroids was studied using this platform, further highlighting its application in analyzing complex biological processes.⁽¹⁷⁷⁾ By leveraging the selective patterning approach described here, it becomes feasible to isolate and analyze spheroids that respond to specific treatments. For example, spheroids exposed to a particular drug could be selectively encapsulated, facilitating targeted studies of signaling pathways within these spheroids and enhancing the precision and efficiency of subsequent analyses.

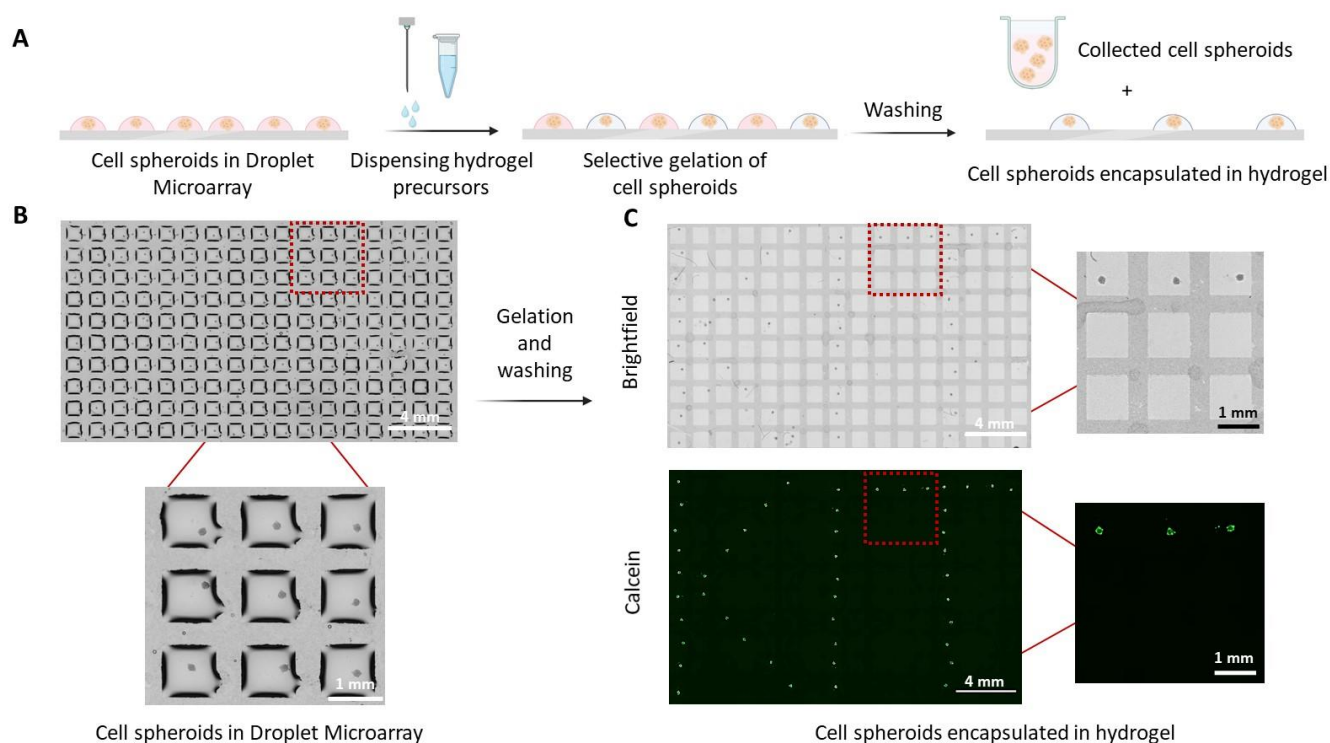


Figure 33. Sorting of cell spheroids. A) Schematics representation of the workflow for selective gelation of droplets containing spheroids on the DMA slide. B) Microscope image of the array of 10 x 17 droplets containing cell spheroids (upper panel), and close up of an array of 3 x 3 spots before gelation (lower panel). C) Brightfield (upper panel) and fluorescent (lower panel) microscope image of the array of 10 x 17 spots

Results and discussion

on DMA showing cell spheroids encapsulated in hydrogel after the selective gelation and washing off spheroids from not gelated droplets.

Next, the potential of using a gelation-degelation cycle for sorting spheroids encapsulated in hydrogel pads was demonstrated (Figure. 34A). First, MCF-7 cell spheroids were generated across the entire array of 672 spots on the DMA platform. For visualization purposes, the spheroids were stained with Calcein-AM (Figure. 34B). Hydrogel precursors were then dispensed in a pattern of two arrays of 7 x 7 spots (Figure. 34C). After gelation, the slide was washed with PBS, which led to the removal of all spheroids located in liquid droplets, leaving the spheroids within the hydrogel pads intact on the chip (Figure. 34C). Then, dextranase enzyme was applied to all hydrogel pads, followed by a 45-minute incubation period. The DMA slide was then washed with PBS, resulting in the removal of all spheroids from the surface, thus confirming the degelation of the hydrogels containing the spheroids (Figure. 34D). This approach presents a promising method for the controlled and selective fixation and sorting of cell spheroids on the DMA platform.

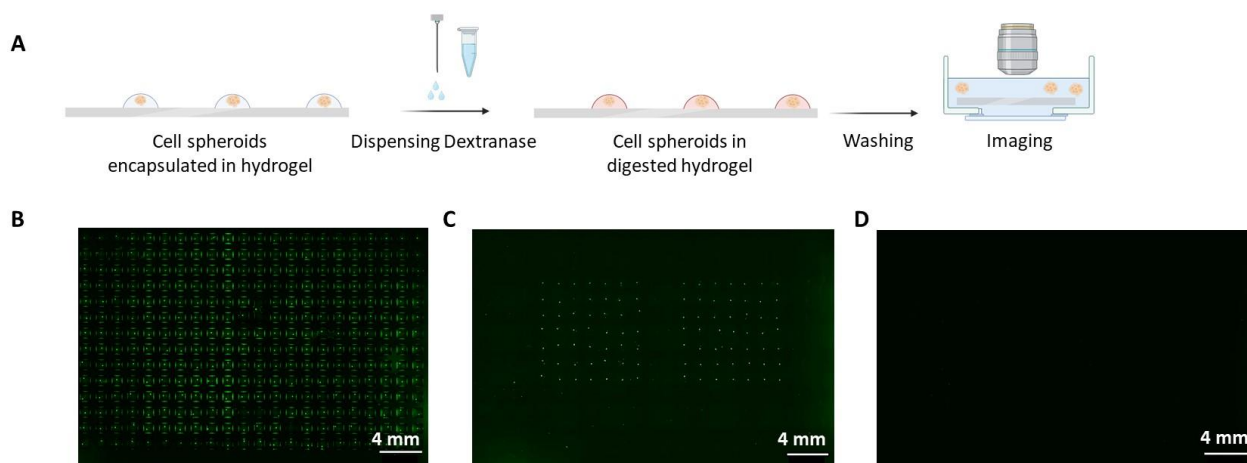


Figure 34. Digestion of hydrogel. A) Schematics representation of the workflow for digestion of hydrogel and returning the hydrogel pads to the liquid state. B) Fluorescent microscope image of the array of 22 x 14 droplets containing cell spheroids, stained with calcein. C) Fluorescent microscope image of 22 x 14 spots

of DMA slide with cell spheroids encapsulated in hydrogel after immersion of the slide in PBS. D) Fluorescent microscope image of DMA slide after digestion of the hydrogel-containing cell spheroids by Dextranase, immersed in PBS. Scale bar: 4 mm.

2.3.4. Summary

The transition from 2D cell culture models to more physiologically relevant 3D models has significantly advanced biomedical research, particularly in fields such as tissue engineering, disease modeling, and high-throughput drug screening. Hydrogels are one of the most promising tools for creating 3D cell cultures, which closely mimic the ECM. Despite their advantages, integrating 3D cultures into HTS workflows presents challenges, including the need for precise automation, compatibility with small volumes, and cost efficiency. The DMA platform, with its array of nanoliter-volume hydrophilic spots, offers a solution by enabling miniaturization and automation while reducing reagent consumption. Additionally, it allows for precise control over spheroid size by adjusting the number of cells seeded, enabling the creation of uniform single spheroid array. Unlike microtiter plates, where spheroids of varying sizes are distributed over a large area, the DMA platform ensures that spheroids are fixed within a 1 mm × 1 mm spot which simplifies the imaging and analysis.

This study aimed to develop a novel hydrogel-based 3D culture system on the DMA platform for high-throughput screening. The primary goal was to create stable, nanoliter-volume hydrogel arrays capable of supporting individual cells or cell spheroids. The system was designed to facilitate automated workflows, including selective gelation, washing, and medium immersion, for advanced applications in drug screening and precision medicine.

The project used a DMA chip containing 672 hydrophilic spots, each measuring 1 mm × 1 mm. A Dextran-PEG hydrogel system was selected for its slow gelling properties and compatibility with automated liquid handling. Two methods were developed to incorporate cells into the hydrogel arrays:

1. Pre-mixing Method: Cells were mixed with hydrogel precursors and dispensed onto the DMA slide.

2. On-chip Gelation Method: Cell suspensions or spheroids were dispensed as liquid droplets and gelated by adding hydrogel precursors to the droplets.

Cell viability and hydrogel stability were assessed through imaging and staining procedures. Additional experiments demonstrated selective gelation and a gelation-degelation cycle for spheroid sorting and fixation.

672 hydrogel pads were dispensed on a single slide under one minute. Hydrogel arrays demonstrated high structural integrity during washing and medium immersion, with no displacement of cells or spheroids. Jurkat cells cultured in hydrogels maintained high viability for up to 72 hours, comparable to cells cultured in liquid medium. The platform enabled the formation and gelation of single spheroids in droplets, with spheroids retaining their position and integrity during washing. The system allowed for selective gelation of target droplets, enabling the fixation of desired spheroids while washing away others. A gelation-degelation cycle further demonstrated the potential for advanced spheroid sorting.

This method allows for the rapid dispensing of hundreds of nanoliter-hydrogel droplets, with volume and cell density controlled precisely, thereby reducing reagent consumption and providing high-throughput applications. The stable nanoliter-hydrogel array on a chip allows experimental procedures such as washing and medium immersion to be conducted. Spheroid-containing droplets can be solidified at any point in the experiment, enabling the fixation of cell structures on the surface. Additionally, selective gelation of individual droplets enables spheroid sorting by stabilizing desired droplets while pooling others. This method can support high-throughput, miniaturized workflows in 3D microenvironments, advancing research in various fields such as cell, cell spheroid, or organoid screenings, drug screenings, and precision medicine.

3. Experimental part

Ethics and tissue acquisition

This study was conducted in accordance with the University of Heidelberg Ethics Committee of the Medical Faculty (Approval No: S-270/2001, title: Heidelberg Lung Biobank; Biomaterials and data for biomedical research to improve diagnostics as a basis for individualized therapy for lung diseases). All patients provided written informed consent prior to surgery, allowing the use of their tissue samples for research purposes. The consent process included detailed information about the study's aims and potential risks. Patients were assured that their participation was voluntary, and their identity would remain confidential.

Lung tumor tissues were obtained from patients diagnosed with NSCLC stage I to III, undergoing surgical resection at Thoraxklinik Heidelberg (University Hospital of Heidelberg, Germany). Samples were collected within 24 hours post-surgery and immediately processed for research purposes.

Cell culture

Patient-derived glioblastoma cell lines L0125 and L0512 were maintained in Neurocult Basal Medium with proliferation supplements (Cat. # 05751, Stemcell Technologies, Canada), 20 ng/mL EGF (Cat. # 78006.2, Stemcell Technologies, Canada), 20 ng/mL basic-FGF (Cat. # 78003.2, Stemcell Technologies, Canada), 2 µg/mL Heparin (Cat. # 07980, Stemcell Technologies, Canada), and 1% penicillin/streptomycin (Cat. # 15140-122, Gibco, Thermo Fisher Scientific, USA) at 37°C in a 5% CO₂ atmosphere in T25 flasks. The cells were routinely split once a week when reached a cell density of 3 x 10⁶ cells/mL. For splitting, the media containing cells was collected, and the flask was washed with PBS (Cat. # 10010-023, Gibco, Thermo Fisher Scientific, USA). The cells were centrifuged, resuspended in Accutase solution (Cat. # A6964, Merck, Germany), and incubated at 37°C to aid detachment. Following a series of washing and centrifugation steps, the

Experimental part

cells were resuspended in fresh media, counted, and replated at a density of 5×10^5 cells per T25 flask for further culture.

The Jurkat human T lymphocyte cell line was cultured in RPMI-1640 medium (Gibco, Life Technologies, USA) with the addition of 10% heat-inactivated fetal bovine serum (FBS, Sigma-Aldrich, USA) and 1% penicillin/streptomycin. The cells were maintained in T25 flasks at 37°C in a 5% CO₂ atmosphere and were routinely split every 2–3 days once reaching a cell density of 3×10^6 cells/mL.

MCF-7 human breast cancer cells (kindly provided by Dr. Oliver Kassel's research group, Institute of Biological and Chemical Systems (IBCS), Karlsruhe Institute of Technology (KIT)) were cultured in RPMI-1640 medium supplemented with 10% heat-inactivated FBS and 1% penicillin/streptomycin. The cells were split every 2–3 days when they reached 80% confluency and incubated at 37°C with 5% CO₂.

Tissue processing

Tissues were kept in DMEM medium until dissociation, which was performed within 24 hours post-surgery. Manual single-cell suspensions were generated as follows: tissues were transferred to a 10 cm Petri dish and cut into 1-2 mm pieces using sterile scalpels. The tissue pieces were then transferred to a 50 mL Falcon tube and pipetted up and down multiple times until a homogeneous suspension was achieved and then the suspension was centrifuged. Liberase DH (0.28 Units/mL, Roche, Switzerland) in DMEM culture medium was added to the pellet and incubated for 2 hours on an overhead rotator at 37°C. Cells were filtered using 100 µm and subsequently 40 µm cell strainers (Corning, USA) and centrifuged. The cells were then resuspended in PBS and loaded on top of Histopaque (Sigma-Aldrich, USA), followed by centrifugation for 20 minutes at 1800 x g without brake at room temperature. The separated cells were diluted with PBS and centrifuged again.

For semi-automated tumor dissociation, the human Tumor Dissociation Kit (Miltenyi Biotec, Germany) was used. The procedure followed the manufacturer's protocol using the gentleMACS™ Octo Dissociator with Heaters (Miltenyi Biotec, Germany). Tumor samples were minced with two

Experimental part

scalpels into 2-4 mm fragments and placed into gentleMACS™ C Tubes (Miltenyi Biotec, Germany) containing the enzyme mix and DMEM medium. These tubes were then placed onto the gentleMACS™ Octo Dissociator with Heaters, and the '37C_h_TDK_2' program was run. The cell suspension was filtered through 100 µm and 40 µm cell strainers, loaded on top of Histopaque, and diluted with PBS as previously described. Cells were maintained in DMEM/Ham's F-12 without Glutamine (Gibco, Thermo Fisher Scientific, USA) supplemented with Glutamax 100x (Gibco, Thermo Fisher Scientific, USA), 1% penicillin/streptomycin, 3 µg/mL of Rock inhibitor, and Airway Epithelial Cell Growth Medium Supplement Pack (Promocell, Germany): 0.004 mL/mL of Bovine Pituitary Extract, 10 ng/mL of Epidermal Growth Factor, 5 µg/mL of Insulin, 0.5 µg/mL of Hydrocortisone, 6.7 ng/mL of Triiodo-L-thyronine, and 10 µg/mL of Transferrin.

Printing cells on DMA

The DMA slides were purchased from Aquarray GmbH (Eggenstein-Leopoldshafen, Germany). The DMA slide (Catalogue number G-np-102) with 672 hydrophilic spots (1 mm × 1 mm) was used throughout the study. First, DMA slides were sterilized by immersion in 100% ethanol for 1 minute, followed by drying under a sterile bench for 20 min before use, according to the manufacturer's instructions. The cell concentration was adjusted to achieve the desired final number of cells in a 200 nL volume. Cells were seeded onto the DMA slides using an automated non-contact liquid dispenser, I-DOT One (Dispendix GmbH, Germany), at a volume of 200 nL per spot. The humidity during dispensing was adjusted to 70% using a humidifier connected to the IDOT One. After dispensing, the DMA slide containing cells was immediately placed inside a humidity-controlled Petri dish, also referred to as humidity chamber. This dish, a 10 cm Petri dish filled with 2 mL of PBS and covered with a lid containing a humidifying pad, was then placed in a standard cell culture incubator (37 °C and 5% CO₂).

Creating cell spheroids on DMA

The DMA slides were immersed in 100% ethanol and dried in clean bench for 20 minutes. Anti-adherence rinsing solution (STEMCELL Technologies Inc., Canada) was used to coat hydrophilic

Experimental part

spots and to reduce cell adhesion on DMA spots. 50 nL of anti-adherence rinsing solution was dispensed on each spot using I-DOT One dispenser. The DMA slides were then dried under clean bench for 15 minutes before being used for cell culture. Then, 200 nL of cell suspension with desired cell density was dispensed by I-DOT One dispenser on each spot under 70% humidity condition. The slide was inverted immediately after dispensing and placed on a “Spheroid table” (Catalogue number: AQP-0006, Aquarray GmbH, Germany) designed to enable the cultivation of DMA slides upside-down, facilitating the formation of 3D cell spheroids using the hanging drop method. The “spheroid table” with a slide on it was placed in a 10 cm Petri dish filled with 10 mL of PBS and covered with lid containing humidifying pad and placed in the cell culture incubator.

Immunostaining and flow cytometry

Cells were washed with PBS to remove the culture medium. The cells were then fixed with 4% paraformaldehyde (Thermo Fisher Scientific, USA) for 10 minutes at room temperature. All samples were blocked with a Blocker BSA solution (Thermo Fisher Scientific, USA) for 1 hour at room temperature. The samples were then incubated with the anti-EpCAM antibody (Santa Cruz Biotechnology, USA) at a concentration of 1:200 in 1% BSA overnight at 4°C. The following day, the samples were rinsed with PBS three times. For flow cytometry analysis, stained cells were resuspended in PBS and analyzed using a Guava easyCyte System (Luminex Corporation, USA) with GuavaSoft 4.5 software. Fluorescence compensation was applied to account for spectral overlap, and analysis, including gating strategy, was performed using FlowJo (FlowJo, LLC, USA). Quadrant gating was applied to identify EpCAM-positive and EpCAM-negative populations.

FDA Compounds Screening

The DMA slides were sterilized with 100% ethanol and dried under a clean bench for 20 minutes. Different drugs were printed on each spot of the DMA slides in advance of dispensing the cells. For each drug, 10 mM stock solutions were prepared in DMSO. A non-contact dispensing system (sciFLEXARRAYER S11 liquid dispenser, SCIENION AG, Germany) was used to print 2 nL of the drug solution in DMSO onto each spot. The CNS-Penetrant Compound Library (Catalog No.

Experimental part

L4700) was purchased from Selleck Chemicals LLC, and the drugs were printed on the DMA slide with a final drug concentration of 5 μM in droplets, in five replicates for each drug. For drug sensitivity testing of patient-derived lung cancer cells, vinorelbine, pemetrexed, cisplatin, carboplatin, cyclophosphamide, etoposide, topotecan, vincristine, docetaxel, paclitaxel, gemcitabine, and adriamycin were printed on the DMA slide in five different concentrations, as detailed in Table 2, with five replicates for each concentration. The outer rows were not used for drug screening due to edge effects. Additionally, 2 nL of DMSO was printed on the DMA slide as a control. The drug-printed DMA slides were dried in the dark at room temperature for 24 hours to ensure the evaporation of the DMSO content from the spots. The pre-dispensed slides were then stored in a dark box containing silica gel (Sigma-Aldrich Chemie, USA) before use.

Preparing hydrogel on DMA platform

Hydrogels were prepared using the 3-D Life Dextran-PEG Hydrogel SG Kit (#G92-1, Cellendes GmbH, Germany), which includes PEG-Link, 10 \times CB pH 7.5, water and SG Dextran. The gel was formed by combining 35.5 μL of water, 8 μL of 10 \times CB and 6.7 μL of SG-Polymer Dextran. Then, 40 μL of a cell suspension (2×10^6 cells/mL, corresponding to 300 cells per spot) was added, mixed thoroughly, followed by the addition of 10 μL of PEG-link crosslinker, resulting in a total volume of 100 μL . The mixture was immediately mixed by pipetting. The hydrogel was then dispensed onto hydrophilic spots in a volume of 150 nL using the automated I-DOT One liquid dispenser under a humidity setting of 70%. The DMA slide was incubated for 45 minutes in a cell culture incubator inside a humidity chamber. After gel formation, 150 nL of complete RPMI-1640 medium containing 10% FBS and 1% penicillin/streptomycin was dispensed on top of the hydrogel using Certus FLEX liquid dispenser (Gyger Fluidics GmbH, Switzerland). Afterwards, the DMA slide containing hydrogels covered with medium was placed into a 10 cm humidified Petri dish. Alternatively, the DMA slide was placed in a sterile 4-well plate and the well was filled with complete RPMI-1640 medium until the slide was fully immersed.

To digest the hydrogels, 19 nL of Dextranase enzyme (#D10-1, Cellendes GmbH, Germany) was dispensed onto the hydrogel pads, followed by incubation for 45 minutes in a cell culture incubator.

Formation of nanoliter hydrogel array containing 3D cell spheroids

Spheroids were first created by dispensing 200 nL of MCF-7 cell suspension at a concentration of 2.5×10^6 cells/mL, corresponding to 500 cells per spot, onto DMA spots pre-coated with Anti-adherence rinsing solution using an automated dispenser. The slide was then inverted and placed on a "spheroid table" to allow spheroid formation via the hanging drop method. This setup was then placed in a humidity chamber to enable the cells to form uniform 3D spheroids within 48 hours.

After the single spheroid array was formed, hydrogels were formed by mixing 21.24 μ L of 10x CB (pH 7.2), 17.8 μ L of SG Dextran, and 26.56 μ L of PEG-Link. The mixture was immediately dispensed into the droplets containing cell spheroids to encapsulate them, and the slides were incubated for 2 hours to solidify the hydrogels, creating a stable array of hydrogel containing the cell spheroids.

Viability assay

For staining the cells with fluorescent dyes, 50 nL of PBS containing Hoechst 33342 (10 mg/mL, Invitrogen™, USA), Calcein-AM (1 mg/mL, Invitrogen™, USA), and Propidium Iodide (1 mg/mL, Invitrogen™, USA) was dispensed onto the cells. The cells were incubated with the staining solution for 30 minutes in a cell culture incubator, followed by fluorescent microscopy for imaging.

For the cell viability assay using the Cell Counting Kit-8 (CCK-8) 500 T (Boster Biological Technology, USA), 100 nL of the reagent was dispensed onto droplets containing the cell spheroids. The samples were then incubated in a humidity chamber for 2 hours inside a cell culture incubator at 37°C and 5% CO₂ to allow for the formation of formazan, a colorimetric indicator of viable cells. After incubation, the entire slide was scanned using a standard document scanner (Epson Perfection V600, Seiko Epson Corporation, Japan) to capture the intensity of the color change, which correlates with cell viability. DMA spots containing only the medium and Kit-8

Experimental part

reagent were used to measure background signal, which was then subtracted from the experimental readings obtained from the cell samples.

Fluorescent microscopy

To perform microscopy, the DMA slide was placed in a 4-well plate with humidity pads and sealed with parafilm to reduce evaporation during imaging. Cells were monitored and imaged using the Keyence BZ-X810 microscope (Keyence, Japan) and an automated screening microscope, the Leica 3D Thunder Imager (Leica Microsystems, Germany), for both brightfield and fluorescent imaging. The images of the DMA slide containing hydrogel pads, representing the vertical dimension, were captured using a Keyence VHX-7000 microscope (Keyence, Japan). The data obtained from the microscopy was analyzed using ImageJ/Fiji software (National Institutes of Health, USA).

Data Analysis

Image analysis for fluorescent images to estimate the number of cells per spot was performed using the ImageJ/Fiji software. The images were first converted to 8-bit format, followed by manual adjustment of the threshold. To separate individual cells, the "Watershed" algorithm was applied. The "Analyze Particles" function was then used to quantify the number of stained cells in each spot. For automated processing of multiple images, the "Batch Macro" function was employed.

The color function in ImageJ was used to merge the red and green channels corresponding to Calcein and PI-positive cells respectively.

The diameter of spheroids in the brightfield channel were analyzed using Grid Screener.⁽¹⁴⁰⁾ The DMA array was detected in the semi-automated mode by marking the right and left borders of the top left, top right and bottom right spots of the figure. After identification of the grid, the evaluation method was chosen. The diameter of spheroids was evaluated with 'spheroid-analysis' after loading the respective image of the brightfield channel.

Experimental part

Dose-response curves were generated using GraphPad Prism (GraphPad Software, LLC, California, USA). Data were entered into an XY data table with five replicate response values for each drug concentration. The drug concentrations (X values) were log-transformed prior to curve fitting using the "Transform" analysis feature in Prism. Nonlinear regression was performed using the "log(agonist) vs. response -- Variable slope (four parameters)" model under the "Dose-response – Stimulation" equation group.

IC₅₀ values were determined by drawing a horizontal line at 50% viability on the dose-response plot. The intersection of this line with the fitted curve was used to identify the corresponding drug concentration on the log-transformed X-axis. This value was then antilog-transformed to calculate the IC₅₀ in terms of the original drug concentration. Error bars represent the standard deviation derived from the five replicates at each drug concentration.

All calculations and visualizations were created using Origin 2020b (OriginLab Corporation, USA) and GraphPad Prism.

Statistical Analysis

Data were analyzed using GraphPad Prism software. Error bars indicate standard deviation derived from the five replicates at each drug concentration. Statistical significance was determined using ordinary one-way ANOVA, with highly significant differences (****p < 0.0001, ***p < 0.001, **p < 0.01) for comparisons between different groups, while “NS” indicates nonsignificant statistical difference between the data groups.

Creation of Figures

Schematic figures and illustrations were created and designed using Biorender.com (Toronto, Canada).

4. Conclusion

Solid tumors, including lung cancer and gliomas, present major challenges in clinical practice due to their heterogeneity, aggressive progression, and often limited treatment options. Lung cancer remains the most common cause of cancer-related deaths globally, while glioblastomas, the most aggressive glioma subtype, are known for their poor prognosis and resistance to conventional therapies. These malignancies highlight an urgent need for innovative therapeutic strategies that can address their complexity and improve patient outcomes.

Functional precision oncology aims to tackle this challenge by using DSRT to experimentally assess the effect of various therapies on patient-derived tumor cells. This provides a more dynamic and personalized approach to treatment selection. However, applying this approach to clinical practice remains difficult due to challenges such as the limited number of cells available from minimal biopsies obtained from solid tumors, the high cost of compounds and reagents used in HTS workflows, and the considerable time needed to establish biological models and generate actionable data.

In Chapter 2.1, this study introduced a miniaturized DSRT workflow for NSCLC using the DMA slide. Unlike patient-derived organoids and PDX models, which can take weeks or months to establish, this method allows for the direct testing of cancer cells isolated from biopsy samples using a panel of drug candidates at various concentrations. The rapid workflow enables drug sensitivity testing within a clinically relevant timeframe of less than a week, facilitating the identification of the most effective therapies for each patient. This is particularly beneficial when quick, personalized treatment decisions can significantly impact patient outcomes.

The ability to perform high-throughput drug sensitivity testing with as few as 300 cells per 200 nanoliter droplet represents a major advancement, particularly for patients with advanced or metastatic lung cancer, where only small biopsy-derived samples are available. Traditional drug sensitivity testing typically requires significantly larger cell numbers and reagent volumes, making such approaches impractical for many patients. The DMA platform overcomes these limitations by

Conclusion

reducing the scale of testing. Each 200 nanoliter droplet requires hundreds to thousands of times fewer cells and reagents compared to traditional 96 and 384-well plates. This reduction not only makes high-throughput screening feasible with minimal patient material, but it also significantly lowers the cost of testing by conserving expensive reagents. Additionally, the miniaturized format allows for the simultaneous testing of a larger panel of drug candidates and concentration gradients, providing a comprehensive drug sensitivity profile in a single experiment.

The reliability of this approach was confirmed through experiments that tested the reproducibility of drug sensitivity results. The viability and drug response data were highly similar for cell densities of 300, 500, and 700 cells per droplet, demonstrating that testing with as few as 300 cells per droplet produced consistent results. The platform was able to capture both inter- and intra-patient variability in drug responses. For example, cells from different patients with the same cancer subtype showed varying sensitivities to vinorelbine, with cell viability ranging from 33.8% to 58.5% at 1 μ M. The study also explored intratumor heterogeneity by analyzing drug responses from three distinct tumor regions, revealing differences in sensitivity to certain drugs, such as carboplatin. Furthermore, the feasibility of using needle biopsy-derived samples was demonstrated, expanding DSRT to patients who are not candidates for surgical tumor resection.

Thus, this work represents a significant step forward in the field of precision oncology. By leveraging a miniaturized, high-throughput DSRT platform, it enables rapid, patient-specific drug sensitivity testing using minimal cell input. This innovative approach holds great promise for improving treatment outcomes in lung cancer and beyond, particularly for patients with limited tissue samples, and sets the stage for more personalized cancer care.

In Chapter 2.2, high-throughput drug screening using CNS-penetrating drugs on glioblastoma tumorsphere cell lines was performed. DAC pre-treatment was used to sensitize glioblastoma cells to a library of blood-brain barrier-penetrating drugs. The use of DAC as a sensitizing agent is beneficial because it reverses epigenetic changes and restores sensitivity to chemotherapy. High-throughput drug screening was performed in two conditions: cells pretreated with DAC and cells untreated with DAC, to investigate whether pretreatment with DAC sensitizes the cells to treatment.

Conclusion

The glioblastoma tumor sphere cell lines L0125 and L0512 used in this study are slow-growing, but miniaturization of the assay using DMA slide reduced costs and increased throughput, making it suitable for the slow-growing nature of glioma tumor spheres. Only 300 cells were required to form uniform spheroids on the DMA slide, which could then grow on the chip for 72 hours. In this study the results of screening with 533 drugs on L0125 and 356 drugs on L0512 cell line are presented. The cells were tested in both DAC-pretreated and untreated conditions, allowing a direct comparison of drug efficacy in the presence or absence of DAC-induced sensitization.

A dual readout system combining the Kit-8 assay for cell viability and fluorescent staining (Calcein/PI) to assess live and dead cells provided a comprehensive evaluation of drug efficacy. This approach enhanced the reliability and accuracy of the results, ensuring that the observed effects were due to drug-induced toxicity rather than assay artifacts.

Several drugs showed greater therapeutic potential when combined with DAC. For example, Obatoclax Mesylate and Trametinib demonstrated increased effectiveness when tested on DAC-pretreated L0125 cells, while SNS-032 and AZD5438 showed enhanced efficacy on DAC-pretreated L0512 cells compared to DAC-untreated cells, suggesting that DAC pretreatment improved their activity. Vorinostat and Epoxomicin were effective on L0125 cells in both DAC-pretreated and untreated conditions, while Epirubicin showed efficacy on L0512 cells under both conditions. Flavopiridol and Givinostat demonstrated effectiveness on both cell lines. Next, a method will be developed to quantify Kit-8 staining and PI signal intensities, providing insights into whether DAC enhances the efficacy of these drugs. To validate the findings and generate dose-response curves, eleven concentrations of each drug will be prepared. The cell lines will then be tested at these concentrations under both DAC-pretreated and untreated conditions using 384-well plates.

In Chapter 2.3, a stable array of nanoliter-volume hydrogels capable of supporting cells or cell spheroids on DMA slide was introduced. The DMA platform was used to establish a homogeneous nanoliter-volume array of hydrogels containing cells or spheroids in a fast, automated, and high-throughput manner. Automated dispensing of hydrogels was successfully demonstrated, with 672 homogeneous hydrogels of 150 nL volume created in under a minute. This precise control over volume and cell density highlights the platform's potential to advance high-throughput screening

Conclusion

in 3D cell cultures. Two distinct methods were developed for integrating cells into hydrogel arrays: pre-mixing cells with hydrogel precursors and on-chip gelation of cell-laden droplets. These methods ensure flexibility, allowing researchers to tailor the workflow to specific experimental needs. Miniaturization of the hydrogel array to 150 nL per spot results in a 2- to 3-order magnitude reduction in reagent consumption compared to traditional microtiter plates. This reduction not only conserves reagents but also lowers the cost of testing by requiring 10 to 100 times fewer cells per experimental point, making it ideal for screening rare and limited cell samples, such as patient-derived cells from solid tumor biopsies.

The stability of the nanoliter hydrogel array during washing steps has been demonstrated, allowing the immobilization of cells or spheroids at precise locations on the DMA slide. This is not feasible with liquid media droplets containing suspension cells or unattached spheroids. Additionally, selective gelation of spheroids within nanoliter droplets enables on-chip spheroid sorting and patterning.

This approach can be adaptable for miniaturized screening workflows in 3D microenvironments, including assays for cell migration, invasion, spheroid sorting, and drug sensitivity testing in functional precision oncology.

In conclusion, this study highlights the significant potential of miniaturized DSRT using the DMA platform to advance functional precision oncology, particularly for solid tumors. By leveraging the miniaturization and automation capabilities of the DMA, high-throughput drug sensitivity testing can be performed with minimal cell input, making it a valuable tool for personalized cancer treatment.

5. References

1. Brown JS, Amend SR, Austin RH, Gatenby RA, Hammarlund EU, Pienta KJ. Updating the Definition of Cancer. *Mol Cancer Res.* 2023;21(11):1142-7.
2. Siegel RL, Miller KD, Wagle NS, Jemal A. Cancer statistics, 2023. *CA Cancer J Clin.* 2023;73(1):17-48.
3. 'World Health Organization. Global cancer burden growing, amidst mounting need for services 2024 [Available from: <https://www.who.int/news/item/01-02-2024-global-cancer-burden-growing--amidst-mounting-need-for-services>.
4. Cooper G. *The Cell: A Molecular Approach*: Sunderland (MA): Sinauer Associates; 2000. Available from: <https://www.ncbi.nlm.nih.gov/books/NBK9963/>.
5. Chen R, Smith-Cohn M, Cohen AL, Colman H. Glioma Subclassifications and Their Clinical Significance. *Neurotherapeutics.* 2017;14(2):284-97.
6. Krzyszczyk P, Acevedo A, Davidoff EJ, Timmins LM, Marrero-Berrios I, Patel M, et al. The growing role of precision and personalized medicine for cancer treatment. *Technology (Singap World Sci).* 2018;6(3-4):79-100.
7. Zhou Y, Tao L, Qiu J, Xu J, Yang X, Zhang Y, et al. Tumor biomarkers for diagnosis, prognosis and targeted therapy. *Signal Transduction and Targeted Therapy.* 2024;9(1):132.
8. Kinnersley B, Sud A, Everall A, Cornish AJ, Chubb D, Culliford R, et al. Analysis of 10,478 cancer genomes identifies candidate driver genes and opportunities for precision oncology. *Nature Genetics.* 2024.
9. Rulten SL, Grose RP, Gatz SA, Jones JL, Cameron AJM. The Future of Precision Oncology. *Int J Mol Sci.* 2023;24(16).
10. Malone ER, Oliva M, Sabatini PJB, Stockley TL, Siu LL. Molecular profiling for precision cancer therapies. *Genome Medicine.* 2020;12(1):8.
11. Shuel SL. Targeted cancer therapies: Clinical pearls for primary care. *Can Fam Physician.* 2022;68(7):515-8.
12. van Renterghem AWJ, van de Haar J, Voest EE. Functional precision oncology using patient-derived assays: bridging genotype and phenotype. *Nature Reviews Clinical Oncology.* 2023;20(5):305-17.
13. Marusyk A, Janiszewska M, Polyak K. Intratumor Heterogeneity: The Rosetta Stone of Therapy Resistance. *Cancer Cell.* 2020;37(4):471-84.
14. Letai A, Bhola P, Welm AL. Functional precision oncology: Testing tumors with drugs to identify vulnerabilities and novel combinations. *Cancer Cell.* 2022;40(1):26-35.
15. Panovska D, De Smet F. Functional Precision Oncology: The Next Frontier to Improve Glioblastoma Outcome? *Int J Mol Sci.* 2022;23(15).
16. Ayuda-Durán P, Hermansen JU, Giliberto M, Yin Y, Hanes R, Gordon S, et al. Standardized assays to monitor drug sensitivity in hematologic cancers. *Cell Death Discov.* 2023;9(1):435.
17. Popova AA, Levkin PA. Precision Medicine in Oncology: In Vitro Drug Sensitivity and Resistance Test (DSRT) for Selection of Personalized Anticancer Therapy. *Advanced Therapeutics.* 2020;3(2):1900100.
18. Dinić J, Jovanović Stojanov S, Dragoj M, Grozdanić M, Podolski-Renić A, Pešić M. Cancer Patient-Derived Cell-Based Models: Applications and Challenges in Functional Precision Medicine. *Life.* 2024;14(9):1142.

References

19. Ashburn TT, Thor KB. Drug repositioning: identifying and developing new uses for existing drugs. *Nat Rev Drug Discov*. 2004;3(8):673-83.
20. Breckenridge A, Jacob R. Overcoming the legal and regulatory barriers to drug repurposing. *Nat Rev Drug Discov*. 2019;18(1):1-2.
21. Pushpakom S, Iorio F, Eyers PA, Escott KJ, Hopper S, Wells A, et al. Drug repurposing: progress, challenges and recommendations. *Nature Reviews Drug Discovery*. 2019;18(1):41-58.
22. Rivero-García I, Castresana-Aguirre M, Guglielmo L, Guala D, Sonnhämmer ELL. Drug repurposing improves disease targeting 11-fold and can be augmented by network module targeting, applied to COVID-19. *Scientific Reports*. 2021;11(1):20687.
23. Lexchin J. Bigger and better: how Pfizer redefined erectile dysfunction. *PLoS Med*. 2006;3(4):e132.
24. Singhal S, Mehta J, Desikan R, Ayers D, Roberson P, Eddlemon P, et al. Antitumor activity of thalidomide in refractory multiple myeloma. *N Engl J Med*. 1999;341(21):1565-71.
25. Schipper LJ, Zevenijn LJ, Garnett MJ, Voest EE. Can Drug Repurposing Accelerate Precision Oncology? *Cancer Discov*. 2022;12(7):1634-41.
26. Szymański P, Markowicz M, Mikiciuk-Olasik E. Adaptation of high-throughput screening in drug discovery-toxicological screening tests. *Int J Mol Sci*. 2012;13(1):427-52.
27. Mayr LM, Fuerst P. The future of high-throughput screening. *J Biomol Screen*. 2008;13(6):443-8.
28. Silva TC, Eppink M, Ottens M. Automation and miniaturization: enabling tools for fast, high-throughput process development in integrated continuous biomanufacturing. *Journal of Chemical Technology & Biotechnology*. 2022;97(9):2365-75.
29. Kapałczyńska M, Kolenda T, Przybyła W, Zajączkowska M, Teresiak A, Filas V, et al. 2D and 3D cell cultures - a comparison of different types of cancer cell cultures. *Arch Med Sci*. 2018;14(4):910-9.
30. Kim S, Lee Y, Song BR, Sim H, Kang EH, Hwang M, et al. Drug Response of Patient-Derived Lung Cancer Cells Predicts Clinical Outcomes of Targeted Therapy. *Cancers*. 2024;16(4):778.
31. Pampaloni F, Reynaud EG, Stelzer EH. The third dimension bridges the gap between cell culture and live tissue. *Nat Rev Mol Cell Biol*. 2007;8(10):839-45.
32. Baker BM, Chen CS. Deconstructing the third dimension: how 3D culture microenvironments alter cellular cues. *J Cell Sci*. 2012;125(Pt 13):3015-24.
33. Petersen OW, Rønnov-Jessen L, Howlett AR, Bissell MJ. Interaction with basement membrane serves to rapidly distinguish growth and differentiation pattern of normal and malignant human breast epithelial cells. *Proc Natl Acad Sci U S A*. 1992;89(19):9064-8.
34. Kilian KA, Bugarija B, Lahn BT, Mrksich M. Geometric cues for directing the differentiation of mesenchymal stem cells. *Proc Natl Acad Sci U S A*. 2010;107(11):4872-7.
35. Fischbach C, Chen R, Matsumoto T, Schmelzle T, Brugge JS, Polverini PJ, Mooney DJ. Engineering tumors with 3D scaffolds. *Nat Methods*. 2007;4(10):855-60.
36. Cukierman E, Pankov R, Stevens DR, Yamada KM. Taking cell-matrix adhesions to the third dimension. *Science*. 2001;294(5547):1708-12.
37. Maltman DJ, Przyborski SA. Developments in three-dimensional cell culture technology aimed at improving the accuracy of in vitro analyses. *Biochem Soc Trans*. 2010;38(4):1072-5.
38. Griffith LG, Swartz MA. Capturing complex 3D tissue physiology in vitro. *Nat Rev Mol Cell Biol*. 2006;7(3):211-24.
39. Nakazawa MS, Keith B, Simon MC. Oxygen availability and metabolic adaptations. *Nat Rev Cancer*. 2016;16(10):663-73.
40. Tufail M, Jiang C-H, Li N. Altered metabolism in cancer: insights into energy pathways and therapeutic targets. *Molecular Cancer*. 2024;23(1):203.
41. Chen G, Wu K, Li H, Xia D, He T. Role of hypoxia in the tumor microenvironment and targeted therapy. *Front Oncol*. 2022;12:961637.

References

42. Nayak P, Bentivoglio V, Varani M, Signore A. Three-Dimensional In Vitro Tumor Spheroid Models for Evaluation of Anticancer Therapy: Recent Updates. *Cancers*. 2023;15(19):4846.
43. Hirschhaeuser F, Menne H, Dittfeld C, West J, Mueller-Klieser W, Kunz-Schughart LA. Multicellular tumor spheroids: an underestimated tool is catching up again. *J Biotechnol*. 2010;148(1):3-15.
44. Hofmann S, Cohen-Harazi R, Maizels Y, Koman I. Patient-derived tumor spheroid cultures as a promising tool to assist personalized therapeutic decisions in breast cancer. *Translational Cancer Research*. 2021;11(1):134-47.
45. Maritan SM, Lian EY, Mulligan LM. An Efficient and Flexible Cell Aggregation Method for 3D Spheroid Production. *J Vis Exp*. 2017(121).
46. Zhang L, Su P, Xu C, Yang J, Yu W, Huang D. Chondrogenic differentiation of human mesenchymal stem cells: a comparison between micromass and pellet culture systems. *Biotechnol Lett*. 2010;32(9):1339-46.
47. Carlsson J, Yuhas JM. Liquid-overlay culture of cellular spheroids. *Recent Results Cancer Res*. 1984;95:1-23.
48. Carvalho MP, Costa EC, Miguel SP, Correia IJ. Tumor spheroid assembly on hyaluronic acid-based structures: A review. *Carbohydr Polym*. 2016;150:139-48.
49. Timmins NE, Nielsen LK. Generation of multicellular tumor spheroids by the hanging-drop method. *Methods Mol Med*. 2007;140:141-51.
50. Bartosh TJ, Ylostalo JH. Preparation of anti-inflammatory mesenchymal stem/precursor cells (MSCs) through sphere formation using hanging-drop culture technique. *Curr Protoc Stem Cell Biol*. 2014;28:2b.6.1-2b.6.23.
51. Achilli TM, Meyer J, Morgan JR. Advances in the formation, use and understanding of multi-cellular spheroids. *Expert Opin Biol Ther*. 2012;12(10):1347-60.
52. Manley P, Lelkes PI. A novel real-time system to monitor cell aggregation and trajectories in rotating wall vessel bioreactors. *J Biotechnol*. 2006;125(3):416-24.
53. Anil-Inevi M, Yaman S, Yildiz AA, Mese G, Yalcin-Ozuysal O, Tekin HC, Ozcivici E. Biofabrication of in situ Self Assembled 3D Cell Cultures in a Weightlessness Environment Generated using Magnetic Levitation. *Sci Rep*. 2018;8(1):7239.
54. Sato T, Vries RG, Snippert HJ, van de Wetering M, Barker N, Stange DE, et al. Single Lgr5 stem cells build crypt-villus structures in vitro without a mesenchymal niche. *Nature*. 2009;459(7244):262-5.
55. Idrisova KF, Simon HU, Gomzikova MO. Role of Patient-Derived Models of Cancer in Translational Oncology. *Cancers (Basel)*. 2022;15(1).
56. Lv J, Du X, Wang M, Su J, Wei Y, Xu C. Construction of tumor organoids and their application to cancer research and therapy. *Theranostics*. 2024;14(3):1101-25.
57. Gunti S, Hoke ATK, Vu KP, London NR, Jr. Organoid and Spheroid Tumor Models: Techniques and Applications. *Cancers (Basel)*. 2021;13(4).
58. El Harane S, Zidi B, El Harane N, Krause KH, Matthes T, Preynat-Seauve O. Cancer Spheroids and Organoids as Novel Tools for Research and Therapy: State of the Art and Challenges to Guide Precision Medicine. *Cells*. 2023;12(7).
59. Dekkers JF, Alieva M, Wellens LM, Ariese HCR, Jamieson PR, Vonk AM, et al. High-resolution 3D imaging of fixed and cleared organoids. *Nat Protoc*. 2019;14(6):1756-71.
60. Hofer M, Lutolf MP. Engineering organoids. *Nature Reviews Materials*. 2021;6(5):402-20.
61. Andrews MG, Kriegstein AR. Challenges of Organoid Research. *Annu Rev Neurosci*. 2022;45:23-39.
62. Regmi S, Poudel C, Adhikari R, Luo KQ. Applications of Microfluidics and Organ-on-a-Chip in Cancer Research. *Biosensors (Basel)*. 2022;12(7).
63. Wang Y, Chen Z, Bian F, Shang L, Zhu K, Zhao Y. Advances of droplet-based microfluidics in drug discovery. *Expert Opin Drug Discov*. 2020;15(8):969-79.

References

64. Tevlek A, Kecili S, Ozcelik OS, Kulah H, Tekin HC. Spheroid Engineering in Microfluidic Devices. *ACS Omega*. 2023;8(4):3630-49.
65. Schuster B, Junkin M, Kashaf SS, Romero-Calvo I, Kirby K, Matthews J, et al. Automated microfluidic platform for dynamic and combinatorial drug screening of tumor organoids. *Nature Communications*. 2020;11(1):5271.
66. Prince E, Kheiri S, Wang Y, Xu F, Cruickshank J, Topolskaia V, et al. Microfluidic Arrays of Breast Tumor Spheroids for Drug Screening and Personalized Cancer Therapies. *Advanced Healthcare Materials*. 2022;11(1):2101085.
67. Pong KCC, Lai YS, Wong RCH, Lee ACK, Chow SCT, Lam JCW, et al. Automated Uniform Spheroid Generation Platform for High Throughput Drug Screening Process. *Biosensors (Basel)*. 2024;14(8).
68. Veith I, Nurmik M, Mencattini A, Damei I, Lansche C, Brosseau S, et al. Assessing personalized responses to anti-PD-1 treatment using patient-derived lung tumor-on-chip. *Cell Reports Medicine*. 2024;5(5).
69. Yoshida GJ. Applications of patient-derived tumor xenograft models and tumor organoids. *Journal of Hematology & Oncology*. 2020;13(1):4.
70. Liu Y, Wu W, Cai C, Zhang H, Shen H, Han Y. Patient-derived xenograft models in cancer therapy: technologies and applications. *Signal Transduct Target Ther*. 2023;8(1):160.
71. Guillen KP, Fujita M, Butterfield AJ, Scherer SD, Bailey MH, Chu Z, et al. A human breast cancer-derived xenograft and organoid platform for drug discovery and precision oncology. *Nature Cancer*. 2022;3(2):232-50.
72. Jin J, Yoshimura K, Sewastjanow-Silva M, Song S, Ajani JA. Challenges and Prospects of Patient-Derived Xenografts for Cancer Research. *Cancers (Basel)*. 2023;15(17).
73. Kim J, Koo B-K, Knoblich JA. Human organoids: model systems for human biology and medicine. *Nature Reviews Molecular Cell Biology*. 2020;21(10):571-84.
74. Ganesh K, Massagué J. Targeting metastatic cancer. *Nat Med*. 2021;27(1):34-44.
75. Dupain C, Masliah-Planchon J, Gu C, Girard E, Gestraud P, Du Rusquec P, et al. Fine-needle aspiration as an alternative to core needle biopsy for tumour molecular profiling in precision oncology: prospective comparative study of next-generation sequencing in cancer patients included in the SHIVA02 trial. *Mol Oncol*. 2021;15(1):104-15.
76. Cooper KE, Abdallah KE, Angove RSM, Gallagher KD, Bonham VL. Navigating Access to Cancer Care: Identifying Barriers to Precision Cancer Medicine. *Ethn Dis*. 2022;32(1):39-48.
77. Mattar M, McCarthy CR, Kulick AR, Qeriqi B, Guzman S, de Stanchina E. Establishing and Maintaining an Extensive Library of Patient-Derived Xenograft Models. *Front Oncol*. 2018;8:19.
78. Wang E, Xiang K, Zhang Y, Wang X-F. Patient-derived organoids (PDOs) and PDO-derived xenografts (PDOXs): New opportunities in establishing faithful pre-clinical cancer models. *Journal of the National Cancer Center*. 2022;2(4):263-76.
79. Cardoso BD, Castanheira EMS, Lanceros-Méndez S, Cardoso VF. Recent Advances on Cell Culture Platforms for In Vitro Drug Screening and Cell Therapies: From Conventional to Microfluidic Strategies. *Advanced Healthcare Materials*. 2023;12(18):2202936.
80. Cui P, Wang S. Application of microfluidic chip technology in pharmaceutical analysis: A review. *Journal of Pharmaceutical Analysis*. 2019;9(4):238-47.
81. Benz M, Asperger A, Hamester M, Welle A, Heissler S, Levkin PA. A combined high-throughput and high-content platform for unified on-chip synthesis, characterization and biological screening. *Nature Communications*. 2020;11(1):5391.
82. Feng W, Ueda E, Levkin PA. Droplet Microarrays: From Surface Patterning to High-Throughput Applications. *Advanced Materials*. 2018;30(20):1706111.

References

83. Chakraborty S, Gourain V, Benz M, Scheiger JM, Levkin PA, Popova AA. Droplet microarrays for cell culture: effect of surface properties and nanoliter culture volume on global transcriptomic landscape. *Materials Today Bio.* 2021;11:100112.
84. Geyer FL, Ueda E, Liebel U, Grau N, Levkin PA. Superhydrophobic-superhydrophilic micropatterning: towards genome-on-a-chip cell microarrays. *Angew Chem Int Ed Engl.* 2011;50(36):8424-7.
85. Popova AA, Schillo SM, Demir K, Ueda E, Nesterov-Mueller A, Levkin PA. Droplet-Array (DA) Sandwich Chip: A Versatile Platform for High-Throughput Cell Screening Based on Superhydrophobic-Superhydrophilic Micropatterning. *Adv Mater.* 2015;27(35):5217-22.
86. Huhtamäki T, Tian X, Korhonen JT, Ras RHA. Surface-wetting characterization using contact-angle measurements. *Nat Protoc.* 2018;13(7):1521-38.
87. Barati Darband G, Aliofkhazraei M, Khorsand S, Sokhanvar S, Kaboli A. Science and Engineering of Superhydrophobic Surfaces: Review of Corrosion Resistance, Chemical and Mechanical Stability. *Arabian Journal of Chemistry.* 2020;13(1):1763-802.
88. Jokinen V, Sainiemi L, Franssila S. Complex Droplets on Chemically Modified Silicon Nanoglass. *Advanced Materials.* 2008;20(18):3453-6.
89. Feng W, Li L, Ueda E, Li J, Heißler S, Welle A, et al. Surface Patterning via Thiol-Yne Click Chemistry: An Extremely Fast and Versatile Approach to Superhydrophilic-Superhydrophobic Micropatterns. *Advanced Materials Interfaces.* 2014;1(7):1400269.
90. Popova A DK, Hartanto T.G. , Schmitt E. and Levkin P. A. Droplet-microarray on superhydrophobic–superhydrophilic patterns for high-throughput live cell screenings. *RSC Adv.* 2016;6:38263 –76
91. Chakraborty S, Gourain V, Benz M, Scheiger JM, Levkin PA, Popova AA. Droplet microarrays for cell culture: effect of surface properties and nanoliter culture volume on global transcriptomic landscape. *Mater Today Bio.* 2021;11:100112.
92. Chakraborty S, Luchena C, Elton JJ, Schilling MP, Reischl M, Roux M, et al. “Cells-to-cDNA on Chip”: Phenotypic Assessment and Gene Expression Analysis from Live Cells in Nanoliter Volumes Using Droplet Microarrays. *Advanced Healthcare Materials.* 2022;11(12):2102493.
93. Tronser T, Demir K, Reischl M, Bastmeyer M, Levkin PA. Droplet microarray: miniaturized platform for rapid formation and high-throughput screening of embryoid bodies. *Lab Chip.* 2018;18(15):2257-69.
94. Popova AA, Tronser T, Demir K, Haitz P, Kuodyte K, Starkuviene V, et al. Facile One Step Formation and Screening of Tumor Spheroids Using Droplet-Microarray Platform. *Small.* 2019;15(25):e1901299.
95. Cui H, Wang X, Wesslowski J, Tronser T, Rosenbauer J, Schug A, et al. Assembly of Multi-Spheroid Cellular Architectures by Programmable Droplet Merging. *Adv Mater.* 2021;33(4):e2006434.
96. Liu Y, Bertels S, Reischl M, Peravali R, Bastmeyer M, Popova AA, Levkin PA. Droplet Microarray Based Screening Identifies Proteins for Maintaining Pluripotency of hiPSCs. *Advanced Healthcare Materials.* 2022;11(18):2200718.
97. Lei W, Deckers A, Luchena C, Popova A, Reischl M, Jung N, et al. Droplet Microarray as a Powerful Platform for Seeking New Antibiotics Against Multidrug-Resistant Bacteria. *Advanced Biology.* 2022;6(12):2200166.
98. Popova AA, Marcato D, Peravali R, Wehl I, Schepers U, Levkin PA. Fish-Microarray: A Miniaturized Platform for Single-Embryo High-Throughput Screenings. *Advanced Functional Materials.* 2018;28(3):1703486.
99. Rosenfeld A, Oelschlaeger C, Thelen R, Heissler S, Levkin PA. Miniaturized high-throughput synthesis and screening of responsive hydrogels using nanoliter compartments. *Materials Today Bio.* 2020;6:100053.

References

100. Popova AA, Dietrich S, Huber W, Reischl M, Peravali R, Levkin PA. Miniaturized Drug Sensitivity and Resistance Test on Patient-Derived Cells Using Droplet-Microarray. *SLAS Technol.* 2021;26(3):274-86.
101. Kästner A, Kron A, van den Berg N, Moon K, Scheffler M, Schillinger G, et al. Evaluation of the effectiveness of a nationwide precision medicine program for patients with advanced non-small cell lung cancer in Germany: a historical cohort analysis. *The Lancet Regional Health – Europe.* 2024;36.
102. Hendriks LEL, Remon J, Faivre-Finn C, Garassino MC, Heymach JV, Kerr KM, et al. Non-small-cell lung cancer. *Nature Reviews Disease Primers.* 2024;10(1):71.
103. Lynch TJ, Bell DW, Sordella R, Gurubhagavatula S, Okimoto RA, Brannigan BW, et al. Activating mutations in the epidermal growth factor receptor underlying responsiveness of non-small-cell lung cancer to gefitinib. *N Engl J Med.* 2004;350(21):2129-39.
104. Zhang H, Zhang Y, Zhu Y, Dong T, Liu Z. Understanding the treatment response and resistance to targeted therapies in non-small cell lung cancer: clinical insights and perspectives. *Frontiers in Oncology.* 2024;14.
105. Frost N, Griesinger F, Hoffmann H, Länger F, Nestle U, Schütte W, et al. Lung Cancer in Germany. *J Thorac Oncol.* 2022;17(6):742-50.
106. Rossi A, Di Maio M. Platinum-based chemotherapy in advanced non-small-cell lung cancer: optimal number of treatment cycles. *Expert Rev Anticancer Ther.* 2016;16(6):653-60.
107. Ricciardi S, Tomao S, de Marinis F. Pemetrexed as first-line therapy for non-squamous non-small cell lung cancer. *Ther Clin Risk Manag.* 2009;5:781-7.
108. Paik PK, Kim RK, Ahn L, Plodkowski AJ, Ni A, Donoghue MTA, et al. A Phase II Trial of Albumin-Bound Paclitaxel and Gemcitabine in Patients with Newly Diagnosed Stage IV Squamous Cell Lung Cancers. *Clin Cancer Res.* 2020;26(8):1796-802.
109. Tomasini P, Barlesi F, Mascaux C, Greillier L. Pemetrexed for advanced stage nonsquamous non-small cell lung cancer: latest evidence about its extended use and outcomes. *Ther Adv Med Oncol.* 2016;8(3):198-208.
110. Sha C, Lee PC. EGFR-Targeted Therapies: A Literature Review. *Journal of Clinical Medicine.* 2024;13(21):6391.
111. Min H-Y, Lee H-Y. Mechanisms of resistance to chemotherapy in non-small cell lung cancer. *Archives of Pharmacol Research.* 2021;44(2):146-64.
112. Ding S, Hsu C, Wang Z, Natesh NR, Millen R, Negrete M, et al. Patient-derived micro-organospheres enable clinical precision oncology. *Cell Stem Cell.* 2022;29(6):905-17.e6.
113. Kita K, Fukuda K, Takahashi H, Tanimoto A, Nishiyama A, Arai S, et al. Patient-derived xenograft models of non-small cell lung cancer for evaluating targeted drug sensitivity and resistance. *Cancer Sci.* 2019;110(10):3215-24.
114. Sung S, Heymann JJ, Crapanzano JP, Moreira AL, Shu C, Bulman WA, Saqi A. Lung cancer cytology and small biopsy specimens: diagnosis, predictive biomarker testing, acquisition, triage, and management. *Journal of the American Society of Cytopathology.* 2020;9(5):332-45.
115. Satofuka H, Wang Y, Yamazaki K, Hamamichi S, Fukuhara T, Rafique A, et al. Characterization of human anti-EpCAM antibodies for developing an antibody–drug conjugate. *Scientific Reports.* 2023;13(1):4225.
116. Lv X, Mao Z, Sun X, Liu B. Intratumoral Heterogeneity in Lung Cancer. *Cancers (Basel).* 2023;15(10).
117. Kodack DP, Farago AF, Dastur A, Held MA, Dardaei L, Friboulet L, et al. Primary Patient-Derived Cancer Cells and Their Potential for Personalized Cancer Patient Care. *Cell Rep.* 2017;21(11):3298-309.
118. Yang W, Soares J, Greninger P, Edelman EJ, Lightfoot H, Forbes S, et al. Genomics of Drug Sensitivity in Cancer (GDSC): a resource for therapeutic biomarker discovery in cancer cells. *Nucleic Acids Research.* 2012;41(D1):D955-D61.

References

119. Xiao Y, Yu D. Tumor microenvironment as a therapeutic target in cancer. *Pharmacol Ther.* 2021;221:107753.
120. Hirata E, Sahai E. Tumor Microenvironment and Differential Responses to Therapy. *Cold Spring Harb Perspect Med.* 2017;7(7).
121. Wu M, Hong G, Chen Y, Ye L, Zhang K, Cai K, et al. Personalized drug testing in a patient with non-small-cell lung cancer using cultured cancer cells from pleural effusion. *Journal of International Medical Research.* 2020;48(9):0300060520955058.
122. Andus I, Prall F, Linnebacher M, Linnebacher CS. Establishment, characterization, and drug screening of low-passage patient individual non-small cell lung cancer in vitro models including the rare pleomorphic subentity. *Front Oncol.* 2023;13:1089681.
123. Zhang J, Fujimoto J, Zhang J, Wedge DC, Song X, Zhang J, et al. Intratumor heterogeneity in localized lung adenocarcinomas delineated by multiregion sequencing. *Science.* 2014;346(6206):256-9.
124. Sun X-x, Yu Q. Intra-tumor heterogeneity of cancer cells and its implications for cancer treatment. *Acta Pharmacologica Sinica.* 2015;36(10):1219-27.
125. Han S, Liu Y, Cai SJ, Qian M, Ding J, Larion M, et al. IDH mutation in glioma: molecular mechanisms and potential therapeutic targets. *British Journal of Cancer.* 2020;122(11):1580-9.
126. Davis ME. Glioblastoma: Overview of Disease and Treatment. *Clin J Oncol Nurs.* 2016;20(5 Suppl):S2-8.
127. Miller JJ, Loebel F, Juratli TA, Tummala SS, Williams EA, Batchelor TT, et al. Accelerated progression of IDH mutant glioma after first recurrence. *Neuro Oncol.* 2019;21(5):669-77.
128. Dewdney B, Jenkins MR, Best SA, Freytag S, Prasad K, Holst J, et al. From signalling pathways to targeted therapies: unravelling glioblastoma's secrets and harnessing two decades of progress. *Signal Transduction and Targeted Therapy.* 2023;8(1):400.
129. Yang J, Xu J, Wang W, Zhang B, Yu X, Shi S. Epigenetic regulation in the tumor microenvironment: molecular mechanisms and therapeutic targets. *Signal Transduction and Targeted Therapy.* 2023;8(1):210.
130. Wu Q, Berglund AE, Etame AB. The Impact of Epigenetic Modifications on Adaptive Resistance Evolution in Glioblastoma. *Int J Mol Sci.* 2021;22(15).
131. McClellan BL, Haase S, Nunez FJ, Alghamri MS, Dabaja AA, Lowenstein PR, Castro MG. Impact of epigenetic reprogramming on antitumor immune responses in glioma. *J Clin Invest.* 2023;133(2).
132. Xie B, Peng F, He F, Cheng Y, Cheng J, Zhou Z, Mao W. DNA methylation influences the CTCF-modulated transcription of RASSF1A in lung cancer cells. *Cell Biol Int.* 2022;46(11):1900-14.
133. Cheng W, Jiang Y, Liu C, Shen O, Tang W, Wang X. Identification of aberrant promoter hypomethylation of HOXA10 in ovarian cancer. *J Cancer Res Clin Oncol.* 2010;136(8):1221-7.
134. Tawbi HA, Beumer JH, Tarhini AA, Moschos S, Buch SC, Egorin MJ, et al. Safety and efficacy of decitabine in combination with temozolomide in metastatic melanoma: a phase I/II study and pharmacokinetic analysis. *Ann Oncol.* 2013;24(4):1112-9.
135. Plumb JA, Strathdee G, Sludden J, Kaye SB, Brown R. Reversal of drug resistance in human tumor xenografts by 2'-deoxy-5-azacytidine-induced demethylation of the hMLH1 gene promoter. *Cancer Res.* 2000;60(21):6039-44.
136. Hu C, Liu X, Zeng Y, Liu J, Wu F. DNA methyltransferase inhibitors combination therapy for the treatment of solid tumor: mechanism and clinical application. *Clinical Epigenetics.* 2021;13(1):166.
137. Silva-Hurtado TJ, Inocencio JF, Yong RL. Emerging applications of hypomethylating agents in the treatment of glioblastoma (Review). *Mol Clin Oncol.* 2024;21(3):59.
138. Flotho C, Claus R, Batz C, Schneider M, Sandrock I, Ihde S, et al. The DNA methyltransferase inhibitors azacitidine, decitabine and zebularine exert differential effects on cancer gene expression in acute myeloid leukemia cells. *Leukemia.* 2009;23(6):1019-28.

References

139. Mehrjardi NZ, Hänggi D, Kahlert UD. Current biomarker-associated procedures of cancer modeling-a reference in the context of IDH1 mutant glioma. *Cell Death & Disease*. 2020;11(11):998.
140. M. P. Schilling SS, J. E. U. Gómez, A. A. Popova, P. A. Levkin and M. Reischl. Grid Screener: A Tool for Automated High-Throughput Screening on Biochemical and Biological Analysis Platforms. *IEEE Access*. 2021;9:166027-38.
141. Urrutia Gómez JE, Zhou M, Mandsberg NK, Serna JA, von Padberg J, Liu S, et al. Highly Parallel and High-Throughput Nanoliter-Scale Liquid, Cell, and Spheroid Manipulation on Droplet Microarray. *Advanced Functional Materials*.n/a(n/a):2410355.
142. Cui H, Sun X, Schilling M, Herold-Mende C, Reischl M, Levkin PA, et al. Repurposing FDA-Approved Drugs for Temozolomide-Resistant IDH1 Mutant Glioma Using High-Throughput Miniaturized Screening on Droplet Microarray Chip. *Advanced Healthcare Materials*. 2023;12(24):2300591.
143. Berghauer Pont LM, Spoor JK, Venkatesan S, Swagemakers S, Kloezezan JJ, Dirven CM, et al. The Bcl-2 inhibitor Obatoclox overcomes resistance to histone deacetylase inhibitors SAHA and LBH589 as radiosensitizers in patient-derived glioblastoma stem-like cells. *Genes Cancer*. 2014;5(11-12):445-59.
144. Administration' USFD. FDA approves dabrafenib with trametinib for pediatric patients with low-grade glioma with a BRAF V600E mutation 2023 [Available from: <https://www.fda.gov/drugs/resources-information-approved-drugs/fda-approves-dabrafenib-trametinib-pediatric-patients-low-grade-glioma-braf-v600e-mutation>].
145. Taiarol L, Bigogno C, Sesana S, Kravicz M, Viale F, Pozzi E, et al. Givinostat-Liposomes: Anti-Tumor Effect on 2D and 3D Glioblastoma Models and Pharmacokinetics. *Cancers (Basel)*. 2022;14(12).
146. Alonso M, Tamasdan C, Miller DC, Newcomb EW. Flavopiridol induces apoptosis in glioma cell lines independent of retinoblastoma and p53 tumor suppressor pathway alterations by a caspase-independent pathway. *Mol Cancer Ther*. 2003;2(2):139-50.
147. Akhavan D, Cloughesy TF, Mischel PS. mTOR signaling in glioblastoma: lessons learned from bench to bedside. *Neuro Oncol*. 2010;12(8):882-9.
148. Comprehensive genomic characterization defines human glioblastoma genes and core pathways. *Nature*. 2008;455(7216):1061-8.
149. Salphati L, Heffron TP, Aliche B, Nishimura M, Barck K, Carano RA, et al. Targeting the PI3K pathway in the brain--efficacy of a PI3K inhibitor optimized to cross the blood-brain barrier. *Clin Cancer Res*. 2012;18(22):6239-48.
150. Galanis E, Jaeckle KA, Maurer MJ, Reid JM, Ames MM, Hardwick JS, et al. Phase II trial of vorinostat in recurrent glioblastoma multiforme: a north central cancer treatment group study. *J Clin Oncol*. 2009;27(12):2052-8.
151. Wang XF, Zhao ZF, Chen MH, Yuan QH, Li YL, Jiang CL. Epirubicin inhibits growth and alters the malignant phenotype of the U-87 glioma cell line. *Mol Med Rep*. 2015;12(4):5917-23.
152. Yabasin IB, Ibrahim MM, Adam A, Wilfred S-A, Ziem JB, Gao P, et al. Anticancer effects of vecuronium bromide and cisatracurium besylate on lung cancer cells (A549), in vitro. *Biomedicine & Aging Pathology*. 2014;4(4):349-53.
153. Ali MA, Reis A, Ding LH, Story MD, Habib AA, Chattopadhyay A, Saha D. SNS-032 prevents hypoxia-mediated glioblastoma cell invasion by inhibiting hypoxia inducible factor-1alpha expression. *Int J Oncol*. 2009;34(4):1051-60.
154. Byth KF, Thomas A, Hughes G, Forder C, McGregor A, Geh C, et al. AZD5438, a potent oral inhibitor of cyclin-dependent kinases 1, 2, and 9, leads to pharmacodynamic changes and potent antitumor effects in human tumor xenografts. *Molecular Cancer Therapeutics*. 2009;8(7):1856-66.
155. Aazmi A, Zhang D, Mazzaglia C, Yu M, Wang Z, Yang H, et al. Biofabrication methods for reconstructing extracellular matrix mimetics. *Bioact Mater*. 2024;31:475-96.

References

156. Bouhlef W, Kui J, Bibette J, Bremond N. Encapsulation of Cells in a Collagen Matrix Surrounded by an Alginate Hydrogel Shell for 3D Cell Culture. *ACS Biomaterials Science & Engineering*. 2022;8(6):2700-8.
157. Guan X, Huang S. Advances in the application of 3D tumor models in precision oncology and drug screening. *Front Bioeng Biotechnol*. 2022;10:1021966.
158. Vu B, Souza GR, Dengjel J. Scaffold-free 3D cell culture of primary skin fibroblasts induces profound changes of the matrisome. *Matrix Biol Plus*. 2021;11:100066.
159. El-Sherbiny IM, Yacoub MH. Hydrogel scaffolds for tissue engineering: Progress and challenges. *Glob Cardiol Sci Pract*. 2013;2013(3):316-42.
160. Silva Garcia JM, Panitch A, Calve S. Functionalization of hyaluronic acid hydrogels with ECM-derived peptides to control myoblast behavior. *Acta Biomater*. 2019;84:169-79.
161. Almeida HV, Eswaramoorthy R, Cuniffe GM, Buckley CT, O'Brien FJ, Kelly DJ. Fibrin hydrogels functionalized with cartilage extracellular matrix and incorporating freshly isolated stromal cells as an injectable for cartilage regeneration. *Acta Biomater*. 2016;36:55-62.
162. Geckil H, Xu F, Zhang X, Moon S, Demirci U. Engineering hydrogels as extracellular matrix mimics. *Nanomedicine (Lond)*. 2010;5(3):469-84.
163. Valdoz JC, Johnson BC, Jacobs DJ, Franks NA, Dodson EL, Sanders C, et al. The ECM: To Scaffold, or Not to Scaffold, That Is the Question. *Int J Mol Sci*. 2021;22(23).
164. Li J, Mooney DJ. Designing hydrogels for controlled drug delivery. *Nature Reviews Materials*. 2016;1(12):16071.
165. Bertsch P, Diba M, Mooney DJ, Leeuwenburgh SCG. Self-Healing Injectable Hydrogels for Tissue Regeneration. *Chem Rev*. 2023;123(2):834-73.
166. Xu F, Dawson C, Lamb M, Mueller E, Stefanek E, Akbari M, Hoare T. Hydrogels for Tissue Engineering: Addressing Key Design Needs Toward Clinical Translation. *Front Bioeng Biotechnol*. 2022;10:849831.
167. Fang W, Yang M, Wang L, Li W, Liu M, Jin Y, et al. Hydrogels for 3D bioprinting in tissue engineering and regenerative medicine: Current progress and challenges. *Int J Bioprint*. 2023;9(5):759.
168. Unnikrishnan K, Thomas LV, Ram Kumar RM. Advancement of Scaffold-Based 3D Cellular Models in Cancer Tissue Engineering: An Update. *Front Oncol*. 2021;11:733652.
169. Wang Y, Jeon H. 3D cell cultures toward quantitative high-throughput drug screening. *Trends Pharmacol Sci*. 2022;43(7):569-81.
170. Aung A, Kumar V, Theprungsirikul J, Davey SK, Varghese S. An Engineered Tumor-on-a-Chip Device with Breast Cancer-Immune Cell Interactions for Assessing T-cell Recruitment. *Cancer Res*. 2020;80(2):263-75.
171. Dolznig H, Rupp C, Puri C, Haslinger C, Schweifer N, Wieser E, et al. Modeling colon adenocarcinomas in vitro a 3D co-culture system induces cancer-relevant pathways upon tumor cell and stromal fibroblast interaction. *Am J Pathol*. 2011;179(1):487-501.
172. Huang H, Yu Y, Hu Y, He X, Berk Usta O, Yarmush ML. Generation and manipulation of hydrogel microcapsules by droplet-based microfluidics for mammalian cell culture. *Lab Chip*. 2017;17(11):1913-32.
173. Jensen C, Teng Y. Is It Time to Start Transitioning From 2D to 3D Cell Culture? *Front Mol Biosci*. 2020;7:33.
174. Popova AA, Dietrich S, Huber W, Reischl M, Peravali R, Levkin PA. Miniaturized Drug Sensitivity and Resistance Test on Patient-Derived Cells Using Droplet-Microarray. *SLAS TECHNOLOGY: Translating Life Sciences Innovation*. 2021;26(3):274-86.
175. Anna AP, Markus R, Daniel K, Haijun C, Timo A, Pavel AL. Simple assessment of viability in 2D and 3D cell microarrays using single step digital imaging. *SLAS Technology*. 2022;27(1):44-53.
176. Popova AA, Tronser T, Demir K, Haitz P, Kuodyte K, Starkuviene V, et al. Facile One Step Formation and Screening of Tumor Spheroids Using Droplet-Microarray Platform. *Small*. 2019;15(25):1901299.

References

177. Cui H, Wang X, Wesslowski J, Tronser T, Rosenbauer J, Schug A, et al. Assembly of Multi-Spheroid Cellular Architectures by Programmable Droplet Merging. *Advanced Materials*. 2021;33(4):2006434.
178. Cui H, Tronser T, Wang X, Wesslowski J, Davidson G, Popova AA, Levkin PA. High-throughput formation of miniaturized cocultures of 2D cell monolayers and 3D cell spheroids using droplet microarray. *Droplet*. 2023;2(1):e39.

Appendix

Number	Name	Pathway	M.w.
1	Veliparib (ABT-888)	DNA Damage/DNA Repair	244.29
2	Selumetinib (AZD6244)	MAPK	457.68
3	Cediranib (AZD2171)	Protein Tyrosine Kinase	450.51
4	Dasatinib (BMS-354825)	Angiogenesis	488.01
5	Gefitinib (ZD1839)	Protein Tyrosine Kinase	446.90
6	Imatinib (STI571) Mesylate	Protein Tyrosine Kinase	589.71
7	Lapatinib (GW-572016) Ditosylate	Protein Tyrosine Kinase	925.46
8	Lenalidomide (CC-5013)	Ubiquitin	259.26
9	Pazopanib HCl (GW786034 HCl)	Protein Tyrosine Kinase	473.98
10	Rapamycin (AY-22989)	PI3K/Akt/mTOR	914.18
11	Sorafenib (BAY 43-9006) tosylate	MAPK	637.03
12	Vorinostat (SAHA)	Epigenetics	264.30
13	Entinostat (MS-275)	Epigenetics	376.41
14	Enzastaurin (LY317615)	TGF-beta/Smad	515.61
15	Obatoclox Mesylate (GX15-070)	Apoptosis	413.49
16	Olaparib (AZD2281)	DNA Damage/DNA Repair	434.46
17	Vismodegib (GDC-0449)	Stem Cells & Wnt	421.30
18	Iniparib (BSI-201)	DNA Damage/DNA Repair	292.03
19	Vatalanib (PTK787) 2HCl	Protein Tyrosine Kinase	419.73
20	OSU-03012 (AR-12)	PI3K/Akt/mTOR	460.45
21	Everolimus (RAD001)	PI3K/Akt/mTOR	958.22
22	Ivacaftor (VX-770)	Transmembrane Transporters	392.49
23	SNS-032 (BMS-387032)	Cell Cycle	380.53
24	Roscovitine (CYC202)	Cell Cycle	354.45
25	Capecitabine (RO 09-1978)	DNA Damage/DNA Repair	359.35
26	Ritonavir (ABT-538)	Proteases	720.94
27	Aprepitant (MK-0869)	Neuronal Signaling	534.43
28	Thalidomide (K17)	Ubiquitin	258.23
29	Cladribine (RWJ 26251)	Neuronal Signaling	285.69
30	Melatonin (NSC 113928)	GPCR & G Protein	232.28
31	Methotrexate (CL-14377)	Metabolism	454.44
32	Bendamustine (SDX105) HCl	DNA Damage/DNA Repair	394.72
33	Epirubicin (IMI 28) HCl	DNA Damage/DNA Repair	579.98
34	Flavopiridol (L86-8275)	Cell Cycle	401.84

Appendix

35	Topotecan (NSC609699) HCl	DNA Damage/DNA Repair	457.91
36	Temozolomide (CCRG 81045)	DNA Damage/DNA Repair	194.15
37	Tamoxifen (ICI 46474)	Angiogenesis	371.51
38	Vincristine (NSC-67574) sulfate	Cytoskeletal Signaling	923.04
39	Agomelatine (S20098)	Neuronal Signaling	243.30
40	Latrepirdine 2HCl	Neuronal Signaling	392.37
41	Dienogest	Endocrinology & Hormones	311.42
42	Nepafenac	Neuronal Signaling	254.28
43	Rufinamide	Transmembrane Transporters	238.19
44	Ramelteon	GPCR & G Protein	259.34
45	Celecoxib (SC 58635)	Neuronal Signaling	381.37
46	Asenapine maleate	Neuronal Signaling	401.84
47	Mercaptopurine (6-MP)	DNA Damage/DNA Repair	152.18
48	Dexamethasone (MK-125)	Immunology & Inflammation	392.46
49	Edaravone	ER stress & UPR	174.20
50	Etodolac	Neuronal Signaling	287.35
51	Etomidate	Neuronal Signaling	244.29
52	Felbamate	Neuronal Signaling	238.24
53	Fluconazole (UK 49858)	Metabolism	306.27
54	Fluoxetine (Lilly 110140) HCl	Neuronal Signaling	345.79
55	Fluvoxamine (DU-23000) maleate	Neuronal Signaling	434.41
56	Gatifloxacin	DNA Damage/DNA Repair	375.39
57	Genistein (NPI 031L)	Protein Tyrosine Kinase	270.24
58	Ivermectin (MK-933)	Transmembrane Transporters	875.09
59	Levetiracetam (UCB-L059)	Transmembrane Transporters	170.21
60	Lidocaine	Neuronal Signaling	234.34
61	Loratadine (SCH29851)	Neuronal Signaling	382.88
62	Patupilone (Epothilone B)	Cytoskeletal Signaling	507.68
63	Lopinavir (ABT-378)	Proteases	628.80
64	Mosapride Citrate	Neuronal Signaling	614.02
65	Ondansetron HCl	Neuronal Signaling	329.82
66	Oxcarbazepine	Transmembrane Transporters	252.27
67	Pizotifen Malate	Neuronal Signaling	429.53
68	Resveratrol (SRT501)	Autophagy	228.24
69	Rocuronium Bromide	Neuronal Signaling	609.68
70	Stavudine (d4T)	Microbiology	224.21
71	Tenofovir	Microbiology	287.21
72	Vecuronium Bromide	Neuronal Signaling	637.73
73	Rolipram (ZK-62711)	Metabolism	275.34
74	Sumatriptan Succinate	Neuronal Signaling	413.49
75	Tizanidine HCl	Neuronal Signaling	290.17
76	Topiramate	Metabolism	339.36
77	Venlafaxine HCl	Neuronal Signaling	313.86

Appendix

78	Voriconazole (UK-109496)	Metabolism	349.31
79	Ziprasidone HCl	Neuronal Signaling	449.40
80	Zonisamide	Transmembrane Transporters	212.23
81	Atazanavir (BMS-232632) Sulfate	Proteases	802.93
82	Neflamapimod (VX-745)	MAPK	436.26
83	Iloperidone	Neuronal Signaling	426.48
84	AEE788 (NVP-AEE788)	Protein Tyrosine Kinase	440.58
85	Naratriptan HCl	Neuronal Signaling	371.93
86	Pralatrexate (NSC 754230)	Metabolism	477.47
87	Aztreonam	Microbiology	435.43
88	Pomalidomide (CC-4047)	Ubiquitin	273.24
89	Sulfasalazine (NSC 667219)	Immunology & Inflammation	398.39
90	Candesartan (CV-11974)	GPCR & G Protein	440.45
91	Rizatriptan Benzoate	Neuronal Signaling	391.47
92	Pyridostigmine Bromide	Neuronal Signaling	261.12
93	Riluzole (PK 26124)	Transmembrane Transporters	234.20
94	Prednisone (NSC-10023)	Endocrinology & Hormones	358.43
95	Acetylcysteine (N-acetylcysteine)	Apoptosis	163.19
96	Naproxen Sodium	Neuronal Signaling	252.24
97	Ibuprofen (NSC 256857)	Neuronal Signaling	206.28
98	Amprenavir (VX-478)	Proteases	505.63
99	Ketoprofen	Neuronal Signaling	254.28
100	Ketorolac	Neuronal Signaling	255.27
101	Adenosine	GPCR & G Protein	267.24
102	Zolmitriptan	Neuronal Signaling	287.36
103	Tretinoin (NSC 122758)	Metabolism	300.40
104	Phenylbutazone	Immunology & Inflammation	308.37
105	Flucytosine	Microbiology	129.09
106	Flurbiprofen	Immunology & Inflammation	244.26
107	Disulfiram (NSC 190940)	Metabolism	296.54
108	Ipratropium Bromide	Neuronal Signaling	412.37
109	Busulfan (NSC-750)	DNA Damage/DNA Repair	246.30
110	Carbamazepine	Transmembrane Transporters	236.27
111	Didanosine	Microbiology	236.23
112	Emtricitabine (BW 1592)	Microbiology	247.25
113	Progesterone (NSC 9704)	Endocrinology & Hormones	314.46
114	Lamivudine (BCH-189)	Microbiology	229.26
115	Piroxicam	Neuronal Signaling	331.35
116	Glyburide (Glibenclamide)	Transmembrane Transporters	494.00
117	Indomethacin (NSC-77541)	Neuronal Signaling	357.79
118	Terbinafine	Microbiology	291.43
119	Methylprednisolone (NSC-19987)	Endocrinology & Hormones	374.47
120	Meloxicam	Neuronal Signaling	351.40

Appendix

121	Methocarbamol	Metabolism	241.24
122	Prednisolone (NSC-9900)	Endocrinology & Hormones	360.44
123	Nevirapine (NSC 641530)	Microbiology	266.30
124	Nimodipine	Transmembrane Transporters	418.44
125	Oxybutynin	Neuronal Signaling	357.49
126	Suprofen	Neuronal Signaling	260.31
127	Pyrazinamide	Microbiology	123.11
128	Rifampin (NSC-113926)	DNA Damage/DNA Repair	822.94
129	Ethionamide	Microbiology	166.24
130	Tetrabenazine (Xenazine)	Neuronal Signaling	317.42
131	Simvastatin (MK 733)	Metabolism	418.57
132	Acetylcholine Chloride	Neuronal Signaling	181.66
133	Aciclovir (BW 248U)	Microbiology	225.20
134	Atracurium Besylate	Neuronal Signaling	1243.48
135	Lomustine	DNA Damage/DNA Repair	233.70
136	Cimetidine	Neuronal Signaling	252.34
137	Daidzein	Metabolism	254.24
138	Diethylstilbestrol	Endocrinology & Hormones	268.35
139	Dapoxetine HCl	Neuronal Signaling	341.87
140	Ganciclovir (BW 759)	Microbiology	255.23
141	Felodipine	Transmembrane Transporters	384.25
142	Hydroxyurea (NSC-32065)	DNA Damage/DNA Repair	76.05
143	Tropisetron HCl	Neuronal Signaling	320.81
144	Vitamin B12	Metabolism	1355.37
145	Diclofenac Sodium	Neuronal Signaling	318.13
146	Metronidazole	DNA Damage/DNA Repair	171.15
147	Tropicamide	Neuronal Signaling	284.35
148	Pregnenolone	Endocrinology & Hormones	316.48
149	Sulfamethoxazole	Microbiology	253.28
150	Haloperidol	Neuronal Signaling	375.86
151	Isoniazid	Metabolism	137.14
152	Levofloxacin	DNA Damage/DNA Repair	361.37
153	Metformin HCl	Metabolism	165.62
154	Miconazole Nitrate	Microbiology	479.14
155	Tolfenamic Acid	Neuronal Signaling	261.70
156	Pranoprofen	Neuronal Signaling	255.27
157	Primidone	Transmembrane Transporters	218.25
158	Tamoxifen (ICI 46474) Citrate	Endocrinology & Hormones	563.64
159	Aripiprazole	Neuronal Signaling	448.39
160	Methscopolamine	Neuronal Signaling	398.29
161	Pyrimethamine	Metabolism	248.71
162	Sulindac	Neuronal Signaling	356.41
163	Pramipexole 2HCl Monohydrate	Neuronal Signaling	302.26

Appendix

164	Mirtazapine	Neuronal Signaling	265.35
165	Urapidil HCl	Neuronal Signaling	423.94
166	Candesartan Cilexetil	GPCR & G Protein	610.66
167	Nimesulide	Neuronal Signaling	308.31
168	Dyclonine HCl	Transmembrane Transporters	325.87
169	Memantine HCl	Neuronal Signaling	215.76
170	Cyproheptadine HCl	Neuronal Signaling	323.86
171	Orphenadrine Citrate	Neuronal Signaling	461.50
172	Lovastatin (MK-803)	Metabolism	404.54
173	Atorvastatin Calcium	Metabolism	1155.34
174	Adiphenine HCl	Neuronal Signaling	347.88
175	Duloxetine HCl	Neuronal Signaling	333.88
176	Rivastigmine Tartrate	Neuronal Signaling	400.42
177	Dexmedetomidine HCl	Neuronal Signaling	236.74
178	Almotriptan Malate	Neuronal Signaling	469.55
179	Rasagiline Mesylate	Metabolism	267.34
180	Flunixin Meglumin	Neuronal Signaling	491.46
181	Lapatinib (GW-572016)	Protein Tyrosine Kinase	581.06
182	Cisatracurium Besylate	Neuronal Signaling	1243.48
183	Conivaptan HCl	GPCR & G Protein	535.04
184	Probucol	Metabolism	516.84
185	Bazedoxifene (WAY-140424) HCl	Endocrinology & Hormones	507.06
186	Atropine sulfate monohydrate	Neuronal Signaling	694.83
187	LY2886721	Neuronal Signaling	390.41
188	Bazedoxifene (TSE-424) acetate	Endocrinology & Hormones	530.65
189	Givinostat (ITF2357)	Cytoskeletal Signaling	475.97
190	Irinotecan (CPT-11) HCl Trihydrate	DNA Damage/DNA Repair	677.18
191	SB590885	MAPK	453.54
192	PF-3716556	Transmembrane Transporters	394.47
193	Buparlisib (BKM120)	PI3K/Akt/mTOR	410.39
194	Cyclosporin A (NSC 290193)	Immunology & Inflammation	1202.61
195	Cytisine	Neuronal Signaling	190.24
196	Honokiol (NSC 293100)	PI3K/Akt/mTOR	266.33
197	Puerarin	Neuronal Signaling	416.38
198	Rutaecarpine	Neuronal Signaling	287.32
199	Rutin	Immunology & Inflammation	610.52
200	Salicin	Neuronal Signaling	286.28
201	Vanillylacetone	NF-κB	194.23
202	Paeoniflorin (NSC 178886)	Immunology & Inflammation	480.46
203	Amantadine HCl	Neuronal Signaling	187.70
204	Amfebutamone (Bupropion) HCl	Neuronal Signaling	276.20
205	Bupivacaine HCl	Transmembrane Transporters	324.89
206	Bethanechol chloride	Neuronal Signaling	196.68

Appendix

207	Clonidine HCl	Neuronal Signaling	266.50
208	Clozapine	Neuronal Signaling	326.82
209	Pramipexole	Neuronal Signaling	211.33
210	Domperidone	Neuronal Signaling	425.91
211	Estriol	Endocrinology & Hormones	288.39
212	Gallamine Triethiodide	Neuronal Signaling	891.53
213	Olanzapine	Neuronal Signaling	312.44
214	Pancuronium dibromide	Neuronal Signaling	732.67
215	Ribavirin (ICN-1229)	Microbiology	244.21
216	Scopolamine (LSM-4015) HBr	Neuronal Signaling	384.26
217	Phenytoin Sodium	Transmembrane Transporters	274.25
218	Phenytoin	Transmembrane Transporters	252.27
219	Asaraldehyde	Neuronal Signaling	196.20
220	Clomipramine HCl	Neuronal Signaling	351.31
221	Tiotropium Bromide hydrate	Neuronal Signaling	490.43
222	Trospium chloride	Neuronal Signaling	427.96
223	5-Aminolevulinic acid HCl	Others	167.59
224	Rosiglitazone (BRL 49653)	Metabolism	357.43
225	Amoxicillin Sodium	Microbiology	387.39
226	Prednisolone Acetate	Endocrinology & Hormones	402.48
227	Phenacetin	Neuronal Signaling	179.22
228	Zidovudine	Microbiology	267.24
229	Dimethyl Fumarate	Immunology & Inflammation	144.13
230	Acemetacin	Neuronal Signaling	415.82
231	Arecoline HBr	Neuronal Signaling	236.11
232	AZD5438	Cell Cycle	371.46
233	OSI-027	PI3K/Akt/mTOR	406.44
234	PNU-120596	Neuronal Signaling	311.72
235	URB597	Metabolism	338.40
236	NPS-2143	GPCR & G Protein	408.92
237	WAY-100635 Maleate	Neuronal Signaling	538.64
238	Trametinib (GSK1120212)	MAPK	615.39
239	BRL-15572 Dihydrochloride	Neuronal Signaling	479.87
240	Flavopiridol (L86-8275) HCl	Cell Cycle	438.30
241	ADX-47273	Neuronal Signaling	369.36
242	Nepicastat (SYN-117) HCl	Metabolism	331.81
243	RS-127445	Neuronal Signaling	281.33
244	ZM 336372	MAPK	389.45
245	Dacomitinib (PF-00299804)	Protein Tyrosine Kinase	469.94
246	Alectinib (CH5424802)	Protein Tyrosine Kinase	482.62
247	Nocodazole (R17934)	Cytoskeletal Signaling	301.32
248	PF-5274857	Stem Cells & Wnt	436.96
249	TAK-285	Protein Tyrosine Kinase	547.96

Appendix

250	Laquinimod	Immunology & Inflammation	356.80
251	WP1066	JAK/STAT	356.22
252	Lonafarnib (SCH66336)	Metabolism	638.82
253	JNJ-1661010	Metabolism	365.45
254	SB269970 HCl	Neuronal Signaling	388.95
255	BRL-54443	Neuronal Signaling	230.31
256	SB 271046 hydrochloride	Neuronal Signaling	488.45
257	VUF 10166	Neuronal Signaling	262.74
258	Prucalopride	Neuronal Signaling	367.87
259	VU 0361737	Neuronal Signaling	262.69
260	SB742457	Neuronal Signaling	353.44
261	Lumiracoxib	Neuronal Signaling	293.72
262	BAY 11-7082	NF-κB	207.25
263	Icotinib (BPI-2009H)	Protein Tyrosine Kinase	391.42
264	Paroxetine HCl	Neuronal Signaling	365.83
265	Zaltoprofen	Neuronal Signaling	298.36
266	Pazopanib	Protein Tyrosine Kinase	437.52
267	Aspirin (NSC 27223)	Metabolism	180.16
268	Niflumic acid	Neuronal Signaling	282.22
269	Rimonabant (SR141716)	GPCR & G Protein	463.79
270	Cabazitaxel (XRP6258)	Cytoskeletal Signaling	835.93
271	Bufexamac	Neuronal Signaling	223.27
272	Lamotrigine	Transmembrane Transporters	256.09
273	Rofecoxib	Neuronal Signaling	314.36
274	Otilonium Bromide	Neuronal Signaling	563.57
275	Alverine Citrate	Neuronal Signaling	473.56
276	Diclofenac Diethylamine	Neuronal Signaling	369.29
277	Oxybutynin hydrochloride	Neuronal Signaling	393.95
278	Dexamethasone Acetate	Immunology & Inflammation	434.50
279	Sulfamethazine	Microbiology	278.33
280	Milnacipran HCl	Neuronal Signaling	282.81
281	Darifenacin HBr	Neuronal Signaling	507.46
282	Benztropine mesylate	Neuronal Signaling	403.53
283	Antipyrine	Neuronal Signaling	188.23
284	Atomoxetine HCl	Neuronal Signaling	291.82
285	Eletriptan HBr	Neuronal Signaling	463.43
286	Amitriptyline HCl	Neuronal Signaling	313.86
287	Ropinirole HCl	Neuronal Signaling	296.84
288	Azacyclonol	Neuronal Signaling	267.37
289	Triflusal	Immunology & Inflammation	248.16
290	Trifluoperazine 2HCl	Neuronal Signaling	480.42
291	Catharanthine	Neuronal Signaling	336.43
292	Tacrine hydrochloride hydrate	Neuronal Signaling	198.26(free bases)

Appendix

293	Cefepime Dihydrochloride Monohydrate	Microbiology	571.50
294	Methacholine chloride	Neuronal Signaling	195.69
295	Nortriptyline hydrochloride	Autophagy	299.84
296	Benactyzine hydrochloride	Neuronal Signaling	363.88
297	Sarpogrelate hydrochloride	Neuronal Signaling	465.97
298	Flibanserin	Neuronal Signaling	390.40
299	Ramosetron Hydrochloride	Neuronal Signaling	315.80
300	Metaxalone	Others	221.25
301	Umeclidinium bromide	Neuronal Signaling	508.49
302	Picoside II	Immunology & Inflammation	512.46
303	Palmitine	Neuronal Signaling	352.40
304	Glabridin	Metabolism	324.37
305	Carvacrol	Neuronal Signaling	150.22
306	Dehydroevodiamine	Immunology & Inflammation	301.34
307	Harmine hydrochloride	Cell Cycle	248.71
308	Dehydroevodiamine hydrochloride	Neuronal Signaling	337.80
309	Loganin	Neuronal Signaling	390.38
310	Galanthamine	Neuronal Signaling	287.35
311	Guaiaacol	NF-κB	124.14
312	Jatrorrhizine	Neuronal Signaling	338.38
313	Hederagenin	Immunology & Inflammation	472.70
314	Lycorine	Neuronal Signaling	287.31
315	Isoimperatorin	Neuronal Signaling	270.28
316	(-)-Epicatechin gallate	Immunology & Inflammation	442.37
317	Ginsenoside Rd	Immunology & Inflammation	947.15
318	Valproic acid (VPA)	Epigenetics	144.21
319	L-Cycloserine	Metabolism	102.09
320	Higenamine hydrochloride	Neuronal Signaling	307.77
321	Veratric acid	Immunology & Inflammation	182.17
322	(+)-Catechin hydrate	Immunology & Inflammation	290.27
323	Ampiroxicam	Neuronal Signaling	447.46
324	Hyoscyamine	Neuronal Signaling	289.37
325	Tolcapone	Metabolism	273.24
326	Probenecid	Transmembrane Transporters	285.36
327	Procaine HCl	Transmembrane Transporters	272.77
328	Homatropine Methylbromide	Neuronal Signaling	370.28
329	Homatropine Bromide	Neuronal Signaling	356.25
330	Hydroxyzine 2HCl	Neuronal Signaling	447.83
331	Acridinium Bromide	Neuronal Signaling	564.55
332	Diphenamil Methylsulfate	Neuronal Signaling	389.51
333	Valdecoxib	Neuronal Signaling	314.36
334	Nabumetone	Neuronal Signaling	228.29
335	Sertraline HCl	Neuronal Signaling	342.69

Appendix

336	Escitalopram Oxalate	Neuronal Signaling	414.43
337	Decamethonium Bromide	Neuronal Signaling	418.29
338	Propranolol HCl	GPCR & G Protein	295.80
339	Mefenamic Acid	Neuronal Signaling	241.29
340	Loxapine Succinate	Neuronal Signaling	445.90
341	Droperidol	Neuronal Signaling	379.43
342	Desvenlafaxine Succinate hydrate	Neuronal Signaling	399.48
343	Desvenlafaxine	Neuronal Signaling	263.38
344	Sodium Phenylbutyrate	DNA Damage/DNA Repair	187.19
345	Carprofen	Neuronal Signaling	273.71
346	Pentoxifyverine Citrate	Neuronal Signaling	525.59
347	Amfenac Sodium Monohydrate	Neuronal Signaling	295.27
348	Chlorzoxazone	Metabolism	169.57
349	Benzethonium Chloride	Neuronal Signaling	448.08
350	Choline Chloride	Neuronal Signaling	139.62
351	Trometamol	Neuronal Signaling	121.14
352	Mezlocillin Sodium	Microbiology	561.56
353	Nicardipine HCl	Transmembrane Transporters	515.99
354	Sasapyrine	Immunology & Inflammation	258.23
355	Cinchophen	Others	249.26
356	Azaperone	Neuronal Signaling	327.40
357	Piperacillin Sodium	Microbiology	539.54
358	Oxaprozin	Metabolism	293.32
359	Pilocarpine HCl	Neuronal Signaling	244.72
360	Doxylamine Succinate	Neuronal Signaling	388.46
361	Serotonin HCl	Neuronal Signaling	212.68
362	Prucalopride Succinate	Neuronal Signaling	485.96
363	Bromfenac Sodium	Neuronal Signaling	356.15
364	Flopropione	Neuronal Signaling	182.17
365	Sulfamethoxypyridazine	Microbiology	280.30
366	Buspirone HCl	Neuronal Signaling	421.96
367	Vilazodone HCl	Neuronal Signaling	477.99
368	Vinorelbine ditartrate (KW-2307)	Cytoskeletal Signaling	1079.11
369	Rotigotine	Neuronal Signaling	315.47
370	Cyclobenzaprine HCl	Neuronal Signaling	311.85
371	Chloroambucil	DNA Damage/DNA Repair	304.21
372	Diphenidol HCl	Neuronal Signaling	345.91
373	Meclofenamate Sodium	Neuronal Signaling	318.13
374	Tacrine HCl	Neuronal Signaling	234.72
375	Imipramine HCl	Neuronal Signaling	316.87
376	Fosfomycin Tromethamine	Others	259.19
377	Bephenium Hydroxynaphthoate	Neuronal Signaling	443.53
378	Trimipramine Maleate	Others	410.51

Appendix

379	Mefloquine HCl	Microbiology	414.77
380	Nitenpyram	Neuronal Signaling	270.72
381	Vinblastine (NSC-49842) sulfate	Cytoskeletal Signaling	909.05
382	Acetazolamide	Metabolism	222.25
383	4-Aminoantipyrine	Immunology & Inflammation	203.24
384	Cefotaxime sodium	Microbiology	477.45
385	Fenbufen	Neuronal Signaling	254.28
386	Salicylic acid	Neuronal Signaling	138.12
387	Trihexyphenidyl hydrochloride	Neuronal Signaling	337.93
388	Clioquinol	Microbiology	305.50
389	Diflunisal	Neuronal Signaling	250.20
390	Dapson	Microbiology	248.30
391	Itopride hydrochloride	Neuronal Signaling	394.89
392	Methylbenactyzine Bromide	Neuronal Signaling	422.36
393	Ethosuximide	Transmembrane Transporters	141.17
394	(+/-)-Sulfinpyrazone	Neuronal Signaling	404.48
395	Cyproheptadine hydrochloride sesquihydrate	Neuronal Signaling	350.88
396	Dantrolene sodium hemiheptahydrate	Transmembrane Transporters	399.29
397	Etoricoxib	Neuronal Signaling	358.84
398	Sulpiride	Neuronal Signaling	341.43
399	Parecoxib	Neuronal Signaling	370.42
400	Glycopyrrolate	Neuronal Signaling	398.33
401	Tiagabine hydrochloride	Neuronal Signaling	412.01
402	Lidocaine hydrochloride	Angiogenesis	270.80
403	Efavirenz	Microbiology	315.67
404	Vitamin E	Neuronal Signaling	430.71
405	Rivastigmine	Neuronal Signaling	250.34
406	Oxybenzone	Others	228.24
407	Guanfacine Hydrochloride	Neuronal Signaling	282.55
408	Acetylcholine iodide	Neuronal Signaling	273.11
409	Perphenazine	Neuronal Signaling	403.97
410	MPTP hydrochloride	Neuronal Signaling	209.72
411	Ondansetron Hydrochloride Dihydrate	Neuronal Signaling	365.85
412	Citalopram HBr	Neuronal Signaling	405.30
413	Cisapride hydrate	Neuronal Signaling	483.96
414	Syringaldehyde	Immunology & Inflammation	182.17
415	Harmaline	Neuronal Signaling	214.26
416	5-methoxyflavone	DNA Damage/DNA Repair	252.26
417	1-Naphthyl acetate	Neuronal Signaling	186.21
418	Atenolol	Neuronal Signaling	266.34
419	Propantheline bromide	Neuronal Signaling	448.39
420	Acotiamide hydrochloride	Neuronal Signaling	541.06
421	Mosapride	Neuronal Signaling	421.89

Appendix

422	Perospirone hydrochloride	Neuronal Signaling	463.04
423	Propiverine hydrochloride	Transmembrane Transporters	403.94
424	Nanofin	Neuronal Signaling	113.20
425	Fingolimod (FTY720) HCl	GPCR & G Protein	343.90
426	Indometacin Sodium	Immunology & Inflammation	433.82
427	Indobufen	Immunology & Inflammation	295.33
428	Granisetron	Neuronal Signaling	312.41
429	Metadoxine	Neuronal Signaling	298.29
430	Pramipexole dihydrochloride	Neuronal Signaling	284.25
431	Duloxetine	Neuronal Signaling	297.41
432	Donepezil	Neuronal Signaling	379.49
433	Acotiamide	Neuronal Signaling	450.55
434	Pralidoxime Iodide	Neuronal Signaling	264.06
435	Tetrahydroberberine	Neuronal Signaling	339.39
436	Naproxen	Immunology & Inflammation	230.26
437	Diaveridine	Metabolism	260.29
438	Abacavir (1592U89)	Microbiology	286.33
439	Adrafinil	Others	289.35
440	Solifenacin (YM905)	Neuronal Signaling	362.46
441	Paroxetine mesylate	Neuronal Signaling	425.47
442	Cisapride (R 51619)	Neuronal Signaling	465.95
443	Revefenacin	Neuronal Signaling	597.75
444	J147	Neuronal Signaling	350.33
445	Amoxicillin trihydrate	Microbiology	419.45
446	Propyphenazone (4-Isopropylantipyrine)	Immunology & Inflammation	230.31
447	Dolasetron	Neuronal Signaling	324.37
448	Erucic acid	PI3K/Akt/mTOR	338.57
449	Imidafenacin	GPCR & G Protein	319.40
450	Nefazodone hydrochloride	Neuronal Signaling	506.47
451	Tegaserod Maleate	Neuronal Signaling	417.46
452	Propylparaben	Microbiology	180.20
453	Parecoxib Sodium	Immunology & Inflammation	392.40
454	Carbaryl	Neuronal Signaling	201.22
455	Promazine hydrochloride	Neuronal Signaling	320.88
456	AS057278	Neuronal Signaling	126.11
457	Ferulic acid methyl ester	Immunology & Inflammation	208.21
458	Nafronyl oxalate salt	Neuronal Signaling	473.56
459	Clidinium Bromide	Neuronal Signaling	432.35
460	Molindone hydrochloride	Neuronal Signaling	312.83
461	Tribenzagan Hydrochloride	Others	424.92
462	Desipramine Hydrochloride	Neuronal Signaling	302.84
463	Atropine sulfate	Neuronal Signaling	676.82
464	Ethyl (triphenylphosphoranylidene) acetate	Neuronal Signaling	348.37

Appendix

465	Phenidone	Immunology & Inflammation	162.19
466	Tropisetron	Neuronal Signaling	284.35
467	6-Paradol	Immunology & Inflammation	278.39
468	Thioridazine hydrochloride	Neuronal Signaling	407.04
469	Trimethadione	Transmembrane Transporters	143.14
470	3-Carene	Immunology & Inflammation	136.23
471	Hippuric acid	Others	179.17
472	Venlafaxine	Neuronal Signaling	277.40
473	Levomilnacipran Hydrochloride	Neuronal Signaling	282.81
474	Ketorolac tromethamine salt	Immunology & Inflammation	376.40
475	Scopolamine N-Oxide Hydrobromide Monohydrate	Metabolism	418.28
476	Deracoxib	Immunology & Inflammation	397.37
477	Lurasidone	Neuronal Signaling	492.68
478	Abemaciclib (LY2835219)	Cell Cycle	506.59
479	Palonosetron	Neuronal Signaling	296.41
480	Quetiapine	Neuronal Signaling	383.51
481	Morantel tartrate	Neuronal Signaling	370.42
482	Chlorpromazine	Neuronal Signaling	318.86
483	Alfuzosin	Neuronal Signaling	389.45
484	N-Acetylcysteine amide	Immunology & Inflammation	162.21
485	Cinitapride Hydrogen Tartrate	Neuronal Signaling	552.57
486	Frovatriptan Succinate	Neuronal Signaling	361.39
487	Trazodone	Neuronal Signaling	371.86
488	Vilazodone	Neuronal Signaling	441.52
489	Metoclopramide	Neuronal Signaling	299.80
490	Scopolamine HBr trihydrate	Neuronal Signaling	438.31
491	Edrophonium chloride	Metabolism	201.69
492	AK 7	Epigenetics	437.35
493	KHS101 hydrochloride	Cytoskeletal Signaling	375.92
494	Cyclopentolate Hydrochloride	Neuronal Signaling	327.85
495	PNU 282987 HCl	Metabolism	301.21
496	BQCA	Metabolism	309.32
497	Fingolimod	Neuronal Signaling	307.47
498	Diclofenac acid	Immunology & Inflammation	296.15
499	Rutin hydrate	Others	610.52
500	5-Methoxytryptamine	Neuronal Signaling	190.24
501	Azeliragon (TTP488)	Others	532.12
502	JNJ 63533054	GPCR & G Protein	316.78
503	Cevimeline HCl hemihydrate	Metabolism	244.78
504	Delavirdine mesylate	Microbiology	552.67
505	Flurbiprofen Axetil	Immunology & Inflammation	330.35
506	Thonzylamine	Neuronal Signaling	286.37
507	RG-7112	Apoptosis	726.28

Appendix

508	Epoxomicin (BU-4061T)	Proteases	554.72
509	(+)-JQ1	Epigenetics	456.99
510	TIC10 Analogue	PI3K/Akt/mTOR	386.49
511	Siponimod (BAF312)	GPCR & G Protein	516.60
512	RG2833 (RGFP109)	Epigenetics	339.43
513	Q-VD-Oph	Apoptosis	513.49
514	SH-4-54	JAK/STAT	610.59
515	URMC-099	MAPK	421.54
516	K02288	TGF-beta/Smad	352.38
517	LY2119620	Neuronal Signaling	437.94
518	Sorafenib (BAY 43-9006)	MAPK	464.82
519	SB-3CT	Proteases	306.40
520	Ribociclib (LEE011)	Cell Cycle	434.54
521	VER-49009	Cytoskeletal Signaling	387.82
522	SB-334867	GPCR & G Protein	319.32
523	PX-478 2HCl	Angiogenesis	394.12
524	Liproxstatin-1	Metabolism	340.85
525	BMH-21	DNA Damage/DNA Repair	360.41
526	BLZ945	Protein Tyrosine Kinase	398.48
527	SB239063	MAPK	368.40
528	VER155008	Cytoskeletal Signaling	556.40
529	Sunitinib (SU11248)	Protein Tyrosine Kinase	398.47
530	Erlotinib (OSI-774)	Protein Tyrosine Kinase	393.44
531	SRT2104 (GSK2245840)	DNA Damage/DNA Repair	516.64
532	GNE-317	PI3K/Akt/mTOR	414.48
533	Pexidartinib (PLX3397)	Protein Tyrosine Kinase	417.81
534	SC79	PI3K/Akt/mTOR	364.78
535	Xanthohumol	Metabolism	354.40
536	BMS202 (PD-1/PD-L1 inhibitor 2)	Immunology & Inflammation	419.52
537	NCT-501	Metabolism	416.52
538	Ozanimod (RPC1063)	GPCR & G Protein	404.46
539	SIS3 HCl	TGF-beta/Smad	489.99
540	TIC10 (ONC201)	PI3K/Akt/mTOR	386.49
541	Zorifertinib (AZD3759)	Protein Tyrosine Kinase	459.90
542	SKF96365	Transmembrane Transporters	402.91
543	PRX-08066 Maleic acid	Neuronal Signaling	517.96
544	Necrostatin-1	Apoptosis	259.33
545	Paxalisib (GDC-0084)	PI3K/Akt/mTOR	382.42
546	Pimavanserin tartrate	GPCR & G Protein	1005.20
547	FPS-ZM1	Neuronal Signaling	327.85
548	Lanabecestat (AZD3293)	Neuronal Signaling	412.53
549	PF-06447475	Autophagy	305.33
550	SB366791	Transmembrane Transporters	287.74

Appendix

551	Ponesimod	GPCR & G Protein	460.97
552	SKL2001	Stem Cells & Wnt	286.29
553	ITSA-1 (ITSA1)	Epigenetics	292.12
554	APS-2-79 HCl	MAPK	423.89
555	LXR-623 (WAY-252623)	Metabolism	422.78
556	Erdafitinib (JNJ-42756493)	Angiogenesis	446.54
557	Stenoparib (E7449)	DNA Damage/DNA Repair	317.34
558	NS-398 (NS398)	Neuronal Signaling	314.36
559	8-OH-DPAT (8-Hydroxy-DPAT)	Neuronal Signaling	247.38
560	ZINC00881524 (ROCK inhibitor)	Cell Cycle	380.46
561	VPS34 inhibitor 1 (Compound 19)	PI3K/Akt/mTOR	391.47
562	TAK-063	Metabolism	428.42
563	GSK2982772	Apoptosis	377.40
564	Pamiparib (BGB-290)	DNA Damage/DNA Repair	298.31
565	S 38093	Neuronal Signaling	288.38
566	NGP 555	Proteases	406.52
567	Vorasidenib (AG-881)	Metabolism	414.74
568	Chk2 Inhibitor II (BML-277)	Cell Cycle	363.80
569	AZD1390	PI3K/Akt/mTOR	477.57
570	AS1517499	JAK/STAT	397.86
571	A-804598	Neuronal Signaling	315.37
572	AZ32	DNA Damage/DNA Repair	328.37
573	Bimiralisib (PQR309)	PI3K/Akt/mTOR	411.38
574	ABX-1431	Metabolism	507.39
575	Albiflorin	Neuronal Signaling	480.46
576	Salvianolic acid A	Immunology & Inflammation	494.45
577	Songorine	Neuronal Signaling	357.49
578	Jatrorrhizine chloride	Neuronal Signaling	373.83
579	Tenuifolin	Neuronal Signaling	680.82
580	Beta-Asarone	Others	208.25
581	Benzoylpaeoniflorin	Immunology & Inflammation	584.57
582	Chelidonine	Neuronal Signaling	353.37
583	Xanthotoxol	Neuronal Signaling	202.16
584	Catharanthine hemitartrate	Neuronal Signaling	822.94
585	Oroxin B	Apoptosis	594.52
586	Huperzine B	Neuronal Signaling	256.34
587	α -Cyperone	Immunology & Inflammation	218.33
588	Isocorynoxine	Neuronal Signaling	382.45
589	Securinine	Neuronal Signaling	217.26
590	Corydaline	Neuronal Signaling	369.45
591	(+)-Isocorynoline	Neuronal Signaling	341.40
592	Nodakenin	Neuronal Signaling	408.40
593	Bz-RS-ISer(3-Ph)-Ome	Others	299.32

Appendix

594	N-Benzoyl-(2R,3S)-3-phenylisoserine	Others	285.29
595	Kavain	Neuronal Signaling	230.26
596	Mecamylamine Hydrochloride	Neuronal Signaling	203.75
597	Madecassic acid	Immunology & Inflammation	504.70
598	Protriptyline hydrochloride	Neuronal Signaling	299.84
599	Anisodamine Hydrobromide	Immunology & Inflammation	386.28
600	Ensartinib (X-396) dihydrochloride	Angiogenesis	634.36
601	S107	Others	209.31
602	PLX5622	Protein Tyrosine Kinase	395.41
603	Ruscogenin	Immunology & Inflammation	430.62
604	Picfeltaenine IA	Neuronal Signaling	762.92
605	Indoprofen	PI3K/Akt/mTOR	281.31
606	Lerisetron	Neuronal Signaling	292.38
607	Cytosporone B	Cell Cycle	322.40
608	Ebselen	Microbiology	274.18
609	L-779450	MAPK	347.80
610	IOX4	Angiogenesis	328.33
611	Olutasidenib (FT-2102)	Metabolism	354.79
612	Lvguidingian	Neuronal Signaling	272.17
613	P7C3-A20	Others	506.21
614	Pirenperone	Neuronal Signaling	393.45
615	Licofelone (ML3000)	Neuronal Signaling	379.88
616	1-Phenylbiguanide	Neuronal Signaling	177.21
617	FK-3311	Immunology & Inflammation	341.33
618	VU0238429	Neuronal Signaling	351.28
619	SB 200646	Neuronal Signaling	266.30
620	ML-297	Transmembrane Transporters	328.32
621	ATB 346	Immunology & Inflammation	365.45
622	Mavacoxib	Immunology & Inflammation	385.34
623	SC-560	Immunology & Inflammation	352.74
624	TFAP	Immunology & Inflammation	281.23
625	Anle138b	Neuronal Signaling	343.17
626	TG4-155	GPCR & G Protein	394.46
627	VU0357017 Hydrochloride	Neuronal Signaling	369.89
628	PQR620	PI3K/Akt/mTOR	445.47
629	SN-6	Transmembrane Transporters	402.46
630	YF-2	Epigenetics	430.85
631	DREADD agonist 21	Neuronal Signaling	278.35
632	Raphin1 acetate	Metabolism	291.13
633	Nodakenetin	Metabolism	246.26
634	Picfeltaenine IB	Neuronal Signaling	792.95
635	Pectolarigenin	Immunology & Inflammation	314.29
636	Myrislignan	Immunology & Inflammation	374.43

Appendix

637	Marmesin	Immunology & Inflammation	246.26
638	Caulophylline (N-Methylcytisine)	Neuronal Signaling	204.27
639	Bozitinib (PLB-1001)	Protein Tyrosine Kinase	424.38
640	NE 52-QQ57	GPCR & G Protein	416.52
641	Clozapine N-oxide	Neuronal Signaling	342.82
642	Capric acid	Neuronal Signaling	172.26
643	MDL-28170	Proteases	382.45
644	UNC2025	Protein Tyrosine Kinase	476.66
645	Pardopruxon (SLV-308) hydrochloride	Neuronal Signaling	269.73
646	PF-04995274	Neuronal Signaling	432.51
647	BNC210	Neuronal Signaling	317.38
648	FPL 62064	Metabolism	265.31
649	RHC 80267	Neuronal Signaling	394.51
650	VU0238441	Neuronal Signaling	339.70
651	VU0119498	Neuronal Signaling	316.15
652	PZ-2891	Metabolism	349.43
653	Irinotecan (CPT-11)	DNA Damage/DNA Repair	586.68
654	Myosmine	Neuronal Signaling	146.19
655	MCC950	Immunology & Inflammation	404.48
656	Prim-o-glucosylcimifugin	Immunology & Inflammation	468.45
657	Ginsenoside Rb3	NF-κB	1079.27
658	Polygalacic acid	Proteases	504.70
659	Palbociclib (PD-0332991) HCl	Cell Cycle	483.99
660	Pemetrexed (LY-231514) disodium	Metabolism	471.37
661	Galanthamine HBr	Neuronal Signaling	368.27
662	Granisetron HCl	Neuronal Signaling	348.87
663	Varenicline Tartrate (CP 526555-18)	Neuronal Signaling	361.35
664	Ibuprofen Lysine	Neuronal Signaling	352.47
665	Palbociclib (PD0332991) Isethionate	Cell Cycle	573.66
666	Cytarabine (U-19920A)	DNA Damage/DNA Repair	243.22
667	Penicillamine	Others	149.21
668	Tranexamic Acid	Others	157.21
669	Procarbazine HCl	DNA Damage/DNA Repair	257.76
670	D-Cycloserine	Microbiology	102.09
671	Gabapentin	Neuronal Signaling	171.24
672	Donepezil HCl	Neuronal Signaling	416.00
673	Neostigmine Bromide	Neuronal Signaling	303.20
674	Streptomycin sulfate	Microbiology	1457.38
675	Solifenacin succinate	Neuronal Signaling	480.55
676	Palonosetron HCl	Neuronal Signaling	332.87
677	Abacavir sulfate	Microbiology	335.35
678	Ceftazidime	Microbiology	546.58
679	Pirenzepine dihydrochloride	Neuronal Signaling	424.32

Appendix

680	Acamprosate Calcium	Transmembrane Transporters	200.24
681	Flavoxate HCl	Neuronal Signaling	427.92
682	Dexamethasone Sodium Phosphate	Immunology & Inflammation	516.40
683	Hexamethonium Dibromide	Neuronal Signaling	362.19
684	Succinylcholine Chloride Dihydrate	Neuronal Signaling	397.34
685	Tolmetin Sodium	Immunology & Inflammation	315.30
686	Pralidoxime chloride	Neuronal Signaling	172.61
687	4-Aminobutyric acid (GABA)	Neuronal Signaling	103.12
688	Choline bitartrate	Neuronal Signaling	253.25
689	Sodium ferulate	Neuronal Signaling	216.17
690	Choline Glycerophosphate	Others	257.22
691	Fosfomycin Disodium	Microbiology	182.02
692	Methotrexate disodium	Metabolism	498.40
693	Homotaurine	Neuronal Signaling	139.17
694	L-Alanine	Others	89.09
695	L-aspartic Acid	Others	133.10
696	Pemetrexed Disodium Hydrate	Metabolism	516.42
697	MCC950 Sodium (CP-456773 Sodium)	Immunology & Inflammation	426.46
698	Fosphenytoin (disodium)	Others	406.24
699	Erlotinib (OSI-774) HCl	Protein Tyrosine Kinase	429.90
700	Tandutinib (MLN518)	Angiogenesis	562.70
701	Vandetanib (ZD6474)	Protein Tyrosine Kinase	475.35
702	Cefoselis Sulfate	Microbiology	620.64
703	Ofloxacin	DNA Damage/DNA Repair	361.37
704	Risperidone	Neuronal Signaling	410.48
705	Methyldopa	Metabolism	211.21
706	Paliperidone	Neuronal Signaling	426.48
707	Irsogladine	Metabolism	256.09
708	Lornoxicam	Neuronal Signaling	371.82
709	Vinpocetine	Transmembrane Transporters	350.45
710	Ketanserin	Neuronal Signaling	395.43
711	(-)-Huperzine A (HupA)	Neuronal Signaling	242.32
712	Itraconazole (R 51211)	Stem Cells & Wnt	705.65
713	Trazodone HCl	Neuronal Signaling	408.32
714	NU7026	DNA Damage/DNA Repair	281.31
715	Droxidopa	GPCR & G Protein	213.19
716	Nuciferine	Neuronal Signaling	295.38
717	Amoxapine	Neuronal Signaling	313.78
718	Alectinib (CH5424802) hydrochloride	Protein Tyrosine Kinase	519.08
719	Lazertinib	Protein Tyrosine Kinase	554.64
720	Stylopine	Immunology & Inflammation	323.34
721	Azasetron HCl	Neuronal Signaling	386.27
722	Alosetron Hydrochloride	Neuronal Signaling	330.81

Appendix

Table 5. List of 722 CNS-penetrant compound library. Drugs numbered 1 to 658 were dissolved in DMSO at a concentration of 10 mM. Drugs numbered 659 to 698 were dissolved in water at a concentration of 10 mM. Drugs numbered 699 to 720 were dissolved in DMSO at a concentration of 2 mM, while drugs 721 and 722 were dissolved in water at a concentration of 2 mM. The targeted pathway for each drug and its molecular weight are also listed.

Curriculum Vitae

PERSONAL INFORMATION

Name: Maryam Salarian

Born: 16th April 1992

Nationality: Iranian

Contact: Maryam.salarian@kit.edu

EDUCATION

Karlsruher Institut für Technologie (KIT)	Karlsruhe, Germany
Ph.D. candidate at the institute of biological and chemical systems	June 2021-Feb 2025

University of Tehran	Tehran, Iran
Master's degree: Biochemistry	Sep 2015-Feb 2018
Thesis: Effect of vinorelbine on the content and expression of HMG proteins in lung cancer cells	

Alzahra University	Tehran, Iran
Bachelor's degree: Biotechnology	Sep 2010- Feb 2014

EXPERIENCE

Institute of Biological and Chemical Systems, KIT University	Karlsruhe, Germany
Doctoral researcher	June 2021-Feb 2025

Institute of Endocrinology & Metabolism, University of Tehran	Tehran, Iran
Assisting researcher	Jan 2021–April 2021

Breast Cancer Institute, University of Tehran	Tehran, Iran
Assisting researcher	March 2018–Dec 2020

PUBLICATION

Nanoliter Hydrogel Array for Cell Screening and Cell Spheroid Sorting, Salarian M., Levkin P., Popova A., Advanced Materials Technology, Dec 2024.

Acknowledgement

First, I want to thank Prof. Pavel Levkin and Dr. Anna Popova for giving me the chance to do this work under their supervision. Thank you for your constant feedback, support, and belief in me.

I am also very grateful to Dr. Marc Schneider, Dr. Michael Meister, and Prof. Dr. Thomas Muley from the Thoraxklinik, University Hospital of Heidelberg, for their great collaboration over the last three years. Thank you for all the helpful feedback and discussions about my project. A special thanks goes to Prof. Dr. Sevin Turcan from the Neurology Clinic and National Center for Tumor Diseases, University Hospital of Heidelberg, for providing the consumables for the project and for the valuable feedback and discussions.

I would like to thank Joaquín Eduardo Urrutia Gómez and Prof. Markus Reischl from the Institute for Automation and Applied Informatics for their discussions and advice on using GridScreener to evaluate my data.

Thank you to everyone in the Levkin Lab for creating such a great working atmosphere over the years. Your brainstorming sessions, feedback, and support meant so much to me, especially when I broke my finger and couldn't work properly. I couldn't have done this without you.

To my parents, thank you for encouraging me to follow a career in science and for supporting my move to Germany. A special thanks to my brother, Arash, who was like a mentor to me throughout my PhD. I learned so much from him, and I am lucky to have had his guidance.

I also want to thank my best friend, Homa Esfahani, for always supporting me and helping me in my academic journey.

Finally, I want to give a big thank you to Emad Hadji for always believing in me, standing by my side, and supporting me in so many ways. Thank you for driving me to campus so many times on weekends and holidays and waiting for hours while I finished my experiments. This journey wouldn't have been possible without you.